

Simulation of the (α, n) - induced Background in the
CDMS-II Dark Matter Search Experiment

von
Michał Tarka

Diplomarbeit in Physik
vorgelegt der

Fakultät für Mathematik, Informatik und Naturwissenschaften
der RWTH Aachen

im Oktober 2007

angefertigt im

I. Physikalischen Institut der RWTH Aachen
Prof. Dr. Laura Baudis

Michał Tarka

16. Oktober 2007

Contents

1	Introduction	1
1.1	Cosmology	3
1.2	Hints for Dark Matter in the Universe	6
1.3	Dark Matter Candidates	18
1.3.1	Baryonic Dark Matter	18
1.3.2	Non-Baryonic Candidates	19
1.4	Direct detection of Dark Matter	21
2	CDMS I, II, SuperCDMS	26
2.1	CDMS I at SUF	26
2.2	CDMS II at Soudan	27
2.3	Super CDMS at SNOLAB	28
2.4	Inner Life of CDMS II	29
2.4.1	The Zip Detectors	29
2.4.2	Cryogenics	33
2.4.3	Shielding and Muon Veto	34
2.5	Neutron backgrounds at CDMS II	35
2.6	Neutrons interactions with matter	36
2.7	Neutrons from (α, n) reactions	36
2.8	Neutrons from spontaneous fission	38
3	The neutron calibration run with ^{252}Cf	40
3.1	GEANT4	40
3.2	Monoenergetic neutron simulation on Si and Ge	42
3.3	Calculating the neutron cross sections	43
3.4	Testing the LHEP-BIC-HP physics	44
3.5	Testing the LBE physics	47
3.6	Neutron Calibrations with Cf^{252}	50
3.7	^{252}Cf Spectrum	52
3.8	GEANT4 Simulation of a ^{252}Cf source	54
3.8.1	Comparison-Monte Carlo/Data	55

4 Simulation of the (α, n)-induced neutron backgrounds	61
4.1 SOURCES4mv	61
4.2 (α, n) -reactions in the CDMS assembly	61
4.3 (α, n) -reactions in the Greenstone rock	65
4.4 (α, n) -reactions in Air	67
4.5 Spontaneous fission	74
4.6 The simulation runs	77
4.7 The (α, n) -runs	77
4.8 Spontaneous fission - the inner poly run	81
5 Results and discussion	82
A ^{252}Cf-neutron calibration spectras	87
B (α, n)-neutron spectras.	101
C Spontaneous Fission-neutron spectras.	109
D Acknowledgment	120

List of Figures

1.1	Hertzsprung-Russel diagram.	7
1.2	Spiral galaxy NGC 3198.	9
1.3	Rotation curve of NGC 3198.	9
1.4	The Virgo Cluster.	11
1.5	NGC 2300.	12
1.6	Large scale structure of the Universe.	13
1.7	Large scale simulation models.	14
1.8	Einstein Cross G2237+0305	15
1.9	The Abell 2218 Cluster.	16
1.10	Microlensing effect.	17
1.11	Bullet cluster.	18
1.12	Principle of a WIMP detector.	22
1.13	DAMA modulation.	24
1.14	Formfactors of Si, Ge and Xe.	25
2.1	CDMS shielding at SUF.	27
2.2	Limits on cross sections.	28
2.3	ZIP detector.	29
2.4	Scheme of a ZIP detector.	31
2.5	Yield bands.	32
2.6	Scheme of the CDMS cryostat.	33
2.7	Scheme of the CDMS shielding.	34
3.1	CDMS assembly in GEANT 4.	41
3.2	GEANT4 neutron cross sections.	42
3.3	Neutron cross sections (0-20 MeV) in Ge , physics library LHEP-BIC-HP.	45
3.4	Neutron cross sections (0-20 MeV) in Si , physics library LHEP-BIC-HP.	45
3.5	Neutron cross sections (0-10 MeV) in Ge , physics library LHEP-BIC-HP.	46
3.6	Neutron cross sections (0-10 MeV) in Si , physics library LHEP-BIC-HP.	46

3.7	Neutron cross sections (0-20 MeV) in Ge , physics library LBE	48
3.8	Neutron cross sections (0-20 MeV) in Si , physics library LBE	48
3.9	Neutron cross sections (0-10 MeV) in Ge , physics library LBE	49
3.10	Neutron cross sections (0-10 MeV) in Si , physics library LBE	49
3.11	^{252}Cf calibration yield-plot.	51
3.12	^{252}Cf neutron spectrum.	54
3.13	Yield plot of a simulated ^{252}Cf neutron source.	56
3.14	^{252}Cf , MonteCarlo vs. Data spectrum.	58
4.1	Neutron spectras from (α, n) reactions.	64
4.2	(α, n) reactions in the Green Stone rock.	67
4.3	Simulated α ranges, α -energy: 4.7 MeV	71
4.4	Simulated α ranges, α -energy: 4 MeV.	72
4.5	Green Stone volume containing possibly escaping α particles.	73
4.6	Considering (α, n) reactions in Air in SOURCES4mv.	73
4.7	(α, n) reactions in air.	74
4.8	Spontaneous fission in copper.	75
4.9	Spontaneous fission in polyethylene and the Green Stone rock.	76
4.10	Neutron ranges in the Green Stone rock.	79
4.11	Cavern geometry in GEANT4.	80
5.1	Single events spectrum.	85
A.1	^{252}Cf -MC/Data - nuclear recoil spectras in detektors 402 and 404	89
A.2	^{252}Cf -MC/Data - nuclear recoil spectras in detektors 405 and 411	90
A.3	^{252}Cf -MC/Data - nuclear recoil spectras in detektors 412 and 413	91
A.4	^{252}Cf -MC/Data - nuclear recoil spectras in detektors 414 and 415	92
A.5	^{252}Cf -MC/Data - nuclear recoil spectras in detektors 423 and 422	93
A.6	^{252}Cf -MC/Data - nuclear recoil spectras in detektors 424 and 425	94
A.7	^{252}Cf -MC/Data - nuclear recoil spectras in detektors 426 and 431	95
A.8	^{252}Cf -MC/Data - nuclear recoil spectras in detektors 432 and 433	96
A.9	^{252}Cf -MC/Data - nuclear recoil spectras in detektors 434 and 435	97
A.10	^{252}Cf -MC/Data - nuclear recoil spectras in detektors 436 and 441	98
A.11	^{252}Cf -MC/Data - nuclear recoil spectras in detektors 443 and 444	99
A.12	^{252}Cf -MC/Data - nuclear recoil spectras in detektors 445 and 446	100
B.1	U- (α, n) -spectra in the Cu-cans.	101
B.2	Th- (α, n) -spectra in the Cu-cans.	102
B.3	U+Th- (α, n) -spectra in the Cu-cans.	102
B.4	U- (α, n) -spectra in the Cu-towerguts.	103
B.5	Th- (α, n) -spectra in the Cu-towerguts.	103
B.6	U+Th- (α, n) -spectra in the Cu-towerguts.	104
B.7	U- (α, n) -spectra in the inner poyethylene shield.	104
B.8	Th- (α, n) -spectra in the inner poyethylene shield.	105
B.9	U+Th- (α, n) -spectra in the inner poyethylene shield.	105

B.10 U-(α, n)-spectra in the Green Stone rock.	106
B.11 Th-(α, n)-spectra in the Green Stone rock.	106
B.12 U+Th-(α, n)-spectra in the Green Stone rock.	107
C.1 U-(SF)-spectra in the Cu-cans.	109
C.2 Th-(SF)-spectra in the Cu-cans.	110
C.3 U+Th-(SF)-spectra in the Cu-cans.	110
C.4 U-(SF)-spectra in the Cu-towerguts.	111
C.5 Th-(SF)-spectra in the Cu-towerguts.	111
C.6 U+Th-(SF)-spectra in the Cu-towerguts.	112
C.7 U-(SF)-spectra in the inner polyethylene shield.	112
C.8 Th-(SF)-spectra in the inner polyethylene shield.	113
C.9 U+Th-(SF)-spectra in the inner polyethylene shield.	113
C.10 U-(SF)-spectra in the Green Stone rock.	114
C.11 Th-(SF)-spectra in the Green Stone rock.	114
C.12 U+Th-(SF)-spectra in the Green Stone rock.	115

List of Tables

1.1	Cosmological models	15
3.1	Natural abundancies of Ge and Si	44
3.2	χ^2 -tests on cross sections in Ge and Si	47
3.3	Cf^{252} neutron emission probabilities	53
3.4	Monte Carlo scale factors for nuclear recoils	59
3.5	Monte Carlo scale factors for single events	60
4.1	U and Th concentrations at CDMS	62
4.2	CDMS components as (α, n) -neutron sources	62
4.3	Atom-densities of U and Th in the CDMS components	63
4.4	Natural abundance of Cu and C	63
4.5	Chemical composition of the Green Stone rock	66
4.6	Abundance of the elements in the Green Stone rock	66
4.7	Ranges of U-emitted α -particles in the Green Stone rock	69
4.8	Ranges of Th-emitted α -particles in the Green Stone rock	69
4.9	MC, (α, n) neutrons in the icebox.	77
4.10	MC, (α, n) neutrons in the towerguts	78
4.11	MC, (α, n) neutrons in the inner polyethylene shield	78
4.12	MC, (α, n) neutrons in the rock	80
4.13	MC, spontaneous fission neutrons in the inner polyethylene shield	81
5.1	U and Th concentrations at Soudan	82
5.2	Atomdensities of U and Th at Soudan	82
5.3	(α, n) -neutron fluxes at Soudan	83
5.4	(SF) -neutron rates at Soudan	83
5.5	Expected neutron rates at Soudan	84
A.1	Alternative detector names	88
B.1	Natural isotopic abundance in the Green Stone rock	108

Chapter 1

Introduction

An overwhelming amount of information we have about our Universe is obtained by analyzing and interpreting electromagnetic radiation reaching the earth. All matter at finite temperatures and all processes with participation of electromagnetic interaction are sources for new electromagnetic waves. We can investigate the light emitted by a radiation-source in order to get some information about the physical state of its matter, or take a look at the modification of this light caused by another cosmic object like intergalactic dust or by gravitation. In order to explain the structure of our Universe including the formation of matter and its composition, astrophysicists and particle-physicists started in the last century to complement each other, establishing a very prospering cooperation. Due to the fact that astrophysicists must rely on their correct interpretation of the light-signals from outer space reaching their measuring instruments, it is essential to understand the processes which created this signals on a microscopic scale, and hence there is no way to explain the mysteries of the Universe without the support of theoretical and experimental results in particle physics on earth. On the other hand, astrophysical observations can set constraints on many theoretical concepts in particle physics, and provide observations of particle states at energy scales, which cannot be reached at earth-conditions.

Although a lot of progress has been made in both fields, many open questions still remain, such as those of the formation of galaxies, the origin of super-massive black holes in galaxy centers, the formation of large scale structures, the origin of space-time, energy, the number of dimensions in the world and also the puzzle of matter content in our Universe.

Exciting astrophysical observations performed by satellite-missions like HUBBLE, ROSAT or COBE provided us with new knowledge about Large Scale Structure, Cosmic Microwave Background radiation (CMB) and gravitational lensing which besides other local phenomena like Ia supernovae, not only strongly indicate the existence of the so-called **Dark Matter** and/or **Dark Energy** emerging as a constant in the field equations of Einstein's general relativity, but also its overwhelming domination over the baryonic matter, described by the standard model

in particle physics. In this equations Dark Energy can be interpreted as the effective gravitation of vacuum energy. The first hints for dark matter whose identity still remains unclear were provided in the early 20'th century by astronomers like Zwicky and Oort and the search for it is of fundamental importance for modern physics and beyond any doubt, one of the biggest scientific challenges nowadays. Observations suggest, that our Universe contains $\sim 73\%$ dark energy, $\sim 23\%$ non-baryonic dark matter and only $\sim 4\%$ of ordinary, baryonic matter.

The astrophysical search for Dark Matter goes hand in hand with examining the theoretical area for adequate dark-matter particle candidates, whose number can be effectively narrowed by observations. The existence of this matter could be an indication for supersymmetry. The CDMS (Cryogenic Dark Matter) experiment in Soudan, Minnesota is an underground-facility experiment based on Ge and Si detectors, which is searching for elastic atomic nuclei scattering single-events potentially caused by **Weakly Interacting Massive Particles** (WIMPs). WIMPs are particles predicted for example by supersymmetric models and represent one of the possible Dark Matter candidates, which could have been produced shortly after the Big Bang. In spite of their low interaction probability with baryonic matter, they should be detectable under low-background conditions, suppositional they are the 'Dark Matter' or part of it at least.

1.1 Cosmology

Gravitation, described by general relativity, is the dominant force in the Universe and although a lot of effort was done to unify gravitation with the electroweak and strong interaction, general relativity stays the ruling formalism describing large scale phenomena in the Universe. The structure of space-time as well as the energy and matter content of the Universe is described by the Einstein's **field equations**:

$$\mathfrak{R}_{\mu\nu} - \frac{1}{2}\mathfrak{R}g_{\mu\nu} - \Lambda g_{\mu\nu} = -\frac{8\pi G}{c^4} \cdot T_{\mu\nu} \quad (1.1)$$

where $\mathfrak{R}_{\mu\nu}$ is the **Ricci Tensor** describing the space curvature at any order of dimension and \mathfrak{R} is a curvature scalar. Both quantities are functions of the **metric tensor** $g_{\mu\nu}$ which relates distance and time via

$$ds^2 = -g_{\mu\nu}dx^\mu dx^\nu. \quad (1.2)$$

G , c and Λ are constants and $T_{\mu\nu}$ is the **energy-momentum tensor** describing the density and flux of energy and momentum in spacetime.

Investigations on the large scale distribution of galaxies and galaxy-clusters demonstrate the isotropic and homogeneous structure of the universe at constant time intervals since the Big Bang [1].

The expansion of such an Universe, whose geometry depends on its matter and energy content is described by a metric tensor of **Robertson-Walker** form:

$$ds^2 = c^2dt^2 - R^2(t)[\frac{dr^2}{(1-kr^2)} + r^2(d\theta^2 + \sin^2\theta d\phi^2)] \quad (1.3)$$

In this equation k stands for the curvature constant, $k = 0$ or ± 1 whereas the **cosmological scale factor** $R=R(t)$ describes the increase of distance between objects caused by the expansion of space-time.

In contrast to the variable time the **redshift** z is a very useful and measurable quantity, which can be used instead. The redshift is a shift in frequency of emitted light caused by the expansion of the Universe, hence the older the light the bigger its shift in wavelength towards longer wavelengths.

$$z \equiv \frac{\Delta\lambda}{\lambda} = \frac{R_0 - R(t)}{R(t)} = \tilde{R}^{-1} - 1 \quad (1.4)$$

where λ is the wavelength, $\Delta\lambda$ its shift, R_0 the present value of the cosmological factor and $\tilde{R} \equiv \frac{R(t)}{R_0}$ the relative scale factor. In this context, we can introduce a new very important parameter - the **Hubble parameter** H , by differentiating equation (1.4)

$$dz = -\frac{R_0dR}{R^2} = -\frac{R_0\dot{R}dt}{R^2} \Rightarrow dt = -\frac{R^2dz}{R_0\dot{R}} = -\frac{dz}{(1+z)H(z)} \quad (1.5)$$

with

$$H \equiv \frac{\dot{R}}{R} \quad (1.6)$$

The Hubble parameter is a time depending quantity which describes the expansion rate of the Universe. The value of this parameter at the present time is known as the **Hubble's constant** H_0 . This pseudo-constant is a measurand provided with an uncertainty which is expressed by h_0 , a dimensionless correction parameter, whose value is thought to be approximately $h_0 = 0.73^{+0.03}_{-0.04}$ [2].

$$H_0 = 100h_0 \text{km s}^{-1} \text{Mpc}^{-1} \quad (1.7)$$

The parameter H is determined by the amount of energy and matter contained in the Universe. The behaviour of both, matter and energy can be described similarly to the behaviour of a perfect fluid by an energy-momentum tensor:

$$T_{\mu\nu} = (\rho + \frac{p}{c^2})U_\mu U_\nu + pg_{\mu\nu} \quad (1.8)$$

where ρ plays the role of a density of the 'cosmic' fluid, p is its pressure and $U_{\mu,\nu}$ its four-velocity.

Additionally p and ρ are related by the following equation of state

$$p = (\gamma - 1) \cdot \rho c^2 \quad (1.9)$$

where γ is a constant whose value depends on the type of fluid.

Matter, radiation and the cosmological constant Λ appear to be the sources of gravitation in Einstein's field equations.

Regarding matter as pressure-less dust and assuming a 'no collision and no relativistic velocities' scenario, its pressure p_m can be set to zero.

The radiation pressure p_r in the early Universe is found by relativistic considerations to be $\frac{1}{3}\rho_r c^2$ [3]. In future vacuum energy could dominate the Universe (see Equation (1.15)), and one can assume a vacuum energy pressure of $p_v = -\rho_v c^2$.

- **dustlike matter:** $p_m = 0, (\gamma_m = 1)$
- **radiation :** $p_r = \frac{1}{3}\rho_r c^2, (\gamma_r = \frac{4}{3})$
- **vacuum energy :** $p_v = -\rho_v c^2, (\gamma_v = 0)$

For a homogeneous and isotropic Universe we can use the Robertson-Walker metric (1.3) and the energy-momentum tensor for a perfect fluid (1.8) to solve the field equations (1.1):

$$H^2 + \frac{kc^2}{R^2} - \frac{\Lambda c^2}{3} = \frac{8\pi G\rho}{3} \quad (1.10)$$

Defining a **vacuum energy density** :

$$\rho_\Lambda c^2 \equiv \frac{\Lambda c^4}{8\pi G} = constant \quad (1.11)$$

and the **critical density**:

$$\rho_{crit}(t) \equiv \frac{3H^2(t)}{8\pi G} = 1.88 \cdot 10^{-29} h_0^2 g cm^{-3} \quad (1.12)$$

equation (1.10) can be written as

$$\frac{kc^2}{R_0^2} = H_0^2 \left(\frac{\rho_{r,0} + \rho_{m,0} + \rho_\Lambda - \rho_{crit,0}}{\rho_{crit,0}} \right) \quad (1.13)$$

for a Universe at present time.

This equation shows clearly, that if the sum of

- $\rho_{r,0} + \rho_{m,0} + \rho_\Lambda = \rho_{crit,0} \Rightarrow k = 0$,

than the Universe is flat and infinite in extent, if

- $\rho_{r,0} + \rho_{m,0} + \rho_\Lambda > \rho_{crit,0} \Rightarrow k > 0$,

than the Universe is unbounded but closed, it has a finite and positively curved, spherical geometry. In the last case

- $\rho_{r,0} + \rho_{m,0} + \rho_\Lambda < \rho_{crit,0} \Rightarrow k < 0$,

the Universe is unbounded, infinite and of hyperbolic geometry.

That is, why $\rho_{crit,0}$ is such an important quantity - it determines the geometry of our Universe. Substituting $\rho_{r,0}, \rho_{m,0}, \rho_\Lambda, 0$ by three dimensionless **density parameters**:

- $\Omega_{r,0} \equiv \frac{\rho_{r,0}}{\rho_{crit,0}}$,
- $\Omega_{m,0} \equiv \frac{\rho_{m,0}}{\rho_{crit,0}}$,
- $\Omega_{\Lambda,0} \equiv \frac{\rho_\Lambda}{\rho_{crit,0}} = \frac{\Lambda c^2}{3H_0^2}$

and by defining an $\Omega_{tot,0} \equiv \Omega_{r,0} + \Omega_{m,0} + \Omega_{\Lambda,0}$,
equation (1.13) can be written as

$$k = \left(\frac{R_0 H_0}{c^2} \right) (\Omega_{tot,0} - 1) \quad (1.14)$$

This equation allows us to make conclusions on the geometry of our Universe by determining the total matter and energy densities, normalized by ρ_{crit} .

Substituting equation (1.14) back to equation (1.10), using the density parameters $\Omega_{r,0}, \Omega_{m,0}, \Omega_{\Lambda,0}$ and $z = \frac{R_0 - R(t)}{R(t)}$ from equation (1.4) leads us to the **Friedmann-Lemaitre equation**

$$\tilde{H} = [\Omega_{r,0}(1+z)^4 + \Omega_{m,0}(1+z)^3 + \Omega_{\Lambda,0} - (\Omega_{tot,0} - 1)(1+z)^2]^{1/2} \quad (1.15)$$

which describes the relative expansion rate $\tilde{H} \equiv \frac{H(z)}{H_0}$.

This equation already tells us a lot about the evolution processes of the Universe. The first and the second term $\Omega_{r,0}(1+z)^4$ and $\Omega_{m,0}(1+z)^3$ show that both, radiation and matter act as a source of gravity to increase the expansion rate with increasing z-values.

The third term $\Omega_{\Lambda,0}$ has no dependence on z and hence no dependence on time, which means a domination of the vacuum energy in the limit $t \rightarrow \infty$ in any Universe with $\Lambda > 0$.

Regarding $\Omega_{\Lambda,0} = (\frac{H_{t \rightarrow \infty}}{H_0^2})$ with the density parameter $\Omega_{\Lambda,0} \equiv \frac{\Lambda c^2}{3H_0^2}$ for the far future, leads to the equation

$$\Lambda c^2 = 3H_\infty^2$$

which describes a relation between vacuum energy and the expansion rate $H_{t \rightarrow \infty}$ at late times.

Finally the last term in equation (1.15) changes the weight of influence of the first 3 terms on the expansion rate by adding or subtracting a factor, depending on whether Ω_{tot} is smaller or bigger than one.

1.2 Hints for Dark Matter in the Universe

In 1911 E. Hertzsprung, a Danish astronomer discovered a correlation between the luminosity of stars and their type of spectrum and hence their temperature, which first allowed impartial classification of stars. The same discovery was made 1913 by H.N.Russel, an American astronomer. The graphical plot of the correlation between both characteristics is known as the **Hertzsprung-Russel-Diagram**.

Every point in this diagram is corresponding to a star at a given temperature and luminosity. Obviously the positions of the stars in this diagram are not arbitrary distributed. Most of them are placed along a well-defined band - the **Main Sequence**. There are also other 'agglomerations' of stars appearing above and below the main sequence. These regions correspond to different evolution stages of the stars.

Since stars can be regarded as black-body radiators, it is possible to estimate the mass of a given star using the HR-diagram. The radiation power P of a black body is described by the **Stefan Boltzmann - Law**

$$P = \sigma \cdot A \cdot T^4 \quad (1.16)$$

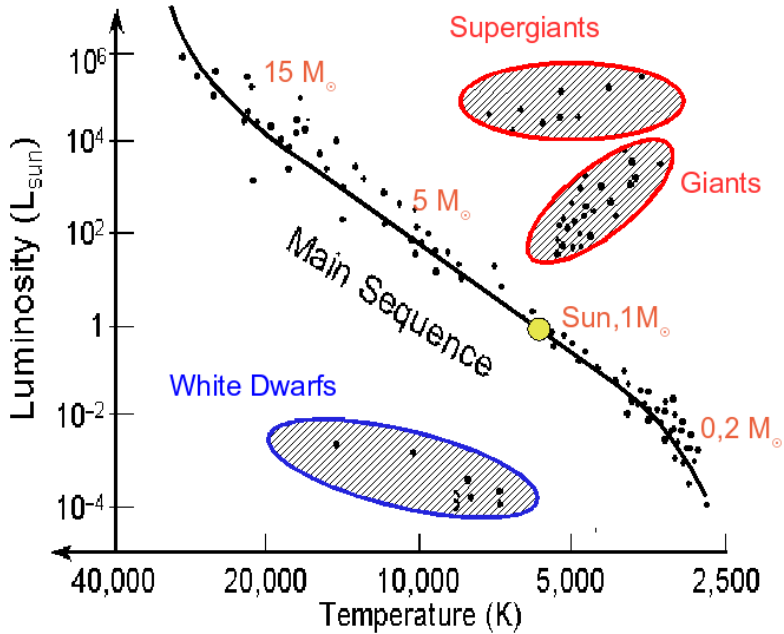


Figure 1.1: Hertzsprung-Russel diagram.

Most of the stars ($\sim 90\%$) are placed around the black curve which is called the "Main Sequence". The White Dwarf region contains hot stars which are small and hence not very luminous. Red Giants are stars at the final stage of their evolution. Such stars appear much more luminous, if they have much bigger masses than the sun and are classified as Super Giants.

where A is the surface of this body, T its temperature and
 $\sigma \approx 5.67 \cdot 10^{-8} \frac{W}{m^2 K^4}$
the Stefan-Boltzmann constant. This law allows us to define an effective temperature T_{eff} of a star in correlation to its luminosity L and radius R .

$$T_{eff} = \left(\frac{L}{4\pi R^2 \sigma} \right)^{1/4} \quad (1.17)$$

Considering the

- conservation of mass
- conservation of energy
- hydrostatic equilibrium
- energy transport

in a star, a theoretical relation between the mass M and its luminosity L can be derived, called the **mass-luminosity relation**

$$L \propto M^4 \quad (1.18)$$

Rotation curves of galaxies

The simple relationship between mass and the luminosity of a star in Equation (1.2) allows to make a rough estimate on masses of stars and galaxies. The mass of a galaxy can be also estimated by its dynamical behaviour. The rotation velocity of spiral galaxies for example is determined by its gravitational potential, hence measuring the velocity-distribution of a spiral galaxy by Doppler-effect, one can obtain information about its mass content. This measurements can be done analyzing the absorption lines of stars in the central region and by analyzing the emission lines of H I regions in the outer regions of a galaxy. Surprisingly, the rotation curves are flat at large distances from the center, which is not conform with, what can be expected by estimating the galaxies mass-distribution by its luminosity. Assuming, that the vast majority of its mass reside in the center of the galaxy, one can expect a velocity-distribution which is $\propto \sqrt{\frac{1}{r}}$, where r is the distance to the galaxy center. This follows from simple Newtonian-mechanics considerations.

$$G \frac{mM_r}{r^2} = \frac{mv^2}{r} \Rightarrow v(r) = \sqrt{\frac{GM_r}{r}} \quad (1.19)$$

In this equation M_r describes the mass contained in the galaxy-volume limited by the distance r from the galaxy-center, m is the mass of the regarded star, v its rotation velocity around the galaxy-center and G the gravitation-constant.

In the center of the galaxy the density ρ of its mass M can be considered as roughly constant $M = \rho \cdot V \propto r^3$ which with equation (1.19) results in

$$v(r) \propto r \quad (1.20)$$

This is consistent with the observations, in contrast to the velocity distribution in the outer galaxy-regions, where M_r can be considered as almost the whole mass of the galaxy. In this case equation (1.19) gives us a velocity-radius dependence of

$$v(r) \propto \sqrt{\frac{1}{r}} \neq \text{constant} \quad (1.21)$$

The discrepancy in the outer galaxy-regions between measurements and theory shown in Figure 1.3 can be solved by assuming a halo of dark matter, whose density ρ_{halo} shows the following dependence on r :

$$\rho_{halo}(r) \propto \frac{1}{r^2} \quad (1.22)$$

The concept of a Dark Matter halo in galaxies finds more support in other astrophysical investigations on the dynamics of e.g. elliptical galaxies and galaxy clusters.



Figure 1.2: Spiral galaxy NGC 3198.

This galaxy is an example of a barred spiral galaxy (Type SBc) at a distance of about 9.4 Mpc. The blue outer regions indicate the presence of young stars. H I gas in these regions can be used to determine the rotation distribution by measuring the doppler-shift of the 21cm emission line.

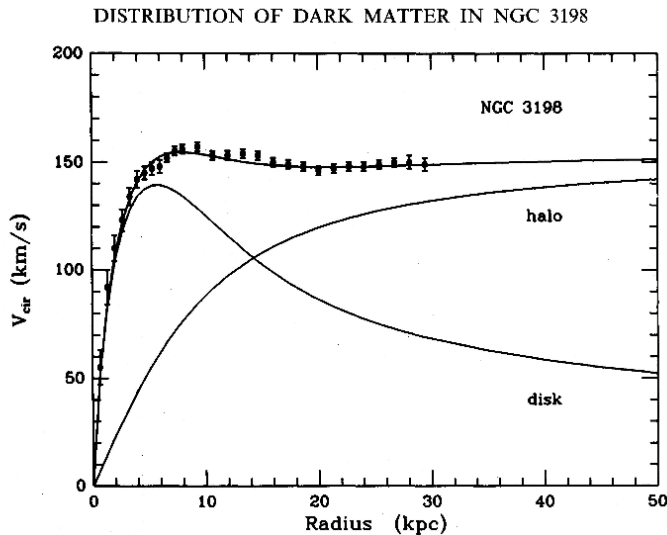


Figure 1.3: Rotation curve of NGC 3198.

The points show the galaxy's H I rotation curve [4], the disk-curve shows the expected rotation curve, if the mass-density distribution would follow the brightness distribution of the galaxy. The halo curve shows the rotation curve of the dark halo model, which is needed in order to explain the observed rotation curve.

Galaxy Clusters

Dynamical hints for Dark Matter can also be found on the next higher scale. Galaxy clusters are agglomerations of galaxies which find themselves within their collective gravitational sphere of influence. Analyzing their relative velocities, allows to determine the total mass of the cluster. Assuming that all cluster-galaxies are in a stationary state of equilibrium one can make use of the **Virial theorem** in order to make conclusions about the contribution of kinetic and potential energy to the total energy in an average over time.

$$2 \langle T \rangle = \langle \sum_i r_i \nabla_i V \rangle \quad (1.23)$$

Here i is the number of galaxies in the cluster, r_i the distances between them and T, V the kinetic and potential energy.

The average on time $\langle f \rangle$ on any function f is defined as

$$\langle f \rangle = \lim_{\tau \rightarrow \infty} \frac{1}{\tau} \int_0^\tau f(t) dt \quad (1.24)$$

Assuming a potential V of the form

$$V_j = \alpha_j \cdot r_j^m \quad (1.25)$$

equation (1.23) can be written as

$$2 \langle T \rangle = m \langle V \rangle \quad (1.26)$$

If the cluster contains n galaxies, then it has $\frac{n(n-1)}{2}$ gravitational interacting pairs.

$$\Rightarrow 2 \frac{1}{2} n \langle m \rangle \langle v^2 \rangle - G \frac{n(n-1)}{2} \frac{\langle m^2 \rangle}{r} = 0, \quad (1.27)$$

assuming $n(n-1) \rightarrow n^2$ and $\langle m^2 \rangle = \langle m \rangle^2$

$$\Rightarrow M \langle v^2 \rangle \approx G \frac{M^2}{2r} \Rightarrow M \approx \frac{2r \langle v^2 \rangle}{G} \quad (1.28)$$

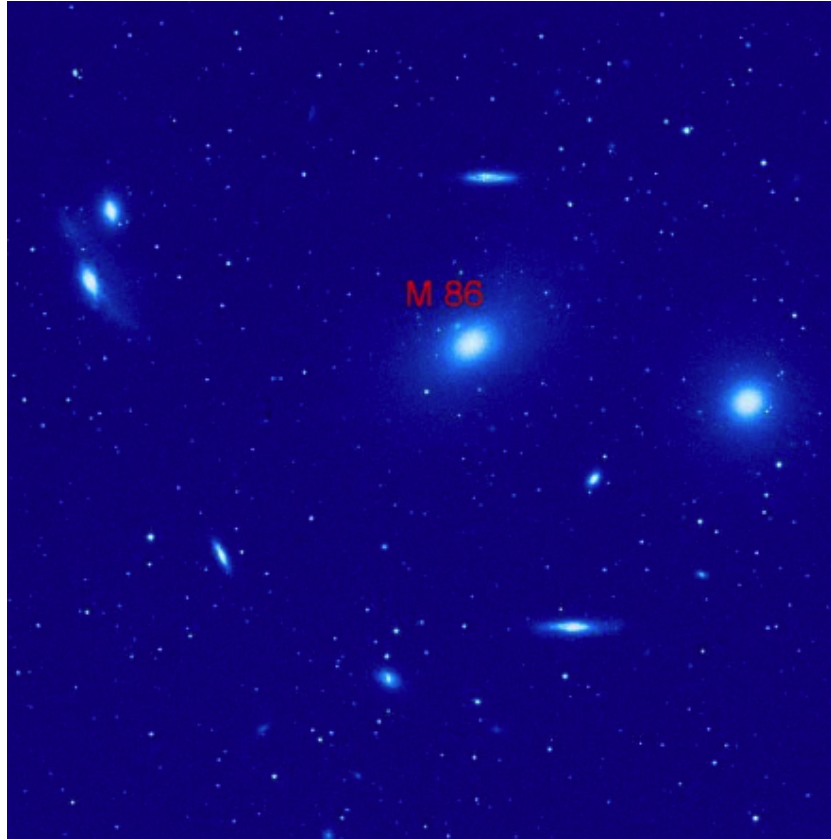


Figure 1.4: The Virgo Cluster.

This cluster in the constellation Virgo contains up to 2000 galaxies. Its virial mass is estimated to be around $7 \cdot 10^{14} M_{\odot}$ [5] with a baryonic matter fraction of about 18% [6].

Observations and measurements of the galaxy-velocities and their distances in a cluster result in much higher cluster masses, than one obtains considering only the sum of the visible galaxies.

This result is additionally supported by **X-ray observations**.

In Figure 1.5 we see the X-Ray emission of the very small NGC-2300 group made by ROSAT. This group is particularly interesting, because it has only a few members, which makes its visible mass designation easy. The galaxies are embedded in very hot gas originating from supernovae with a temperature of about $10^7 K$. This gas would pass of in the space if the gravitational potential of this group would be composed only from the visible matter. The total mass of NGC-2300 is estimated to be around 25 times bigger than the mass of the visible galaxy matter [7].



Figure 1.5: NGC 2300.

ROSAT X-ray picture of the NGC 2300 group showing galaxies embedded in hot gas of about $10^7 K$. The clusters mass is estimated to be around $3 \cdot 10^{13} M_\odot$ with a fraction of $\sim 4\%$ baryonic matter [7].

CMB

The cosmic microwave background radiation (CMB) offers the next hint for the existence of dark matter. The large scale structure of our Universe is an isotropic and homogeneous sponge-like-structure of galaxies with density fluctuations which become less granular with increasing z-values. In Figure 1.6 we see a survey of the z-depending galaxy distribution in the Universe made by the Anglo Australian Observatory.

The evolution of the density fluctuations of matter can be described by the relative density fluctuation defined as

$$\delta(\vec{r}, t) = \frac{\rho(\vec{r}, t) - \bar{\rho}(t)}{\bar{\rho}(t)} = D(t) \cdot \delta(\vec{r}, t) \quad (1.29)$$

where $\rho(\vec{r}, t)$ is the cosmic matter density at time t and position \vec{r} , $\bar{\rho}(t)$ is the mean cosmic matter density and $D(t)$ is an accretion coefficient.

CMB is an isotropic relict radiation of the primordial phase of our Universe, emerging from a time when photons decoupled from matter. Therefore the density fluctuations of matter at that time $\delta_{\rho_{mat}, 0}$ should cause fluctuations of the CMB corre-

sponding to $\rho_{mat,0}$. In fact, the spectrum of CMB is well described by a blackbody function with a current temperature of $T = 2.726K$, featuring small fluctuations in temperature δT which can be described by spherical harmonic functions $Y_{lm}(\Theta, \phi)$

$$\frac{\delta T}{T}(\Theta, \phi) = \sum_{l=2}^{\infty} \sum_{m=-l}^{+l} a_{lm} Y_{lm}(\Theta, \phi) \quad (1.30)$$

with the complex-valued weights a_{lm} .

The fluctuation δ_{CMB} was determined by the COBE, and later with a much better resolution by the WMAP satellite to be [8]

$$\delta_{CMB} = \frac{\delta T}{T} \propto 10^{-5} \quad (1.31)$$

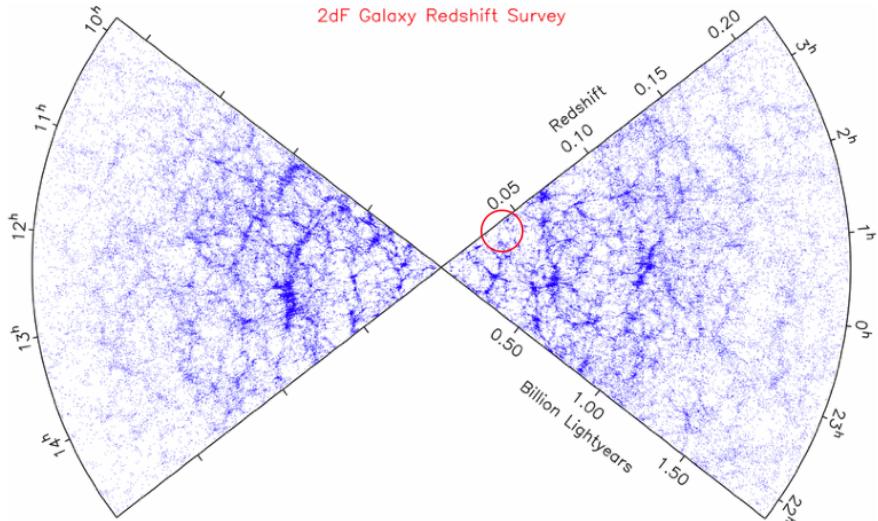


Figure 1.6: Large scale structure of the Universe.
Redshift cone plot a of the galaxies distribution in the Universe at large scales made by the Anglo-Australian Observatory. Every blue point corresponds to a galaxy. The earth is inbetween both cones [1].

Simulations show that, in order to explain the large scale structure of todays Universe, a fluctuation of matter density

$$\delta_{\rho_{mat,0}} \propto 10^{-3} \quad (1.32)$$

would be necessary in the early Universe. This higher density-fluctuations can be obtained assuming a dark matter-component, which did not interact with photons, and hence was allowed to clump together earlier serving the baryonic matter as

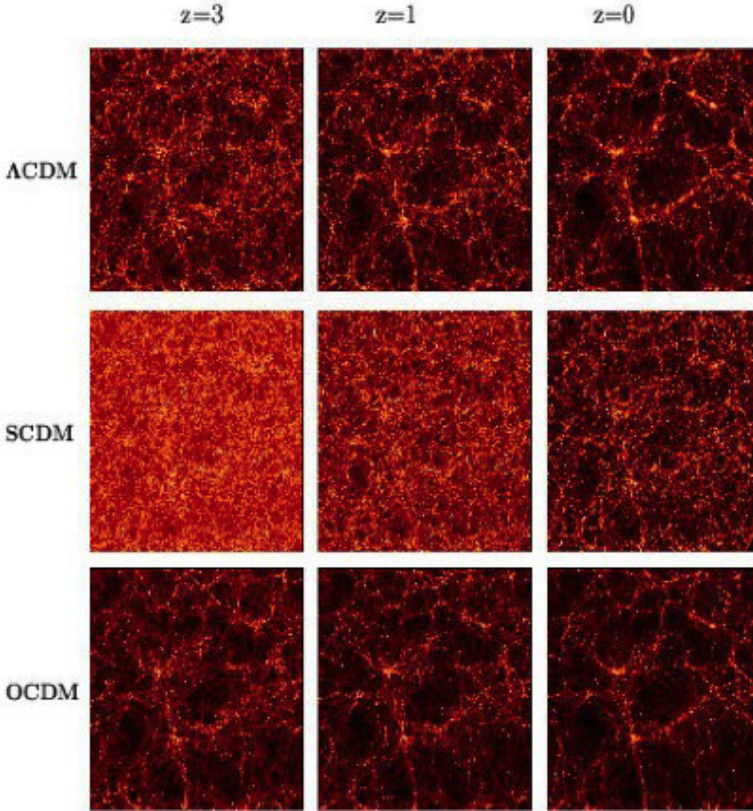


Figure 1.7: Large scale simulation models.

Cosmic density fields simulated for three different cosmic models ΛCDM , SCDM and OCDM. The resulting mass distributions are shown for three different redshifts [9].

gravitational seeds. In order to figure out which fraction of the dark component is necessary to achieve the structure of todays Universe, numerical n-body simulations were performed, testing different cosmological models. In Figure 1.7 we see the result of simulations made by the Virgo-collaboration. Three tested cosmological models are shown ΛCDM , SCDM, OCDM. The corresponding cosmological parameters are listed in Table 1.1. All three models differ more and more with increasing z-values.

ΛCDM is a reality-concording model with a matter density (baryonic + dark) of 30 % and 70 % dark energy. Only a small fraction of Ω_m is considered as baryonic matter. The other two models describe the standard model (SCDM) and an open Universe (OCDM) with $k < 1$ corresponding to equation (1.14).

model	Ω_m	Ω_Λ
ΛCDM	0.3	0.7
$SCDM$	1	0
$OCDM$	0.3	0

Table 1.1: Cosmological parameters used in simulations for three different Universe-models.

Gravitational lensing

In general relativity, gravity is described as a space-time distortion which causes that a light beam following a straight trajectory in the distorted space-time shows a deflection to outstanding observers. 1918 Arthur Stanley Eddington succeeded to proof this effect during a solar eclipse. The angle of deflection is depending on the mass of the gravitational lens and the distance R of the light beam to the center of the gravitation source, hence the mass M of a lensing object can be determined by measuring the deflection angle ϵ of light coming from objects lying behind this lens.

$$M \approx \frac{\epsilon R c^2}{2G} \quad (1.33)$$

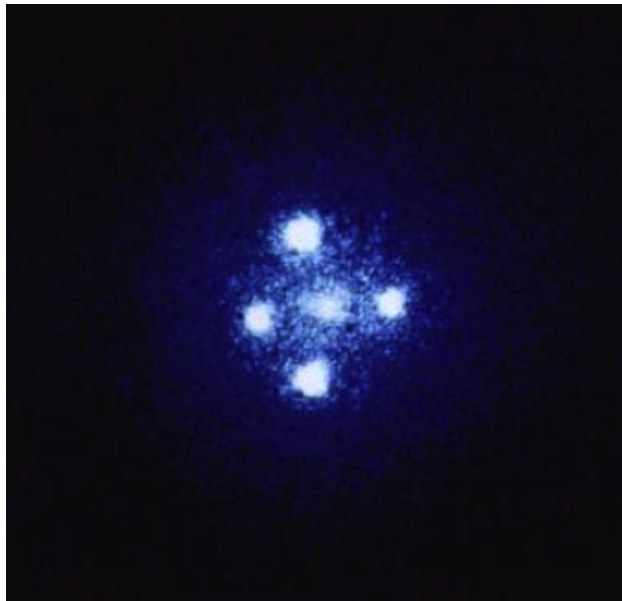


Figure 1.8: Einstein Cross G2237+0305

The four images around the central galaxy have the same redshifts, which indicate that they are multiple images of one object, which was identified to be a quasar whose light have been gravitationally lensed by the central galaxy.

The lensing object can be a single star as well as a whole galaxy-cluster. Ex-

amples are shown in Figure 1.8 and 1.9. Figure 1.8 shows a Quasar lensed by a galaxy, known as the G2237+0305 Einstein Cross. A ring-symmetry in the lensed image can be only achieved by a lens with symmetric geometry and without big density fluctuations.

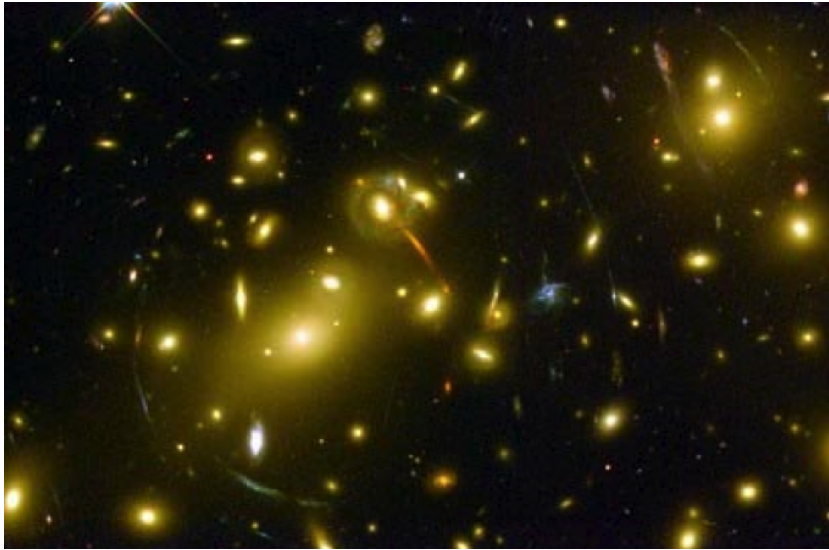


Figure 1.9: The Abell 2218 Cluster.

This cluster acts as a gravitational lens. The arcs of light are from distant galaxies which lie behind the cluster, whose light has been distorted and magnified by the gravitational potential of the cluster.

Figure 1.9 shows an image of the Abell 2218 cluster showing up some light arcs, which can be interpreted as deflected light from objects lying behind the cluster.

Microlensing

Another gravitational-lensing phenomena is the effect of Microlensing. This effect is appears, when a **Massive Compact Halo Object** (MACHO) crosses the line of sight between the observer and the lens, causing an increase of light-intensity. This phenomena can be distinguished from other events which show also an fluctuating intensity behavior by its unique characteristics :

- achromatic but strong intensity increase
- curve of light which is symmetric in time
- event shows up only once

Figure 1.10 shows a microlensing event OGLE-2003-BLG-423 [10] with an maxi-

mum magnification of

$$A_{max} = 256 \pm 43$$

A planet is assumed to be responsible for this lens-effect. Gravitational lensing could be in principle used to determine the total mass of the Universe. Unfortunately this method demands geometrical conditions which can be only satisfied by chance, which makes this phenomena to be very rare.

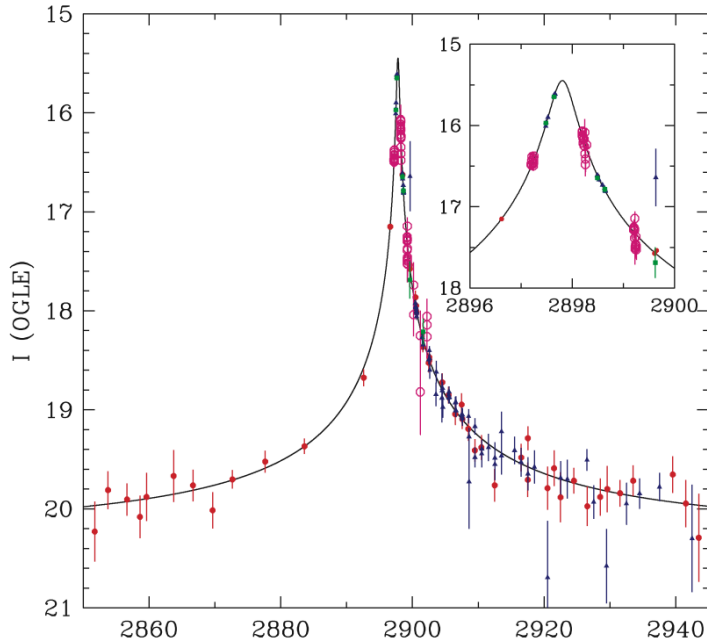


Figure 1.10: Microlensing effect.
Light curve of an microlensing event, OGLE-2003-BLG-423 [10].

Bullet Cluster

Recently, an impressive evidence based an gravitational lensing was adduced. The stellar-mass component of a galaxy is about 1-2 %. Much higher (5-15 %) is the fraction on galaxy-mass in form of gas or plasma [11]. The rest is probably made of dark matter.

In Figure 1.11 one can see two colliding galaxy-clusters, whose galaxies behave as collisionless particles, while the gas of both heats up due to electromagnetic interaction, inducing a plasma and emitting X-rays. The green contours show a gravitational potential map performed by gravitational lensing. In the case that both clusters contain no Dark Matter, the potentials would trace the dominant and visible cluster-component, which is the hot plasma. The right picture shows more then clearly a decoupling of the hot plasma from the stellar cluster-component, whereas the potential contours follow not the presumable dominant plasma, but

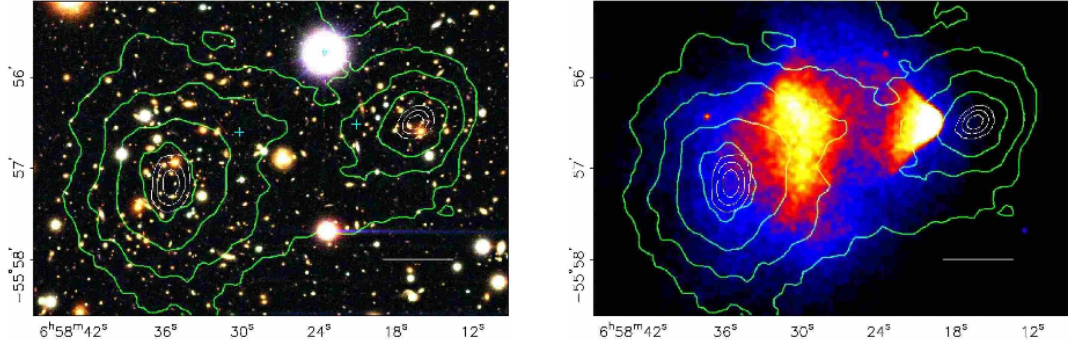


Figure 1.11: Bullet cluster.

The stellar, visible component of both colliding galaxy clusters is shown on the left. The right picture shows the decoupled hot plasma. Green contours in both pictures show the gravitational potential map, which indicate that the overwhelming mass of the clusters is invisible. Figure from [11].

the stellar baryonic component. Evidently there is a spatial coincidence between a dark matter component and the stellar component, which both contribute by far the biggest part of the clusters mass.

1.3 Dark Matter Candidates

It is estimated from the big-bang nucleosynthesis that only 4.4 % of the total content of the Universe consists of baryonic matter. The other 95.6 % consist of matter and energy of an unknown nature. This is a provocation to snoopy human beings and its identification is a big challenge. Let's take a look at possible candidates.

1.3.1 Baryonic Dark Matter

There is no doubt that baryonic matter is also a part of Dark Matter. This part is composed of planets, neutron stars, black holes, brown dwarfs, MACHOS and gas and dust, that sometimes can be seen in absorption and emission lines anyway. Recent developments allowed even to discover planets in other solar systems, but discovering them is still very difficult and needs a good portion of luck. The total baryonic matter density Ω_{bar} consists of the visible baryonic matter like stars and ionized gas Ω_{lum} and its baryonic dark component Ω_{bdm} :

$$\Omega_{bar} \equiv \Omega_{lum} + \Omega_{bdm} \quad (1.34)$$

Ω_{lum} can be determined by the luminosity density of the Universe and was estimated by Fukugita et al [12] to be

$$\Omega_{lum} = (0.0027 \pm 0.0014) \cdot h_0^{-1} \quad (1.35)$$

assuming $h_0 = 0.75 \pm 0.15$ this leads to a luminous baryonic matter density of

$$\Omega_{lum} = 0.0036 \pm 0.0020 \quad (1.36)$$

Furthermore the baryonic component was determined by regarding all visible matter, estimating its mass via the mass-to-light relationship and summing them [12] resulting in

$$\Omega_{bar} = 0.021 \pm 0.007 \quad (1.37)$$

This is in very good agreement with the theoretical cross-check. The primordial nucleosynthesis gives a constraint on Ω_{bar} regarding the abundances of 4He and 7Li in the primordial state, resulting in a baryon density [13] of

$$\Omega_{bar} = (0.0019 \pm 0.002)h_0^{-2} = 0.028 \pm 0.012 \quad (1.38)$$

with $h_0 = 0.75 \pm 0.15$

This means that if $\Omega_{tot} \approx 1$, then all baryonic matter in the Universe makes up around 3% of the total mass and a big part of it is not visible. Thus, it is obvious that baryonic matter alone cannot upset enough gravitational potential to explain the observed structure formation of the Universe.

1.3.2 Non-Baryonic Candidates

Neutrinos

Neutrinos are weakly interacting particles, whose existence is unquestioned. Unfortunately it is not easy to determine their fraction on Ω_{tot} , because the rest mass m_ν of neutrinos is still an open question. There are three neutrino-species ν_e, ν_μ, ν_τ , hence their density Ω_ν can be written as

$$\Omega_\nu = \left(\frac{\sum m_\nu c^2}{93.8 \text{eV}} \right) \cdot h_0^{-2} \quad (1.39)$$

here the critical density $\rho_{crit} = \frac{3H_0^2}{8\pi G}$ was used.

If these particles are massless, then their behaviour would be comparable to that of photons. They would stay relativistic forever, and Ω_ν would be a part of the radiation density $\Omega_{rad,0}$,

$$\Omega_{rad,0} = \Omega_\nu + \Omega_\gamma \quad (1.40)$$

If on the other hand neutrinos are massive and non-relativistic particles, then they must be added to the pressureless matter density

$$\Omega_{m,0} = \Omega_{bar} + \Omega_{CDM} + \Omega_\nu \quad (1.41)$$

Ω_{CDM} (Cold Dark Matter) represents the density of other than neutrinos, non-relativistic dark matter particle candidates. In this case (depending on their mass)

neutrinos could play an important role on structure formation in the Universe. Upper limits on neutrino masses were found to be [14]

$$m_{\nu_e}c^2 < 2.2eV, m_{\nu_\mu}c^2 < 0.19MeV, m_{\nu_\tau}c^2 < 18MeV \quad (1.42)$$

Simulations show a good agreement with observations at $\Omega_\nu \approx 0.16$ which implies an effective neutrino mass of [15]

$$m_\nu c^2 \leq 5.5eV \quad (1.43)$$

Since neutrino oscillations have been reported, it is obvious that the neutrino mass is higher than just zero. New limits on neutrino masses can be achieved by double-beta decay experiments like GERDA.

Axions

Axions were postulated as a consequence of the strong-CP problem in quantum chromodynamics (QCD). The QCD Lagrangian

$$\mathcal{L}_\Theta = \Theta \frac{\alpha_s}{8\pi} F^{\mu\nu a} \tilde{F}_{\mu\nu}^a \quad (1.44)$$

contains a dimensionless free parameter Θ , whose value must be $\lesssim 10^{-9}$ in order to not violate current limits on the electric dipole moment of the neutron. The reason for such a small value of Θ is supposed to be a spontaneous breaking of the PQ-symmetry giving a rise for a new particle - the Axion.

Axions can solve the strong CP problem and in addition fulfill the requirements for a dark matter candidate. They interact weakly with baryons and are non-relativistic. An interesting property is also that they could decay into photons, which depending on their rest-mass and its two-photon coupling strength $g_{a\gamma\gamma}$ could represent a part of the extragalactic background light. Its mass m_a is currently estimated to be [2]

$$6\mu eV < m_a < 2500\mu eV \quad (1.45)$$

and its density Ω_a

$$0.05 \lesssim \Omega_a h^2 \lesssim 0.5 \quad (1.46)$$

Obviously axions alone can not represent the total amount on dark matter in the Universe.

WIMPs

Weakly Interactive Massive Particles (WIMPs) are hypothetical, weak interacting particles which are supposed to have been already non-relativistic during their decoupling from the primordial plasma in the early Universe. The interaction strength of a WIMP is comparable to that of neutrinos, but in contrast to neutrinos its mass exceeds those of baryons. WIMP candidates arise also from the

supersymmetric (SUSY) model, which predicts for every fermion a new bosonic superpartner. As the heavier supersymmetric particles would annihilate after the Big Bang, only one supersymmetric WIMP is regarded as a favor candidate for Dark Matter. The **lightest supersymmetric partner** (LSP) - the neutralino χ^0 . This particle is a superposition of the fermionic superpartners of the Higgs and neutral gauge bosons.

$$\chi^0 = a\tilde{\gamma} + b\tilde{Z} + c\tilde{H}_1^0 + d\tilde{H}_2^0 \quad (1.47)$$

Its mass m_χ was estimated by accelerator experiments and astrophysical considerations [16] to be

$$45GeV < m_\chi < 3TeV \quad (1.48)$$

Vacuum Energy

In general relativity, vacuum energy appears as a simple constant in the field-equations

$$\Re_{\mu\nu} - \frac{1}{2}\Re g_{\mu\nu} = -\frac{8\pi G}{c^4} \cdot T_{\mu\nu} + \Lambda g_{\mu\nu}$$

Observations of distant supernovae and fluctuations in the CMB indicate that

$$\Omega_{\Lambda,0} = \frac{\Lambda c^2}{3H_0^2} \approx 1$$

In quantum mechanics, the vacuum-state can be regarded as a ground state of all possible fields, and therefore

$$\Omega_{\Lambda,0} > 0$$

seems to be a naturally given condition. Regrettable, this is the endpoint of agreement between theory and observation.

A lot of effort has been done to implement Λ_0 in QCD, GUT (grand unified theory) and other theoretical concepts like higher dimensional gravity, a variable Λ_0 or phenomenological models. All this attempts ended with one result: an impossibly high Λ_0 value, without any conformity to observational results. Although Λ_0 's right to exist is manifested in general relativity and cosmology (it determines the expansion rate, is related to the energy density etc.), the question of interpreting it physically remains still open and mysterious.

1.4 Direct detection of Dark Matter

WIMPs are expected to be trapped inside galaxies by gravitation. Their density profile in our galaxy should correspond to those determined in other spiral galaxies by rotation-curves and their mean velocity can be expected to be similar to the mean velocity of the stars around the galaxy-center.

This Dark matter could possibly be detected indirectly by annihilation processes and hence searching for gamma-rays, neutrinos, antiprotons or other annihilation products in regions where one can expect a lot of WIMPs (e.g. galaxy center, galactic halo) is the one way to detect WIMPs. This method is more suitable for WIMP-masses $\approx 200\text{GeV}$. The other way is to detect them directly on earth. The cross section of an WIMP interaction with baryonic matter is depending on its mass and velocity, but generally it should be similar to that of Weak Interaction. Looking for elastic nuclear recoils between WIMP and baryonic matter and measuring the deposited energy is hence a reasonable way to detect Dark Matter candidates.

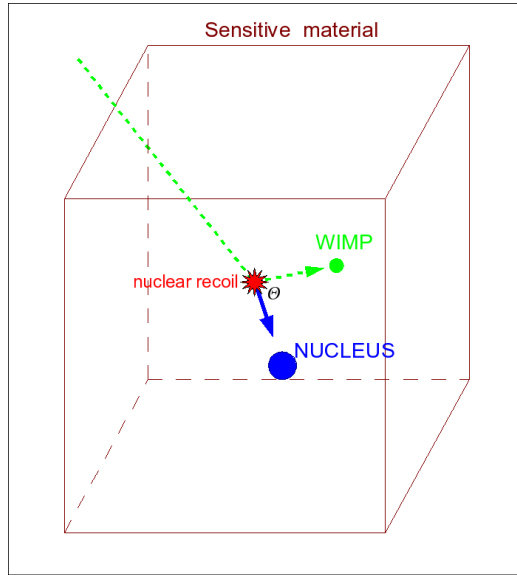


Figure 1.12: Principle of a WIMP detector.

An incoming WIMP scatters in the detector material (e.g. a Ge crystal) transferring a part of its energy to the hitted nucleus.

The momentum transfer q to the nucleus due to a WIMP collision is given by

$$q = 2\mu_r \cdot v \cdot \cos\Theta \quad (1.49)$$

where μ_r is the reduced mass of the system

$$\mu_r = \frac{m_\chi m_{nuc}}{m_\chi + m_{nuc}} \quad (1.50)$$

m_χ is the WIMP mass and v its velocity. The energy transfer Q is depending also on the nucleus mass m_{nuc} . With

$$Q = \frac{q^2}{2m_{nuc}} \quad (1.51)$$

, the differential rate $\frac{dR}{dQ}$ can be written as [17]

$$\frac{dR}{dQ} = \frac{\sigma_0 \rho_0}{2m_\chi \mu_r^2} F^2(Q) \int_{v_{min}}^{\infty} \frac{f(v)}{v} dv \quad (1.52)$$

where $\rho_0 = 0.3 GeV/c^2/cm^3$ [17] is the assumed halo WIMP-density, σ_0 is the total WIMP cross section in the detector material, $F(Q)$ is the nuclear form factor and $f(v)$ the dark matter velocity distribution which can be assumed to be of Maxwellian form [18] in the galactic frame

$$f(v, v_E) \propto \exp\left(-\frac{|v + v_E|^2}{v_0^2}\right) \quad (1.53)$$

Here v_E is the earth-velocity in the dark matter halo and v_0^2 a characteristic velocity given by

$$k_B T = \frac{1}{2} m_\chi v_0^2 \quad (1.54)$$

according to the galactic rotation velocity (Milky Way) of $\approx 230 \frac{km}{h}$.
The energy of a nuclear recoil can be deposited by

- ionization,
- scintillation,
- phonon-energy,

however the expected low rates for such events ($\frac{1-10^{-5}}{day \cdot kg}$) [16] and their low energy transfer require an environment shielded from radioactivity and cosmic rays, furthermore gross detector-masses, a low energy-threshold in the detectors and an effective discrimination against remaining background-signals is essential. The required low background makes underground facilities a reasonable place for direct Dark Matter search.

Three factors are helpful to discriminate background signals. The rotation of the earth around the sun helps to distinguish possible WIMP-signals from background by inducing an annual modulation in the detector signals. Similarly, a second modulation should rise up due to the day-night cycle. These modulations, if they exist are very hard to measure and an easier way is to use at least two target-materials, which due to their different cross-sections yield in different event-rates.

Germanium based detectors which were already used in double-beta-decay experiments were used first in order to search for WIMPs. These detectors are characterized by very good resolution and low threshold energies of about 5-10 keV, but a production of large and low-purity crystals meets with technical and/or financial limits.

Even though massive Ge-detectors are not available, impressive results were obtained, running them in cryogenic-experiments. This combination allows to measure phonon- and ionization-signals simultaneously and to distinguish nuclear recoils caused by WIMPs or neutrons from electron recoils. The first cryogenic experiment was operated by the CDMS-collaboration, which in addition used two different target materials - **Ge** and **Si**.

Much bigger masses are available with **NaI** scintillators. Around 100 kg of this material was operated by the DAMA collaboration, which first claimed in 1997 to detect an annual modulated WIMP-signal shown in Figure 1.13.

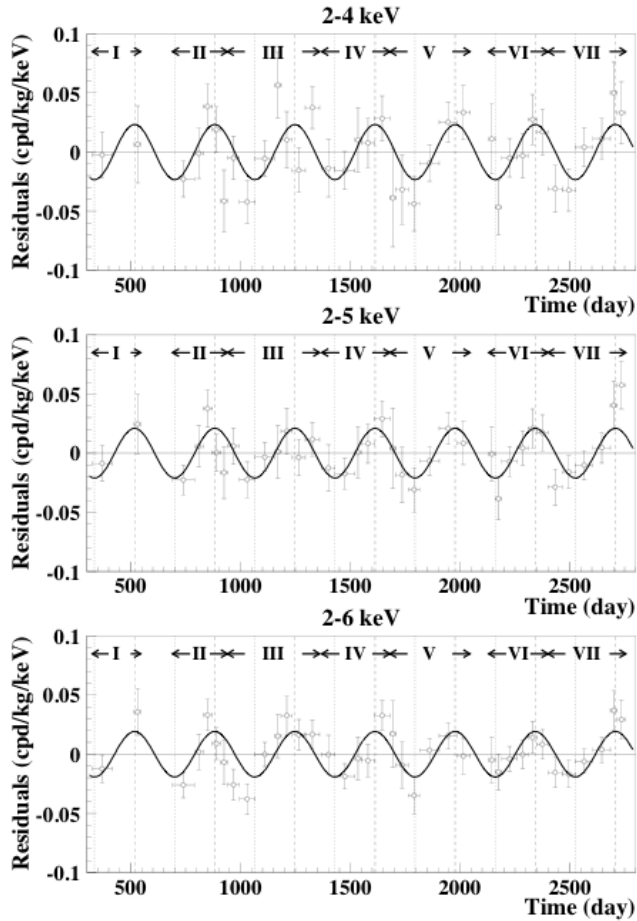


Figure 1.13: DAMA modulation.

Single count-rates as a function of time for a period of seven years measured by the DAMA collaboration since 1997 [19].

Although better limits on cross-sections have been achieved meanwhile, unfortunately the DAMA result couldn't be clearly confirmed by any other WIMP-search experiment like ZEPLIN, Edelweiss or CDMS and hence the origin of the modulation is assumed to come from some other annual-modulated phenomena, but not from WIMPs.

Another favored detector-material is liquid-Xe. The mass of a detector, based on liquid Xenon can be easily increased and its big atomic number ($A=131$) enhances the sensitivity-limits for spin-independent particles. Although this is generally an advantage, the formfactor for Xe is dropping rapidly around 90 keV reducing the event rates in equation (1.52) for nuclear recoils around this energy.

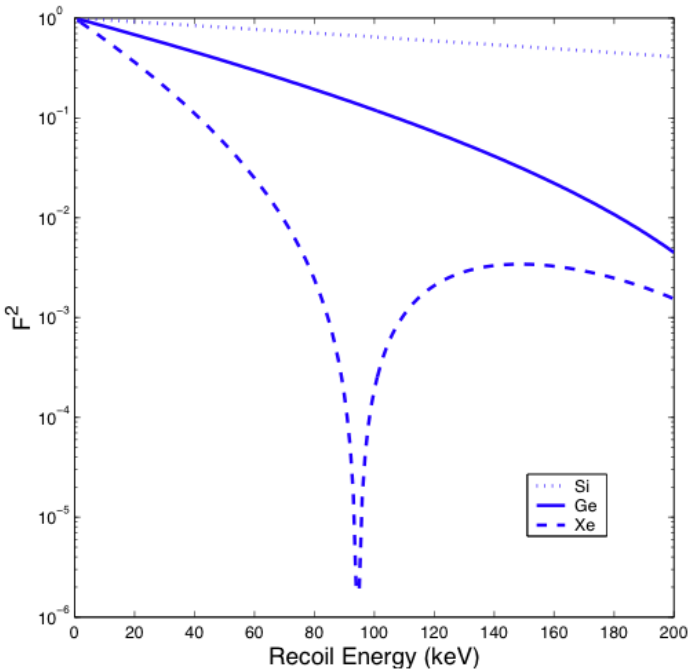


Figure 1.14: Formfactors of Si, Ge and Xe.

Although the high atomic number of 131 for Xe is an advantage, its formfactor is lower than this of Ge and Si and drops rapidly around 90 keV [18].

XENON10 in Gran Sasso, Italy is an example for a Xe based dark-matter-search experiment. This experiment is non-cryogenic, hence phonon-signals can not be measured, but its ionization and scintillation signals can be measured simultaneously, which allows to easily discriminate ionizing particles like photons from the background.

Chapter 2

CDMS I, II, SuperCDMS

2.1 CDMS I at SUF

CDMS I was the first cryogenic dark matter search experiment, operating four Ge and two Si detectors at temperatures $\leq 40mK$ with the capability to measure both, the phonon and the ionization signals caused by recoil events. Electron recoil events near the surface of the detector crystal can mimic nuclear recoils because of insufficient charge collection and hence the discrimination of such events is relevant. This can be achieved by timing- and pulseshape- analysis of the phonon signals, which allows to reconstruct the recoil positions. Other cuts and discrimination efficiencies were also determined and tested at SUF first. CDMS I started in 1998 and was running until 2002, at the shallow site in the Stanford Underground Facility (SUF) with poor muon shielding, in order to investigate the neutron background and to derive dark matter limits. The SUF lab is 10.6 m under the surface (17m water equivalent), which reduced the hadronic component of the cosmic rays flux by a factor of ~ 1000 to negligible values, whereas the muon flux was reduced by factor ~ 4 from $180 \text{ muons}/\text{m}^2/\text{s}$ to $44.4 \text{ muons}/\text{m}^2/\text{s}$ [20], and thus the main background arisen from neutrons, produced by muon-interactions within the rock of the shallow-side by muon capture reactions like

$$\mu^- + p \rightarrow p^* \rightarrow n + \nu_\mu \quad (2.1)$$

In addition, fast neutrons can produce neutrons indirectly by inducing electromagnetic showers, whose products undergo (γ, n) or $(\gamma, x \cdot n)$ reactions. Such neutrons can be produced also at deeper site in contrast to the neutrons from slow muon capture reactions like this in equation (2.1). Another source of background was given by natural radioactivity in the rock and in the detector components, by nuclides from ^{238}U , ^{232}Th , ^{40}K chains. Event rates caused by this background were $\sim 1\text{event/kg-day}$ [21] and hence additional polyethylene, lead and muon-veto-scintillators were installed in order to dam up this background.

In Figure 2.1 the shielding assembly and the dilution refrigerator at SUF is shown schematically. The scintillator muon vetos reject products of muon interac-

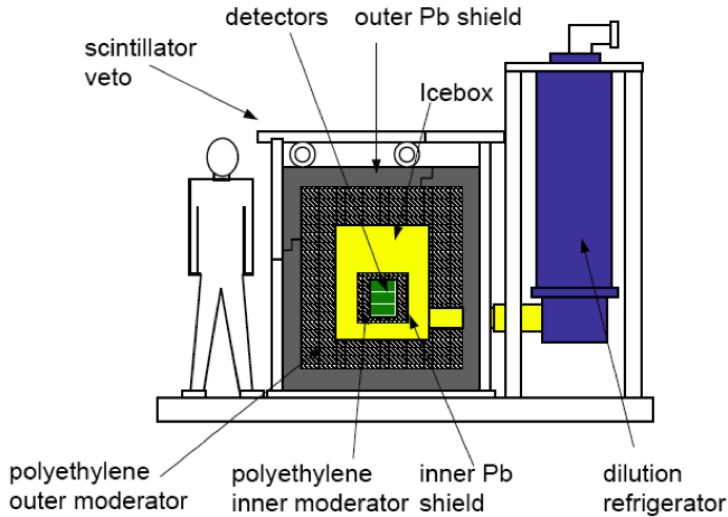


Figure 2.1: CDMS shielding at SUF.

Scheme of the Pb and Polyethylene shields locations at SUF. Also shown are the active muon vetos and the dilution refrigerator. Figure from [23].

tions with an efficiency of 99.99 %. Furthermore a 15 cm thick outer lead, a 25 cm thick outer polyethylene shield followed by 43 kg of inner lead and 11 kg polyethylene were installed, reducing the gamma rates to ~ 1 event /keV/kg/day and the neutron rates for energies between 5 and 100 keV to 0.001 events/keV/kg/day [22]. Between 1998 and 1999, promising exclusion limits for WIMP-interactions were determined at SUF and although these were inconsistent with those determined by the DAMA collaboration, further analysis and finally other dark matter experiments confirmed the limits at SUF, which were the best in 2001 for a WIMP-mass range of $10\text{--}70 \text{ GeV}/c^2$.

2.2 CDMS II at Soudan

CDMS II started its run with the 6 SUF-detectors in 2003 in an underground facility in the Soudan-mine, Minnesota at a depth of 780 m (2090 m water equivalent). Subsequently runs with four additional towers containing 6 detectors respectively were performed, accumulating 19 Ge (each 250 g) and 11 Si (each 100 g) altogether. Same as at the SUF shallow side, the limiting neutron background is arising from muon interactions within the surrounding cavern-rock and from natural radioactivity, though the deep underground position of the detectors reduced the muon flux by a factor of $5 \cdot 10^4$ and the neutron background by a factor of

300 to ~ 1 event/kg/year, making the Soudan mine a reasonable place for WIMP-searching with expected rates of $< 1 \text{ event/kg/day}$ [24].

The detectors are operated at 50 mK cooled by a dilution refrigerator, which is placed together with the detectors and its shields inside a RF-shielded, class 10.000 clean-room. All supplies, control systems and most of the readout-electronics are located outside the RF-room. Physical presence of the operators can not be established over 24 hours the day, because of limited entrance to the underground-lab., hence a computer room at the surface allows remote control of the cryogenic- and data-acquisition- systems at any time. CDMS II will be run through 2007 and start the operation of the new-generation Super-CDMS detectors in 2008-2009.

2.3 Super CDMS at SNOLAB

Super CDMS, a seven tower and 25 kg experiment is a further development of CDMS planned for ~ 2010 . Presumably, its sensitivity will be a factor of two better over other existing experiments. The improvements include mainly cleaner and 2.5 times larger in mass detectors compared to those used in CDMS II. Furthermore

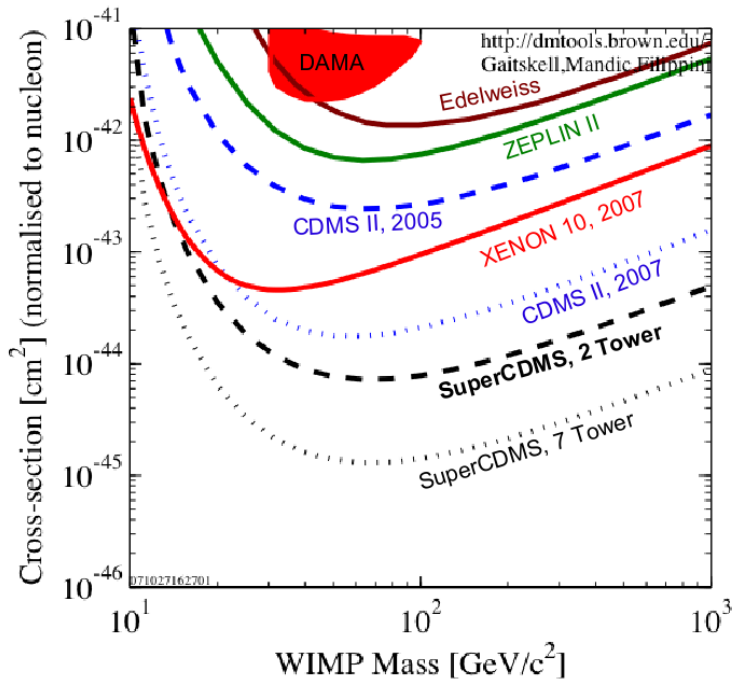


Figure 2.2: Limits on cross sections.

Limits on spin independent WIMP interactions for different experiments. The two lower lines show possible limits for the projected two tower SuperCDMS at Soudan and the 7 tower SuperCDMS at SNOLAB [25].

an even more reduced muon-induced neutron background will be achieved, due to the new deeper location at ~ 2 km depth (6010 m water equivalent) at SNOLAB. The first two towers of Super CDMS are planned to be run still in Soudan, followed by the 7 towers runs beginning at SNOLAB in 2010-2012. Cross sections of $1.3 \cdot 10^{-45} cm^2$ for WIMP recoils are expected at a WIMP mass of $60 GeV/c^2$.

2.4 Inner Life of CDMS II

2.4.1 The Zip Detectors

The heart of every CDMS-experiment is its ZIP (Z-sensitive Ionization and Phonon mediated)-detector. Figure 2.3 shows a CDMS ZIP detector, consisting of high-purity Ge or Si crystals. Each of the Ge-ZIP has a mass of 250 g, whereas the mass of each Si-ZIP is 100g.



Figure 2.3: ZIP detector.

Top side of a ZIP (Z-dependent Ionization and Phonon) detector which is 7.62 cm in diameter and 1 cm thick, mounted in a copper housing. The structure on the surface shows the photolithographically patterned phonon sensors.

Particles hitting the Si or Ge ZIP-crystal interact with a nucleus or an electron loosing energy by inducing lattice vibrations (phonons) or charge excitation

(ionization). Both energy losses can be measured simultaneously by a ZIP event by event, which allows to discriminate many particles by the detector's response they cause. Photons and charged particles e.g. interact electromagnetically and are involved in electron-recoils, which produce a higher ionization signal. Weak interaction particles like neutrons or WIMPs undergo nuclear recoils resulting in low ionization signals. The ionization signal is measured by one inner and one outer ionization electrode on the bottom side of the detector shown in Figure 2.4. The outer electrode is a ring, whose function is to reject events in the detectors outer regions. This events are generally considered as bad events for several reasons:

- the electric field at the edge is not uniform, which influences the ionization signal.
- the phonon sensors on the other detector side do not cover the complete detector surface at the edge, hence the ionization to phonon-energy ratio is disturbed.
- the inner detector side is shielded by other detectors in the assembly, in contrast to the outer regions.

The inner electrode is in effect the one measuring the ionization signal. During an ionization process, an electric field applied across the detector causes the electrons-hole pairs to drift towards the electrodes, resulting in a current I_0

$$I_0 = \sum \frac{e}{d} (v_{e^-} + v_{e_hole^-}) \quad (2.2)$$

where v_{e^-} and $v_{e_hole^-}$ are the drifting velocities of the electrons and electron-holes, d is the crystal-thickness and e is the electrical charge. The ionization energy E_Q given by this charges is defined as

$$E_Q \equiv N_Q \cdot \epsilon \quad (2.3)$$

where N_Q is the number of electron-hole-pairs produced by an recoil event and ϵ is the average energy needed to product an electron-hole pair in the crystal.

$\epsilon \approx 3.0\text{eV}$ for Ge

$\epsilon \approx 3.8\text{eV}$ for Si

The drift of this charges gives rise to additional phonon-excitation, called the Neganov-Luke phonons and hence the total phonon energy is a sum of the recoil-phonons and Neganov-Luke phonons.

$$E_{ph-tot} = E_{ph-rec} + e \cdot N_Q \cdot V_b \quad (2.4)$$

where E_{ph-tot} is the total phonon energy, E_{ph-rec} is the recoil phonon energy and

$$e \cdot N_Q \cdot V_b = \frac{eV_b E_Q}{\epsilon} \quad (2.5)$$

the Neganov-Luke phonon energy, which depends on the bias voltage V_b applied to the crystal.

The recoil energy E_R of an event can be thus determined by

$$E_R = E_{ph-tot} - \frac{eV_b}{\epsilon} E_Q \quad (2.6)$$

In practice the phonon measurement is performed by QET's (Quasiparticle-assisted Electrothermal feedback Transition-edge sensors), made of Aluminum and Tungsten thin films, which are patterned on the ionization-electrodes opposite site of each ZIP.

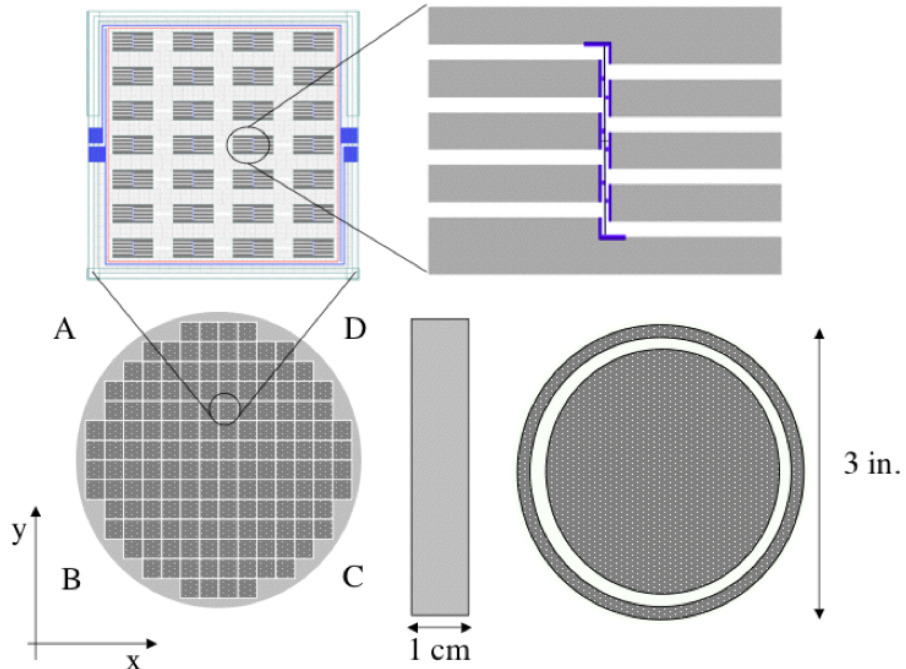


Figure 2.4: Scheme of a ZIP detector.

Bottom right shows a large ionization inner electrode and an outer ring electrode, which allows to discriminate against events in the outer regions of the ZIP. Bottom left shows the pattern of phonon sensors on the opposite detector side divided into four channels A,B,C,D consisting of QET's. Top left shows a zoom in of one die, which consists of 28 QET's. Each QET consists of a $1\mu m$ wide tungsten strip connected to 8 aluminum fins, shown at top right.

Figure from [26].

The QET patterned surface is divided in four sections A,B,C,D (see Figure 2.4) serving as four separated phonon channels. Each of this channels consist of

1036 QETs. One QET in turn consists of $1 \mu\text{m}$ wide, superconducting tungsten thin film strips deposited on the crystal surface (called TES for Transition Edge Sensor). Their transition temperature lies between 70 mK and 130 mK. Phonons induced by a recoil cause a temperature-increase in the tungsten, resulting in a sharp resistivity increase.

A dimensionless ionization yield parameter y

$$y \equiv \frac{E_Q}{E_R} \quad (2.7)$$

is used to characterize the type of recoil, allowing to distinguish electron and nucleon recoils as shown in Figure 2.5. Although the ionization yield doesn't allow to distinguish between WIMP and neutron recoils, it makes a rejection of electron recoils very simple.

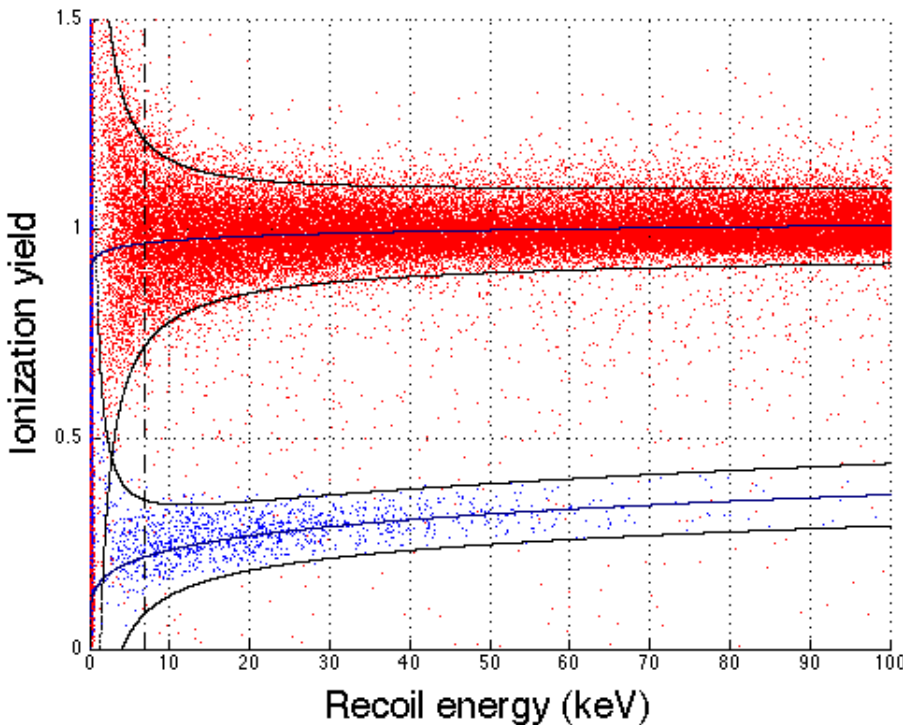


Figure 2.5: Yield bands.

Blue dots are nuclear recoils caused by ^{252}Cf neutrons, red dots are electron recoils caused by ^{133}Ba photons. The black lines represent the band fits and their means in blue. The dashed line represent the detector threshold energy of 7 keV.

2.4.2 Cryogenics

The cryogenic system shown in Figure 2.6 consists of the dilution refrigerator and six, cylindrical copper cans - the Ice Box, with the detectors placed in the innermost can. This can is connected to the mixing chamber of the refrigerator and can support up to seven towers with six ZIP detectors at base-temperature of < 50 mK. The only contact of the ZIP-detectors to the outside world is through a copper stem containing the wiring for the detector readout. The other cans are thermally coupled to the different temperature stages of the dilution refrigerator. Only low-background materials were used for the construction of the icebox. Each of this can is thermally coupled to the different temperatures stages of the dilution refrigerator establishing a temperature gradient in the icebox.

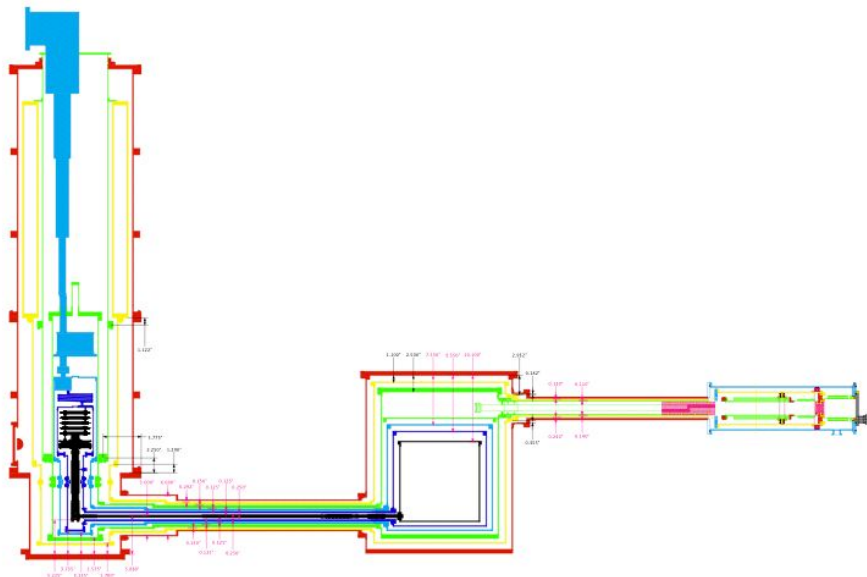


Figure 2.6: Scheme of the CDMS cryostat.

On the left the dilution refrigerator is shown connected to the icebox. Each frame of the icebox corresponds to a different temperature stage of 300K, 77K, 600mK, 50mK and 20mK from the outer to the most inner layer. The stem on the right contains the wiring, connecting the cold electronics with the roomtemperature electronics. Figure from [26].

2.4.3 Shielding and Muon Veto

The location of CDMS II reduced the neutron background from cosmic muons by a factor ~ 300 in comparison to the SUF location [24]. This neutron background is hence almost negligible. Anyway, the ice box is additionally surrounded by 22.5 cm of lead and 50 cm of polyethylene, in order to shield the remaining neutrons and photons from natural radioactivity.

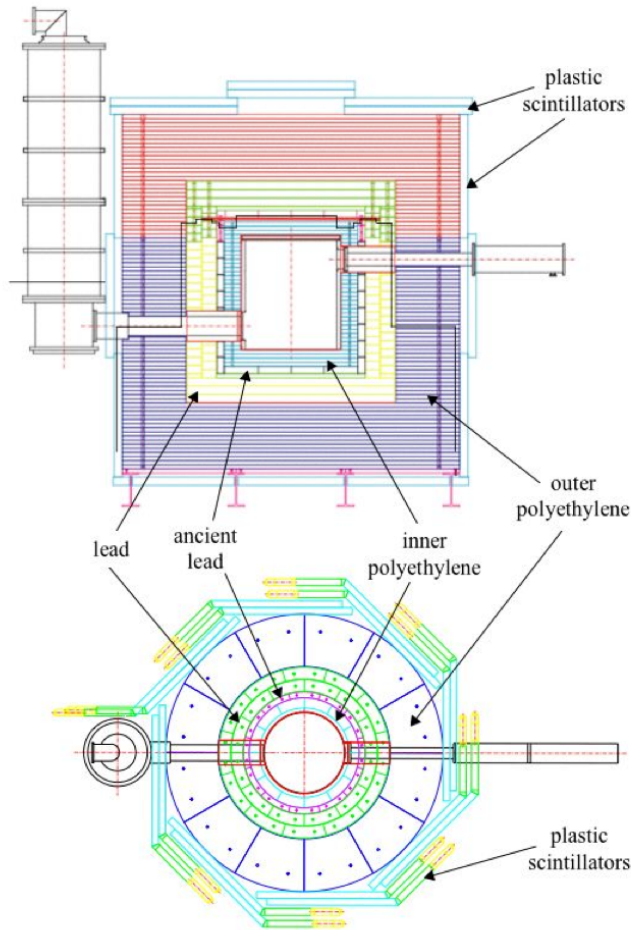


Figure 2.7: Scheme of the CDMS shielding.

Side and top view of the active and passive shields installed around the icebox. The cryostat on the left is connected to the icebox via the cold stem. On the opposite site the electronics stem is shown. Figure from [26].

Forty overlapping plastic scintillator paddles, made of Bicron BC-408 were placed all over around the shields establishing together with photomultiplier-tubes an active muon veto system. Events that happen in a $50 \mu\text{s}$ window during a

significant veto activity are expected to be of cosmogenic origin, and are hence discriminated. The polyethylene shields moderate low energy neutrons from radioactive decays to energies below $\sim 7\text{keV}$, which is the threshold energy of the detectors. The flux of other decay products, mainly photons is reduced by the massive lead layers. In addition a 2mm thick μ -metal shield surrounding the ice box is protecting the electronics and the detectors from external magnetic field influences.

2.5 Neutron backgrounds at CDMS II

In view of the low expected event rates for WIMP particles ($< 1\text{event/day/kg}$), it is essential for any direct dark matter search experiment to understand and effectively suppress or discriminate as much background as possible. As shown at the shallow side in SUF, active muon vetos and passive lead and polyethylene shields reject effectively α , β and γ backgrounds from natural radioactivity. A deep underground location of the detectors is of great importance for shielding against neutrons from cosmogenic-muon interactions. The main neutron-background in the Soudan mine is composed of neutrons from natural radioactivity, (α, n) reactions and muon-induced neutrons. Although the latter are able to pass the shields due to their high energies of more than 50 MeV, it is possible to estimate their rates by the different interaction probabilities for neutrons in Ge and Si. The fast-neutron spectra produced by muons-interactions in the rock can be described by

$$\frac{dN}{dE} = \begin{cases} 6.05 \cdot e^{\frac{-E}{77}} & \text{for } 50 < E < 200\text{MeV} \\ e^{\frac{-E}{250}} & \text{for } E < 200\text{ MeV} \end{cases} \quad (2.8)$$

where E is the neutron energy.

In order to estimate this background, simulations have been done considering the full CDMS-II assembly, resulting in

0.051 ± 0.024 events in Ge
 0.024 ± 0.011 events in Si

for the entire planned CDMS II exposure [24].

Besides the rock, muons interacting with the lead shields produce low energy neutrons, whose spectrum can be described by

$$\frac{dN}{dE} = \begin{cases} 0.812 \cdot E^{5/11} \cdot e^{-E/1.22} & \text{for } E < 200\text{ MeV} \\ 0.018 \cdot e^{-E/9} & \text{for } 4.5 < E < 50\text{MeV} \end{cases} \quad (2.9)$$

Simulations of this spectrum resulted in

1.94 ± 0.44 events in Ge

0.89 ± 0.18 events in Si

for the CDMS II exposure [24].

The reason for more nuclear recoil events in this case, is that there is only 10 cm of polyethylene between the detectors and the lead shield emitting the neutrons. In contrast to neutrons of cosmogenic origin, external neutrons from (α, n) reactions and spontaneous fission (SF) exhibit energies < 10 MeV and can be easily moderated by the polyethylene shields. The flux of this neutrons was reduced by a factor of $\sim 10^6$ by the 50cm thick polyethylene shield, which made this background negligible for CDMS II [24].

As the detector-technology and their sensitivities advances more and more, detailed characterizing of every possibly present neutron-background source could become increasingly relevant. Although high purity materials are used in constructing a detector, a rest contamination of this materials can not be avoided. (α, n) reactions and SF-reactions in the detectors components itself could become the dominant neutron-background in future. In the first instance neutrons from materials located within the shield assembly require besides a high-purity processing, an exact contamination monitoring, as this neutrons "bypass" even the best shields. That applies to the shield-materials too, which, even if they do a very good job concerning external background, they could constrain the detectors sensitivity by the presence of radioactive impurities inducing a considerable internal background.

2.6 Neutrons interactions with matter

In contrast to α , β or γ decays, neutron decays occur only indirectly through highly excited states, as by-products of nuclear reactions or by spontaneous fission (SF) and (α, n) -reactions. The energy loss during an interaction of charged particles in matter is dominated mainly by the coulomb force, hence neutron ranges in matter are much higher than for charged particles, like electrons or α particles and can traverse centimeters of material with no interaction, crossing e.g. a detector without leaving any signature. The rare neutron-interactions take place under the participation of a nucleus of the absorber material and maybe either scattered or absorbed in the target material releasing heavy charged particles as secondary radiations. The cross sections of such reactions are highly energy dependent.

2.7 Neutrons from (α, n) reactions

α particles of about 5MeV from high rate α -emitters such as ^{238}U and ^{232}Th , which are present in the Soudan-mine cavern-rock and the detector assembly as natural impurities, can lead to (α, n) -reactions inside a target material resulting in an undesirable neutron-flux in the detector. An example of such an reaction is



Although the range of α particles in materials is negligible, they can excite a near located nucleus, which deexcites by an neutron-emission, possibly nearby a detector. (α, n) -reactions are energetically possible if the α particle is able to penetrate the coulomb barrier U_c of the target-nucleus

$$U_c = \frac{Z_1 Z_2 e^2}{r_0 (A_1^{1/3} + A_2^{1/3})} \quad (2.10)$$

where $Z_{1,2}$ are the atomic numbers of the α -particle and the target nucleus, $A_{1,2}$ are their mass numbers and $r_0 = 1.2 \text{ fm}$ is a constant. Furthermore the α particle must be able to overcome the threshold energy, which is the difference in binding energies of the initial state nuclei and their final states. Such a reaction can take place for example in the Copper cans inside the icebox. The behaviour of α particles in materials, their differential energy-loss can be expressed by the stopping power P_s defined as

$$P_s(E) = -\frac{dE}{dx} \quad (2.11)$$

where dE/dx expresses the energy loss of the α particle at a distance dx in a material.

Analogically, the stopping power of a mixture of materials can be written as

$$P_s(E) = \frac{\sum_i P_i(E) N_i}{\sum N_i} \quad (2.12)$$

where P_i is the stopping power of the constituent i and N_i is its number of atoms per cm^3 . The energy loss ΔE of an α particle along a path of length L , can be written as

$$\Delta E = E_\alpha - E'_\alpha = \int_0^L (-\frac{dE}{dx}) dx \quad (2.13)$$

where E_α is the initial α -energy and E'_α its energy at L . For thin target materials which cause almost no energy loss the probability interaction for an (α, n) -reaction is [27]

$$N_i \sigma_i(E) dx = \frac{N_i \cdot \sigma_i(E) dE}{-\frac{dE}{dx}} \quad (2.14)$$

where N_i is the atom density of nuclide i and σ_i its (α, n) -cross section. Furthermore, the probabilities for (α, n) -reaction in thick target materials can be expressed by the thick-target neutron production function [27]

$$P_i(E_\alpha) = \int_0^{E_\alpha} \frac{N_i \sigma_i(E)}{(-dE/dx)} dE \quad (2.15)$$

The stopping power $-dE/dx$ can be expressed classically by the Bethe Bloch formula

$$-\frac{dE}{dx} = \frac{4\pi e^4 z^2}{m_0 v^2} N B \quad (2.16)$$

with

$$B \equiv Z \left[\ln \frac{2m_0 v^2}{I} - \ln \left(1 - \frac{v^2}{c^2} \right) - \frac{v^2}{c^2} \right] \quad (2.17)$$

where v is the velocity of the α particle, $z \cdot e$ its charge, m_0 the electrons rest mass, N and Z are the number density and the atomic number of the target material, and finally I is an experimentally determined parameter, which expresses the average excitation and ionization potential of the absorber. Equations (2.16) and (2.17) are generally valid for any kind of charged particles. Obviously the stopping power is increasing with higher charges of the particles and with higher electron densities NZ of the absorber. (α, n) neutrons with non-relativistic energies of some MeV show a $1/v^2$ dependence on velocity.

2.8 Neutrons from spontaneous fission

Besides neutrons from (α, n) reactions, neutrons from spontaneous fission of heavy elements like U or Th can be a noticeable neutron-source in future dark matter experiments. The process of spontaneous fission can be described by a liquid drop model proposed by Bohr and Wheeler. In this model, nuclear forces act similar like the surface tension in a droplet. In the droplet, electrostatic forces from protons act contrary to the surface tension and tend to make it unstable. The heaviest elements are in a state in which the surface tension is almost prevailed by the repulsion, and the droplet is barely held together in result. Fission occurs, if enough energy is supplied to such a barely stable nucleus exciting it over the ground-state and causing vibrations, which extend the stability limits. A separation in two fragments occurs emitting a number of attendant fission products like prompt neutrons and photons, which carry out the energy of the highly-excited fission fragments. From a quantum mechanical point of view, this process is similar to an α - decay, though it exhibits much lower decay-times. The energy-spectra of the neutrons emitted can be described by a Watt distribution [28]

$$N(E)dE = e^{-E/a} \sinh \sqrt{bE} dE \quad (2.18)$$

where E is the kinetic neutron-energy and a , b are evaluated, or experimentally determined parameters.

After the emission of the prompt neutrons, the fission fragments undergo further β^- decay processes emitting more neutrons, called **delayed neutrons**. Delayed neutrons yield about 1 % of the total number of emitted neutrons, hence dealing with their appearance is not of the highest priority.

The remaining heavy fission-fragments exhibit a very large charge, due to the loss of electrons during the fission process. As described by the Bethe-Bloch equation this results in a gross energy loss. The range of these fragments in a material is not that low anyway, because the higher energy-loss is partially compensated by the high initial energies. Additionally the electrons are collected during the track, reducing the effective charge of the fragments, which results in lower energy-losses. Hence fission fragments can reach values comparable to that of α 's anyway, and reach an μm order of magnitude, which makes them at the same time not dangerous to the detector assembly.

Chapter 3

The neutron calibration run with ^{252}Cf

3.1 GEANT4

GEANT4 is a FORTRAN based Monte Carlo simulation toolkit, developed since 1993 for high-energy physics by scientists from facilities like CERN, SLAC, or KAK. Despite the high-energy physics GEANT4 found a more and more wide application in medicine.

This software contains physics models for particle interactions including databases with particle cross sections and their transport properties and allows a wide variety of modelling complicated geometries. A CDMS-GEANT4 simulation has already been written mainly by the collaboration members from the University of Minnesota and used for simulations of different backgrounds and the corresponding detector responses. Previous simulations of CDMS included investigations concerning the optimal location for the calibration sources like ^{252}Cf or ^{133}Ba , in order to achieve best event -rates during the real calibrations. This could be done avoiding unnecessary activation of the detector material with a real calibration source. Further calibration simulations were done for testing the cut efficiencies applied to real data.

Figure 3.1 shows the side and top view geometry of the CDMS-II five tower experiment, which is used currently in the simulations. The green rectangles are the active veto panels. Horizontal red lines indicate the different passive polyethylene and lead shields, the blue lines indicate the Copper cans of the icebox, and finally in the center, towerguts including the ZIP detectors are shown in brown.

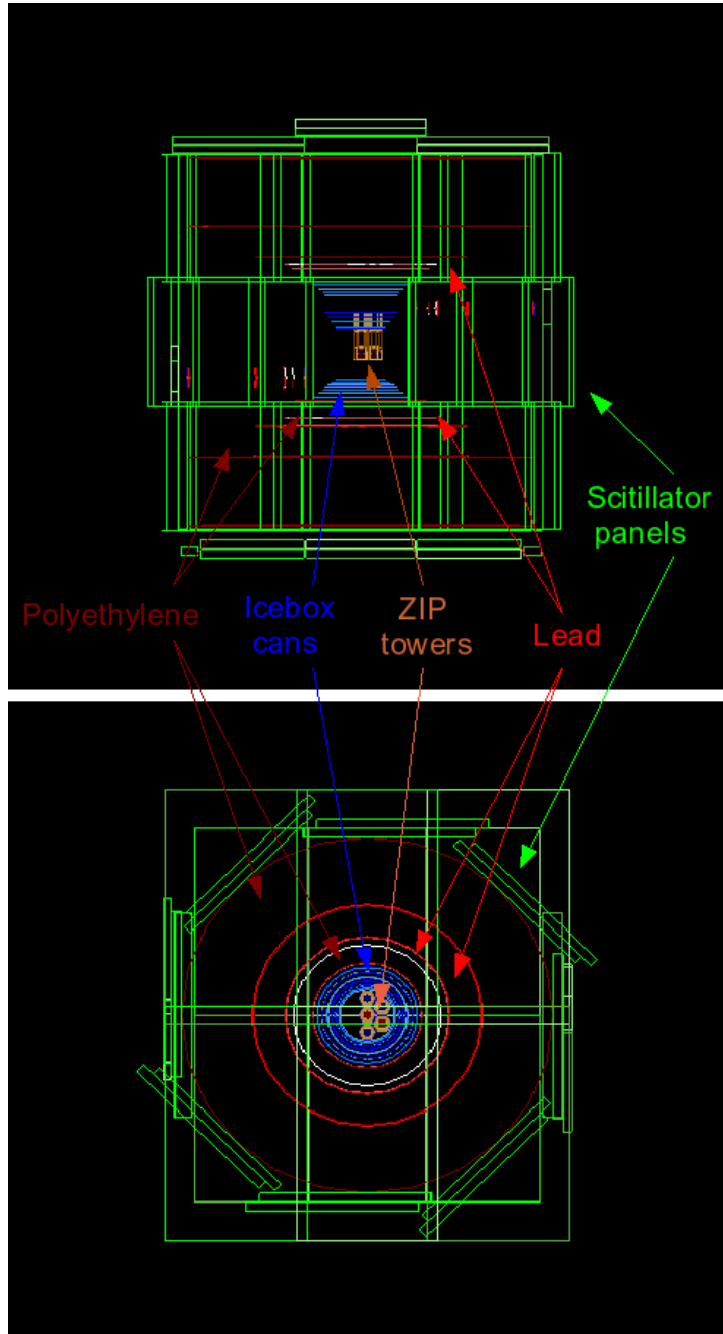


Figure 3.1: CDMS assembly in GEANT 4.
Side view and top view of the CDMS assembly as simulated in GEANT4. Shown are the contours of the shielding, the copper cans of the icebox and the five copper tower guts containing thirty ZIP detectors.

3.2 Monoenergetic neutron simulation on Si and Ge

In order to become introduced to GEANT4 a simple geometry simulation was written, consisting of a 4x4x4 mm Ge- and a Si-block of the same size. The arrangement is shown in Figure 3.2. A beam of monoenergetic neutrons (green) were shot perpendicular to the Ge / Si -crystals surface. The neutrons could pass the detector without being influenced by the crystal or undergo an elastic alternatively inelastic interaction in the crystal, resulting in a changing of their trace direction. In order to calculate the strongly energy-dependent neutron cross sections in Ge and Si, the number of elastic and inelastic scattered neutrons was recorded. $1 \cdot 10^6$ neutrons at fifteen different beam energies respectively were simulated and shot on both, the Ge and Si block. A similar work was done previously by S. Kamat. This calculated cross sections were compared with those from the JENDL-library [29]. The procedure was performed for two different GEANT4 physics libraries, with the objective to investigate the possible influence of different GEANT4 physics lists.

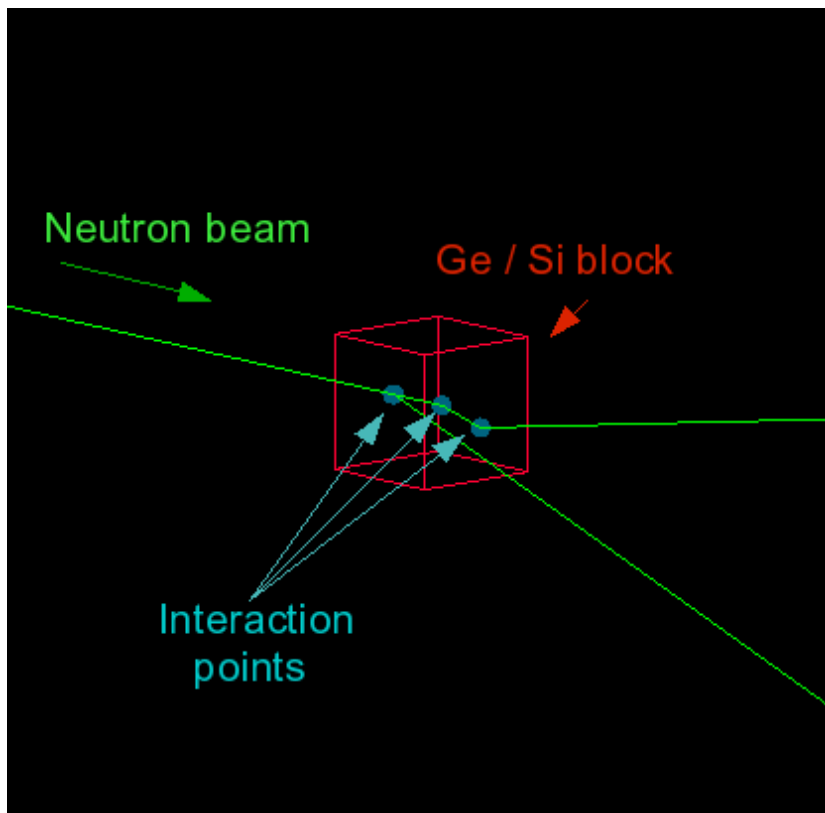


Figure 3.2: GEANT4 neutron cross sections.
Scheme of the GEANT4 simulation used for determining neutron cross sections
in Ge and Si. The target block is 4x4x4 mm in size.

3.3 Calculating the neutron cross sections

The total cross section σ_{tot} is the sum of its elastic σ_{el} and inelastic σ_{inel} component

$$\sigma_{tot} = \sigma_{el} + \sigma_{inel}. \quad (3.1)$$

The angle independent total cross section can be calculated by the mean interaction length λ_T of neutrons in the target material. The correlation between λ_T , σ_{tot} and the number of thrown particles is given by

$$\sigma_{tot} = \frac{A}{\lambda_T N_A \rho} \quad (3.2)$$

where A is the atomic weight of the target, $N_A = 6.022 \cdot 10^{23} [\text{mol}^{-1}]$ is the Avogadro number and ρ is the target density. In order to calculate λ_T from the number of neutron interactions, one must regard the probability P_i of interaction in the material, defined as

$$P_i = \frac{\sigma_{tot} n F dx}{F} = \sigma_{tot} n dx = \sigma_{tot} \frac{N_A \rho}{A} dx \quad (3.3)$$

where n is the target particle density, dx is the differential target thickness and F is the absorber surface. The decrease dN of neutron beam intensity after passing a distance of dx in the target can hence be described by

$$dN(x) = -P_i N(x) = -N(x) \sigma_{tot} n dx \Rightarrow N(x) = N_0 \exp[-n \sigma x] \quad (3.4)$$

where N_0 is the initial neutron-beam intensity. With equation (3.2) this leads to

$$N(x) = N_0 \exp\left[-\frac{x}{\lambda_T}\right] \quad (3.5)$$

The event number n_{evt} in a target of thickness L is the difference between N_0 and $N(L)$, and thus the correlation between the number of interactions and λ_T and finally σ_{tot} can be expressed by

$$n_{evt} = N_0 (1 - e^{-L/\lambda_T}) = N_0 (1 - \exp\left[-\frac{LN_A \rho \sigma_{tot}}{A}\right]) \quad (3.6)$$

$$\Rightarrow \sigma_{tot} = -\frac{A}{LN_A \rho} \ln\left(1 - \frac{n_{evt}}{N_0}\right) \quad (3.7)$$

$1 \cdot 10^6$ monoenergetic neutrons were thrown on a 4x4x4 mm target material, which was either natural Ge or natural Si. The natural isotopic mixture [31] of both is shown in Table 3.1

The atomic masses of both elements were weighted by

$$A = \frac{\sum_i A_i w_i}{\sum_i w_i} \quad (3.8)$$

Isotope	Atomic mass [$\frac{m_a}{u}$]	natural abundance [atom %]
^{70}Ge	69.92	20.84
^{72}Ge	71.92	27.54
^{73}Ge	72.92	7.73
^{74}Ge	73.92	36.28
^{76}Ge	75.92	7.61
^{28}Si	27.98	92.23
^{29}Si	28.98	4.68
^{30}Si	29.97	3.09

Table 3.1: Isotopic composition of natural Ge and Si

where A_i is the atomic weight for isotope i and w_i its fraction on the total composition. For Germanium ($\rho = 5.323g/cm^3$) an atomic weight of $A_{Ge} = 72.61$ was determined, whereas $A_{Si} = 28.09$ was determined for Si ($\rho = 2.33g/cm^3$).

The simulation output file contained among quantities like energy deposition and recoil interaction-positions, also the total number of scattered neutrons as well as the number of elastic and inelastic neutron interactions. All three cross sections were calculated in the energy-range [0-20MeV] using equation (3.7) with the corresponding total, elastic and inelastic event numbers. Finally a comparison of the obtained cross sections with the values available in the JENDL-library [29] was done .

Statistical errors for very low event numbers ($n_{evt} < 20$) were considered in the context of the **Feldman-Cousins** method [34]. All statistical errors were very small, and are hence not shown in the following graphics. To show the grade of agreement with the JENDL values, χ^2 -tests were performed on all data-sets.

3.4 Testing the LHEP-BIC-HP physics

Figure 3.3 and Figure 3.4 show the cross sections in Germanium and Silicon as they result from the simulations. The LHEP-BIC-HP physics library was used in the GEANT4 code. Obviously, there is a noticeable deviation of the simulated cross sections in the range between 10 MeV and 20 MeV, resulting in very high χ^2 -values. This is not an issue, as the neutrons which constitute the possible background at CDMS have energies lower than 10 MeV. Figure 3.5 and 3.6 show the same results in the energy-range 0 MeV to 10 MeV. The very good agreement with the JENDL-values in this energy-range is expressed in χ^2 -values between 0.001 and ~ 4 .

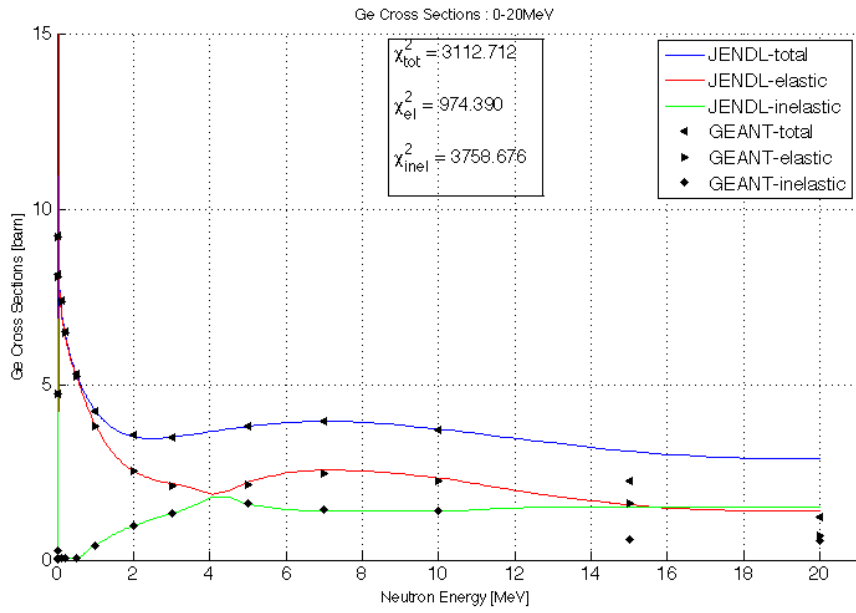


Figure 3.3: Neutron cross sections (0-20 MeV) in Ge, physics library LHEP-BIC-HP.

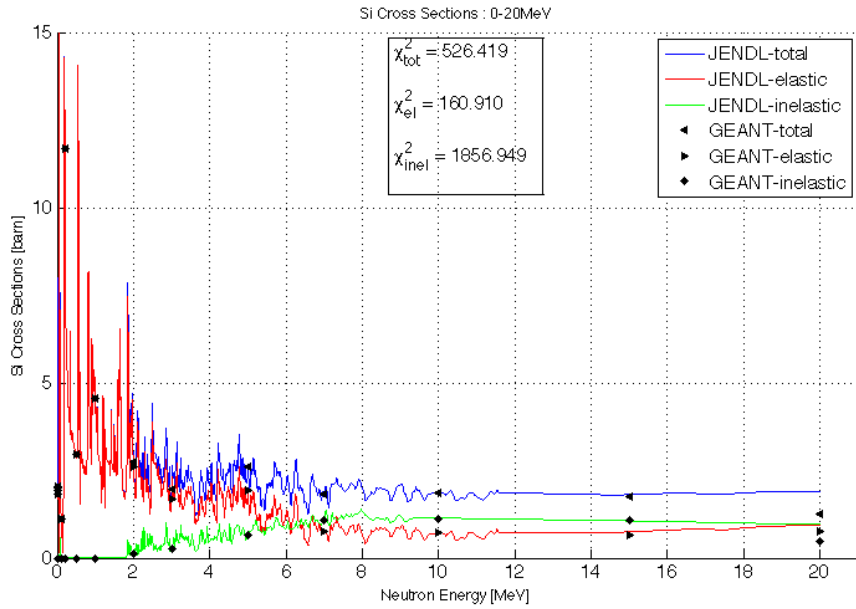


Figure 3.4: Neutron cross sections (0-20 MeV) in Si, physics library LHEP-BIC-HP.

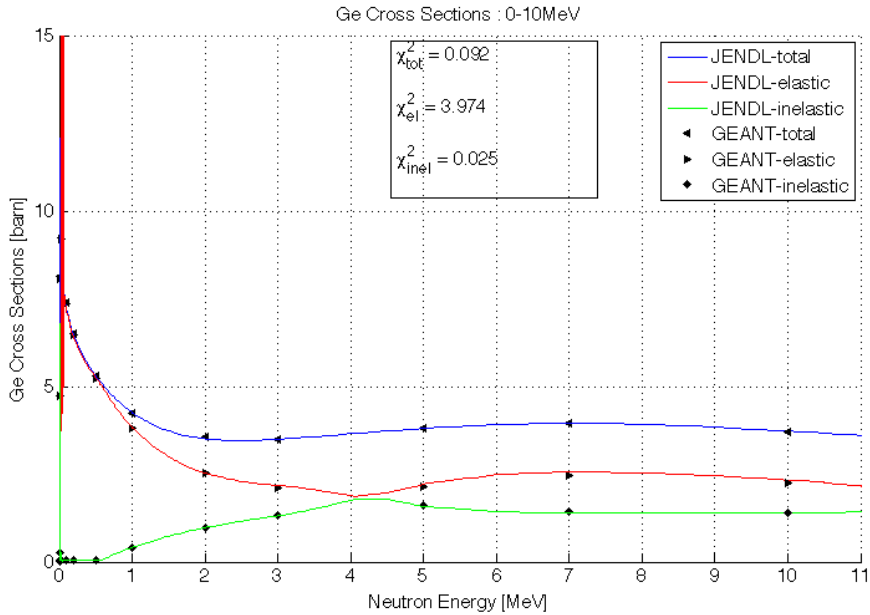


Figure 3.5: Neutron cross sections (0-10 MeV) in **Ge**, physics library LHEP-BIC-HP.

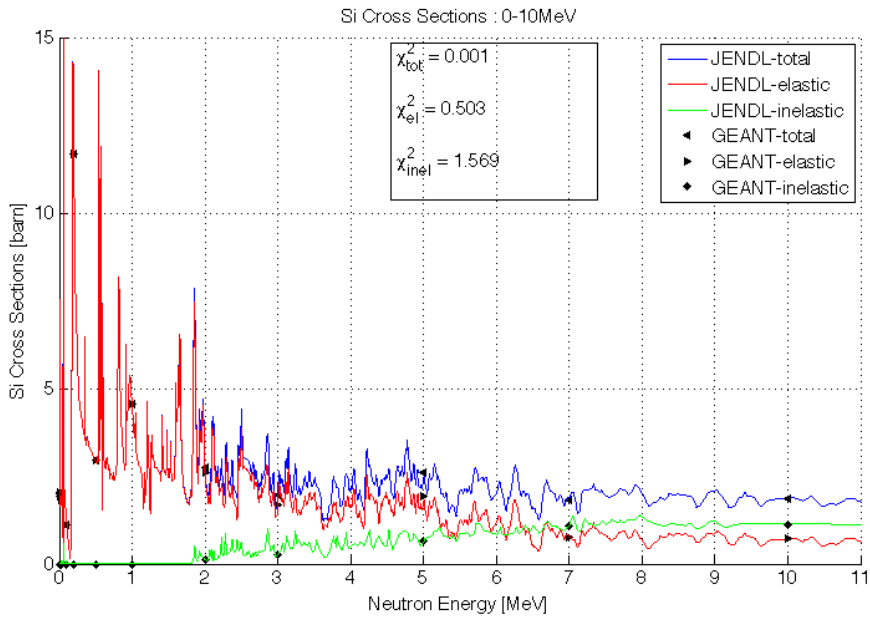


Figure 3.6: Neutron cross sections (0-10 MeV) in **Si**, physics library LHEP-BIC-HP.

Clearly, especially in Ge, neutrons with energies $\lesssim 1\text{MeV}$ tend to interact in an elastic way, because they have not enough energy to excite a nucleus. Recoil signals from such low energy neutrons cause low charge collection in the ZIPS and could be mistaken as WIMPs, assuming their recoil energies are bigger than the detector-threshold energies of about 7keV. Neutrons with higher energies, increasingly undergo inelastic interactions with nuclei, that obtain enough energy to be excited to higher states, resulting in emission of photons, due to de-excitement.

3.5 Testing the LBE physics

The same simulations as described in the previous section were re-run with the LBE physics list, in order to investigate a possible influence of the chosen physics in GEANT4 on the neutron interaction rates. The resulting cross sections in Figure 3.7 and 3.8 exhibit the same behaviour as previously observed using the LHEP-BIC-HP library. χ^2 -values between ~ 700 and ~ 2800 are a consequence of deviations at energies higher than 10 MeV. In contrast, the cross sections for neutrons up to 10 MeV shown in Figure 3.9 and 3.10 show a much better agreement with χ^2 -values between ~ 0.02 and ~ 4 . Table 3.2 shows a summary of the calculated χ^2 -values for both physics libraries in the energy range 0-10 MeV.

LHEP-BIC-HP	Ge	Si
χ^2_{tot}	0.091	0.001
χ^2_{el}	3.908	0.503
χ^2_{inel}	0.025	1.569
LBE	Ge	Si
χ^2_{tot}	1.872	0.021
χ^2_{el}	3.712	1.489
χ^2_{inel}	2.594	2.092

Table 3.2: χ^2 -values on cross sections for the two tested physics libraries LHEP-BIC-HP and LBE in the energy range 0 MeV - 10MeV.

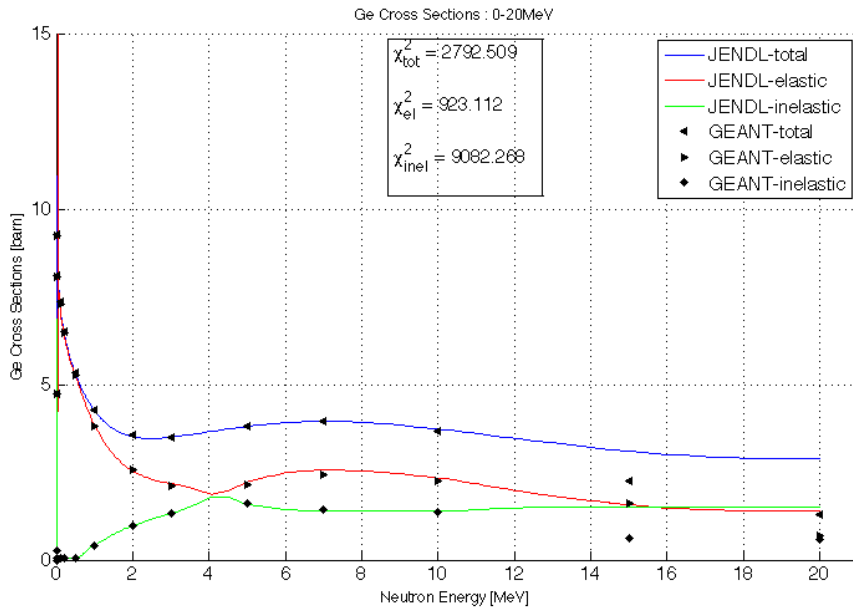


Figure 3.7: Neutron cross sections (0-20 MeV) in **Ge**, physics library LBE.

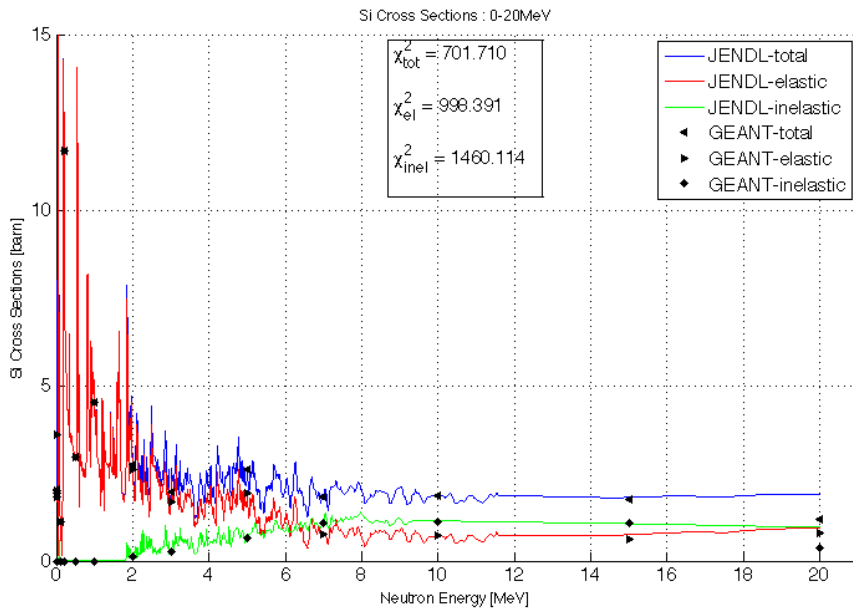


Figure 3.8: Neutron cross sections (0-20 MeV) in **Si**, physics library LBE.

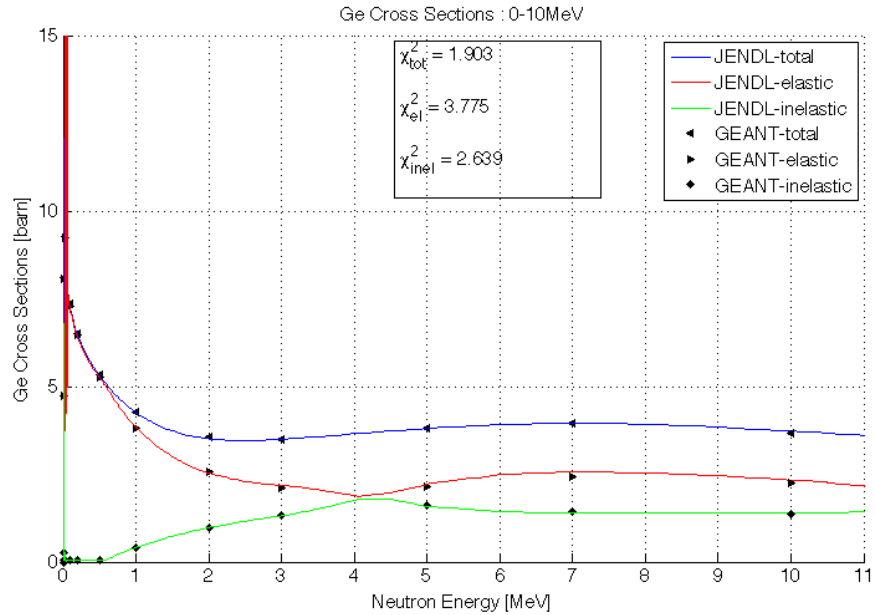


Figure 3.9: Neutron cross sections (0-10 MeV) in Ge, physics library LBE.

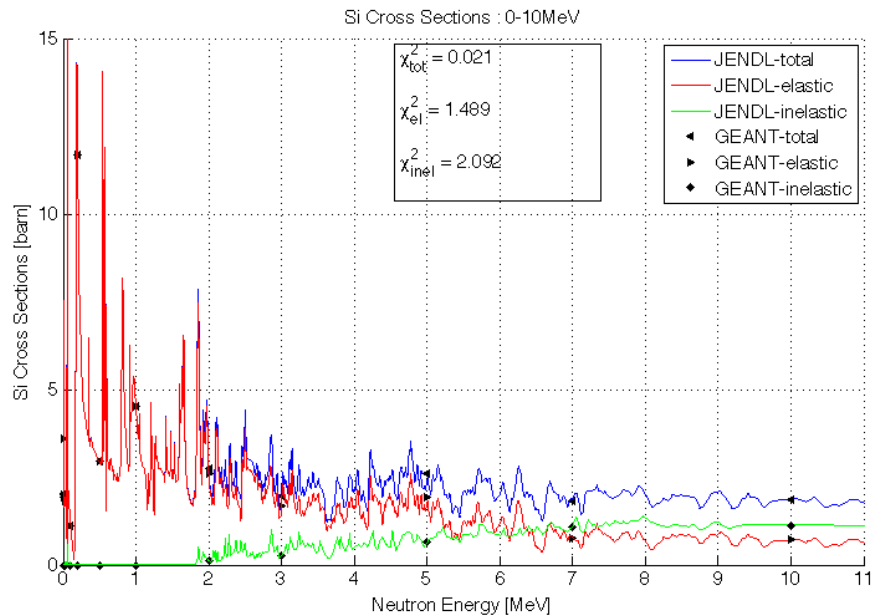


Figure 3.10: Neutron cross sections (0-10 MeV) in Si, physics library LBE.

3.6 Neutron Calibrations with Cf^{252}

In order to characterize the detector response on nuclear and electron recoils, different calibration sources are used. For the electron recoils a ^{123}Ba source, featured by emitting photons, whose spectrum shows four peaks at 276 keV, 303 keV, 356 keV and 384 keV is used. For this calibrations a very good agreement was achieved between data and simulations in the past, although the lines in Si are less sharp than in Ge, due to the domination of Compton scattering in Si.

Nuclear recoils can be characterized using a ^{252}Cf source, emitting besides photons also neutrons at about 1 MeV. To compare the simulated results with the ^{252}Cf datas, first the quantities characterizing the detectors must be derived from the simulation-output files. Those do not contain phonon and ionization energies, which are needed in order to calculate the ionization yields for example. Informations concerning the momentums of the particles, their secondaries, the interaction positions, the deposited energies and the event numbers are available in the simulation output files.

The given total recoil-energy deposited allows to calculate the phonon energy, considering the Neganov-Luke factors $\frac{eV_b}{\epsilon}$ first. This are determined by the detector material and the bias-voltage applied to the crystals. From equation (2.6) and equation (2.7) it follows that

$$E_{ph-sim} = E_{sim} + \frac{eV_b}{\epsilon} E_Q = E_{sim}(1 + \frac{eV_b}{\epsilon} y) \quad (3.9)$$

where E_{ph-sim} is the total phonon energy, which can be calculated via $E_{sim} (\equiv E_R)$, the total event-energy deposited in an simulated interaction. Accordingly, the ionization energy E_{Q-sim} can be calculated by

$$E_{Q-sim} = y \cdot E_{sim} \quad (3.10)$$

Hence using the experimentally determined ionization yields obtained by calibration-runs, it is possible to extract the simulated phonon- and ionization-energies from the simulated recoil energies. Figure 3.11 shows a typical neutron-yield plot as obtained by calibration runs. Obviously, as a result of energy resolution as well as phonon- and charge-channel resolutions, the events are not located at a sharp line defined by the ionization yield, but disperse around their ideal location.

Most of the recoil-events are located within a band, which can be calculated by separating the whole energy range into energy bins and fitting Gaussian to the y-distributions in each of this energy-bin. The functional form for the bands-upper and the lower limit can be described by

$$y_{up} = \mu + \sigma \cdot \frac{c \cdot a \cdot E_R^b + d}{E_R} \quad (3.11)$$

and

$$y_{low} = \mu - \sigma \cdot \frac{c \cdot a \cdot E_R^b + d}{E_R} \quad (3.12)$$

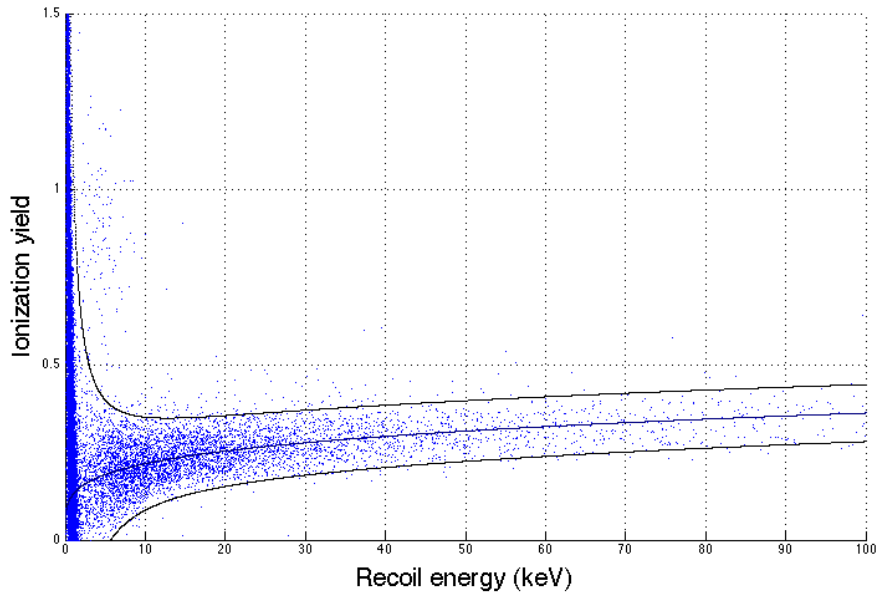


Figure 3.11: ^{252}Cf calibration yield-plot.

Typical neutron calibration yield plot. Most of the events above the threshold energy of 7 keV occur in a band at ionization yields of around 0.3. The black curves show the band fits, the blue one shows the mean value of both, corresponding to the effective ionization yield y_{eff} .

where E_R is the recoil energy, E_Q the ionization energy, σ is the standard deviation, c, a, d are constants derived from the Gaussian and μ is the mean function of y_{up} and y_{low} , described by

$$\mu = \frac{a \cdot E_R^b}{E_R} := y_{eff} \quad (3.13)$$

For the purpose of reproducing the y-plots by a simulation one must use the mean yield obtained by calibration runs instead of y in equations (3.9) and (3.10) and add some randomly distributed noise to y_{eff} in order to disperse the events. The standard deviation of the noise distribution is based on the energy resolution of the phonon and charge channels, determined individually for each detector. This works for elastic interactions very well, but inelastic events which cause higher charge collection would also be forced into the nuclear recoil band this way. To avoid this and to make sure that these events obtain the right ionization yield, a separation into a nuclear recoil part and an electron recoil part was done for inelastic events.

$$E_{sim-in} = E_{nr} + E_{er} \quad (3.14)$$

where E_{nr} and E_{er} are the energies deposited in a nuclear recoil and an electron-

recoil respectively. The yield y_{inel} for such inelastic event can be calculated by weighting over the nuclear- and electron-recoil energy-fractions.

$$y_{inel} = y_{nr} \frac{E_{nr}}{E_{sim}} + y_{er} \frac{E_{er}}{E_{sim}} \quad (3.15)$$

3.7 ^{252}Cf Spectrum

^{252}Cf is probably the most conventional and a very compact neutron source among other radio-isotopic (α, n) sources like $^{239}Pu/Be$ or some photo-neutron sources. ^{252}Cf is a heavy nuclide, emitting neutrons (half-life is about 2.65 years) by spontaneous fission due to the excitation of its fragments. The energy of this neutrons is depending on the velocity distributions of the fission fragments, their masses, number of other accompanying emitted particles and a lot of other factors. The fission particles consist of neutrons, photons, and of $\sim 1\%$ delayed neutrons due to β -decays. Hence the excitation energy E must be at least

$$E = \nu(B_n + E_n) + E_\gamma \quad (3.16)$$

where B_n is the neutron binding energy, E_n is the neutron kinetic energy, E_γ is the emitted photon energy and ν is the neutron multiplicity defined as the sum of number fission neutrons ν_f and the number of delayed neutrons ν_d .

$$\nu = \nu_f + \nu_d \quad (3.17)$$

The multiplicity is not a constant and has a probability distribution $P(\nu)$ corresponding to [28]

$$P(\nu) = \frac{1}{\sqrt{2\pi\sigma^2}} \exp\left[-\frac{(\nu - \bar{\nu})^2}{2\sigma^2}\right] \quad (3.18)$$

where $\bar{\nu}$ is the mean multiplicity

$$\bar{\nu} = \sum \nu P(\nu) \quad (3.19)$$

and σ is the square deviation of ν . Table 3.3 shows some values for neutron emission probabilities for different multiplicities of ^{252}Cf .

The average multiplicity of ^{252}Cf is 3.757 neutrons per fission and the standard deviation of its probability distribution is $\sigma_\nu^2 = 1.59$. Around $2.3 \cdot 10^6$ n/s are produced by one microgram of ^{252}Cf . During every fission process around 9.7 photons are emitted additionally.

Because the theoretical handling of the fission process is complicated, the energy spectrum of the ^{252}Cf fission neutrons was found semi-empirical. It can be expressed either by the Watt-distribution or by the Maxwellian distribution.

P(0)	0.00217
P(1)	0.02556
P(2)	0.12541
P(3)	0.27433
P(4)	0.30517
P(5)	0.18523
P(6)	0.06607
P(7)	0.01414
P(8)	0.00186
P(9)	0.00006

Table 3.3: neutron emission probabilities for ^{252}Cf
[28]

Watt Distribution

$$N(E) = \frac{1}{\sqrt{\pi E_f T_W}} \cdot e^{-\frac{E_f}{T_W}} \cdot e^{-\frac{E}{T_W}} \cdot \sinh \frac{2\sqrt{E_f E}}{T_W} \quad (3.20)$$

where $N(E)$ is the probability density, E_f is the mean kinetic energy per nucleon of a fragment and T_W is the fragments temperature.

Maxwellian Distribution

$$N(E) = \frac{2}{\sqrt{\pi T_M^3}} \cdot \sqrt{E} \cdot e^{-\frac{E}{T_M}} \quad (3.21)$$

where $T_M = \frac{2}{3}\bar{E}$ is the effective nuclear temperature, defined by the mean neutron energy \bar{E} . For both distributions the parameters were found to be [28]

- $T_W = 1.175 \pm 0.005$
- $E_f = 0.359 \pm 0.009$
- $T_M = 1.42 \pm 0.01$

3.8 GEANT4 Simulation of a ^{252}Cf source

According to the ^{252}Cf spectrum described in the previous section a datafile containing one line of neutron energy and a second one containing the related probability densities was created in MATLAB and used in the GEANT4 code to simulate ^{252}Cf fission neutrons. The Cf source was placed in a position corresponding to the CDMS-II calibration south-position at (34.9174 m, -9 cm, 21 cm). In order to confirm the correctness of the GEANT4 simulated neutron spectrum of the ^{252}Cf source, the energies of the neutrons thrown by GEANT4 were compared with the normed Maxwell and Watt distributions. Figure 3.14 shows both theoretical distributions and the normed spectra of $1 \cdot 10^7$ neutrons produced by GEANT4. No multiplicity was considered in the simulation, hence a simultaneous emission of neutrons did not take place.

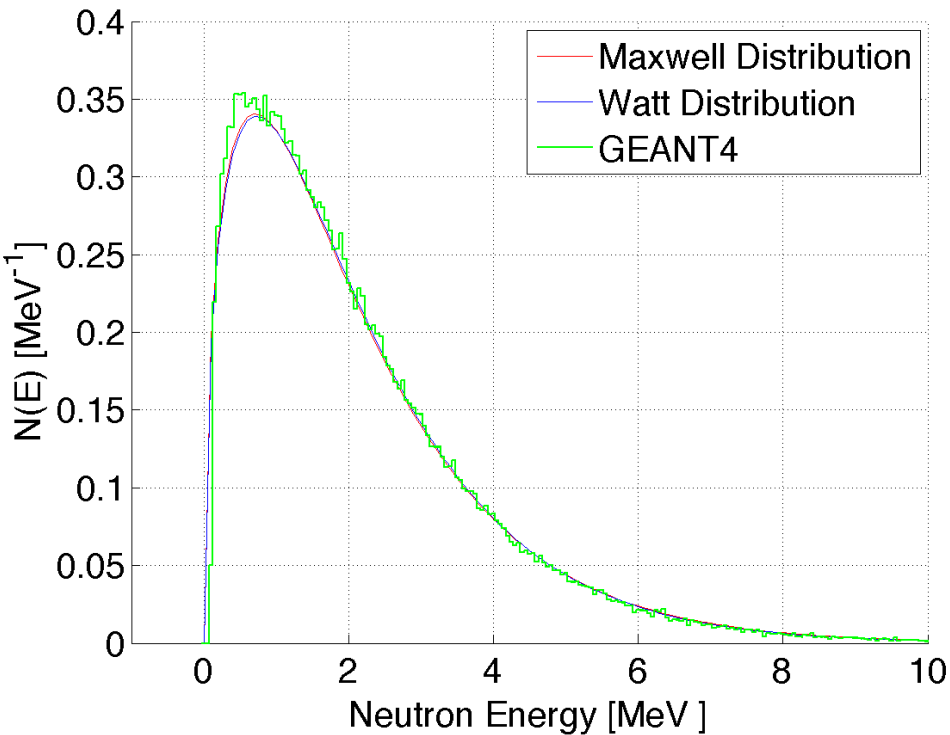


Figure 3.12: ^{252}Cf neutron spectrum.
Comparison of neutron spectra as produced by GEANT4 with the theoretical Watt and Maxwellian distributions.

The small discrepancy in the energy distribution at $\lesssim 1\text{MeV}$, leads to a shift of the mean energy, which was, after weightening determined to be $\bar{E}_{GEANT} = 2.094\text{MeV}$, whereas the mean energy determined by the theoretical energy distribution is

$$\bar{E}_{theory} = 2.13 \pm 0.01 MeV$$

This results in a deviation of $\sim 1.7\%$ between theory and simulation.

3.8.1 Comparison-Monte Carlo/Data

Calibration sources can be placed either at the north side or south side inside the CDMS assembly. The simulation of the ^{252}Cf calibrations, was performed on the 5 tower geometry at the south side location for the Cf-source at (34.9174 cm, -9 cm, 21 cm) relatively to the simulations coordinate system. As calibration runs took place using both, the south and north locations, only datasets obtained by the south calibrations were taken into account, for a comparison between datasets and simulation.

The first CDMS run in the Soudan mine started in 2003. The nuclear recoil calibrations were done using a ^{252}Cf source with an activity of $\sim 5\mu Ci \equiv 185 \cdot 10^3$ Bq. Simulations were compared with data sets from run123, which took place in 2007, and hence a smaller activity A of the Cf-source, calculated by the decay law was taken into account

$$A = -\frac{dN}{dt} = \lambda N_0 e^{-\lambda t} = \frac{\ln 2}{T_{1/2}} N_0 \exp\left[-\frac{t \cdot \ln 2}{T_{1/2}}\right] \quad (3.22)$$

where dN is the number of decayed nuclei in the time dt, N_0 is the initial number of nuclei, λ is the decay constant, defined as

$$\lambda = \frac{\ln 2}{T_{1/2}}, \text{ with the half-life } T_{1/2}, \text{ which is } \sim 2.6 \text{ years for } ^{252}Cf.$$

For a period of four years, an Cf activity of $63.686 \cdot 10^3$ Bq was calculated. In order to finally obtain the number of neutrons emitted by this source, one must take the fission fraction of $\sim 3.1\%$ and the multiplicity of ~ 3.8 into account. Considering both, the Cf-neutron emission rate R during run123 was determined to be

$$R \approx 7600 \frac{n}{s} \quad (3.23)$$

The south calibration data-set used for comparison with the simulations was

- 161109-1430
- 161109-1444
- 170112-1211
- 170307-1033

with a total Cf exposure-time of 1664.2 s ($\sim 27\text{min.}$). This means, that around $13 \cdot 10^6$ neutrons were thrown during this calibration runs, according to the neutron rate in (3.23). During the ^{252}Cf simulation $55 \cdot 10^6$ neutrons were thrown

and hence the resulting spectras had to be rescaled by a factor

$$sc = \frac{n_{cal}}{n_{sim}} \approx 0.236 \quad (3.24)$$

where n_{cal} = number of neutrons thrown during the calibration and n_{sim} = number neutrons thrown in the simulation.

Figure 3.13 shows an example of a yield plot with the gamma and neutron bands for detector 402 obtained by the simulation. The band parameter were taken from run123. The blue points represent multiple scatter events, the green points are single events and the red points are inelastic events, which were calculated by (3.15). The dashed line represents the 7 keV threshold energy for the detectors. As only ^{252}Cf neutrons were simulated, the gamma band contains no electron recoil events caused by photons.

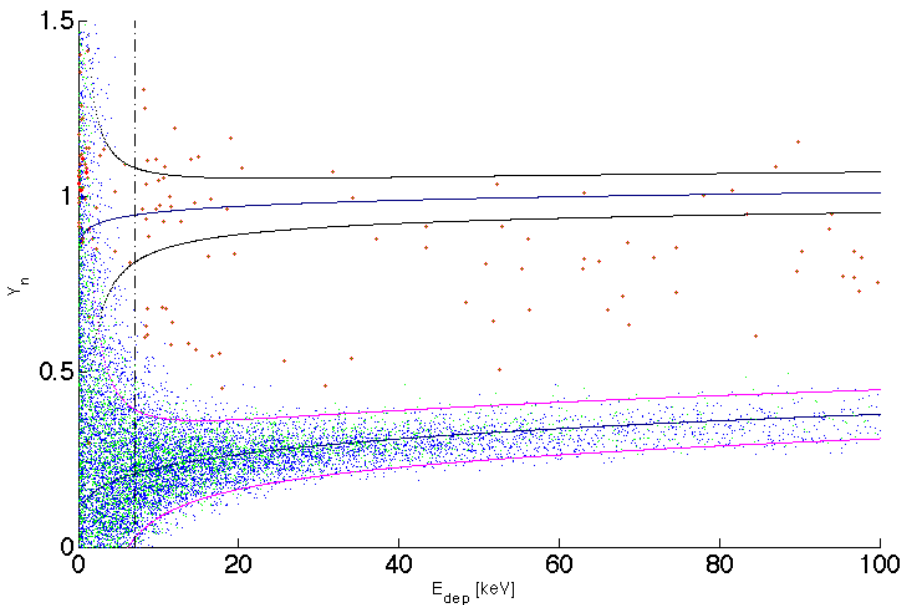


Figure 3.13: Yield plot of a simulated ^{252}Cf neutron source.
Yield plot of simulated ^{252}Cf neutron recoil events, shown for detector 402. The blue points represent nuclear recoil events, the green points represent single events and the red ones are inelastic events. The vertical line is marking the 7 keV threshold energy for the detector.

Because the CDMS apparatus can not distinguish between multiple neutron scatters in one single detector and those, who really scatter once in one single detector, a multiple scatter was defined as a particle, which scatters at least one more time in at least one more detector. Inelastic events were defined as events which were accompanied by at least one photon.

The spectra were compared by applying the following cuts to the data and MC:

DATA

- cGoodEv-123 : removes bad data, due to noise glitches in electronics or the phonon and charge signals.
- cNR-123 : All events, whose yields are not inbetween the nuclear recoil band are removed by this cut.
- cSingle-123 : selects events which occur only once in one detector within a time frame of $50 \mu\text{s}$
- 7keV-cut : This cut ignores all events which deposited less than the detector-threshold energy of $\lesssim 7 \text{ keV}$

MonteCarlo

- Nuclear recoil-cut: removes all events which are not inbetween the nuclear recoil band, defined in cNR-123
- Single-cut: considers only nuclear recoil events which occurred in one single detector.
- 7keV-cut: This one is identical to that, applied to the data.

Figure 3.14 shows a comparison of the MC and data spectrum for ^{252}Cf in detector 402. For the MC-data the scale-factor (3.24), the nuclear recoil- and the 7 keV cut were applied. The data include the cGoodEv, cNR- and the 7 keV cuts.

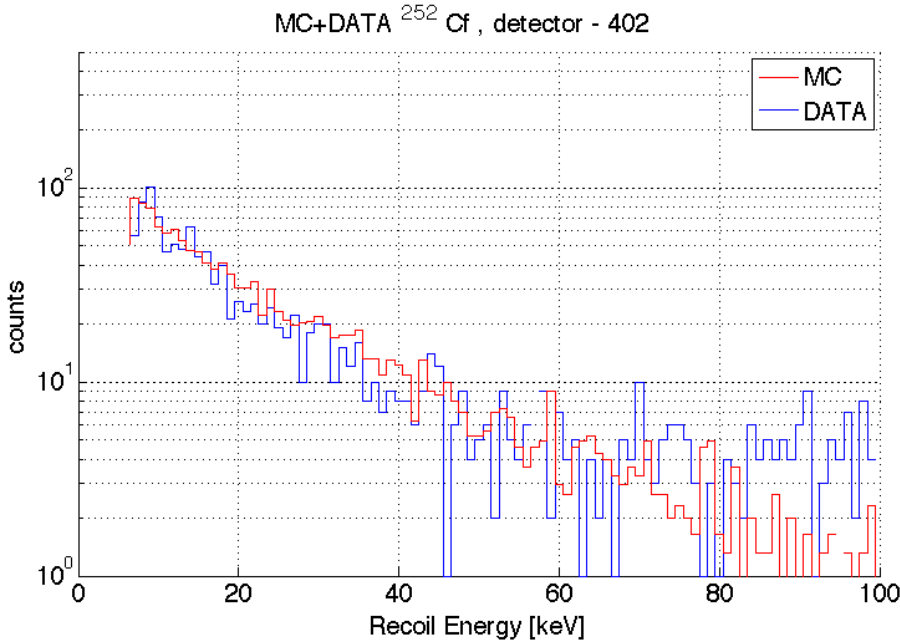


Figure 3.14: ^{252}Cf , MonteCarlo vs. Data spectrum.
MC and data comparison of a ^{252}Cf neutron spectrum in detector 402. The nuclear recoil cut, the 7 keV cut and the cGoodEv cut were applied.

Table 3.4 shows the number of nuclear recoil events for the data, and the number of nuclear recoils obtained by the simulation. The scalefactor (3.24) was applied to the MC data before. The remaining discrepancy between data and MC is represented by a second correction factor fnr

$$fnr = \frac{nr_d}{nr_s \cdot sc} \quad (3.25)$$

where nr_d is the number of nuclear recoils in the data and nr_s is the number of nuclear recoils in the simulation. The factor fnr was individually determined for each detector. Datas for detectors 1,3,12,13,26 are not available due to technical problems at CDMS. The discrepancy between the data and MC seems even bigger for single events. Table 3.5 shows the numbers of single events and their correction factors fsr, defined analogically to fnr. The spectras obtained after rescaling the MC data with fnr are shown in Appendix A. The origin of this discrepancies could not be clarified in this work, hence both correction factors fnr and fsr were applied later to all simulation data.

Detector (*)	Data-nr total	MC-nr-Total	correction factor-fnr
Detector 1	-	-	-
Detector 2	1333	1442.6	0.9241
Detector 3	-	-	-
Detector 4	822	1199	0.6856
Detector 5	833	990.5	0.841
Detector 6	-	-	-
Detector 7	1359	1636.1	0.8306
Detector 8	1252	1420.1	0.8816
Detector 9	784	1324.4	0.592
Detector 10	1123	1122.3	1.0006
Detector 11	831	1003.8	0.8278
Detector 12	-	-	-
Detector 13	-	-	-
Detector 14	731	1111.1	0.6579
Detector 15	735	909.5	0.8081
Detector 16	643	797.6	0.8062
Detector 17	425	822	0.5170
Detector 18	590	628.2	0.9391
Detector 19	949	1301	0.7295
Detector 20	867	1130	0.7673
Detector 21	796	1187.7	0.6702
Detector 22	775	944.6	0.8205
Detector 23	586	904.7	0.6477
Detector 24	467	723.7	0.6453
Detector 25	1040	1339.8	0.7763
Detector 26	-	-	-
Detector 27	961	1000.5	0.9605
Detector 28	730	952.4	0.7665
Detector 29	768	834	0.9208
Detector 30	499	803.8	0.6208

Table 3.4: Individual scale factors fnr for nuclear recoil events.

(*) For alternative detector designation see Table A.1 in Appendix A.

Detector	Data-single	MC-single	correction factor-fsr
Detector 1	-	-	-
Detector 2	402	648.292	0.6201
Detector 3	-	-	-
Detector 4	143	442.854	0.3229
Detector 5	155	426.806	0.3632
Detector 6	-	-	-
Detector 7	332	936.802	0.3544
Detector 8	255	606.284	0.4206
Detector 9	130	566.99	0.2293
Detector 10	198	419	0.4715
Detector 11	164	437.072	0.3752
Detector 12	-	-	-
Detector 13	-	-	-
Detector 14	154	549.408	0.2803
Detector 15	161	377.482	0.4265
Detector 16	74	330.99	0.2236
Detector 17	87	332.406	0.2617
Detector 18	150	330.164	0.4543
Detector 19	278	778.918	0.3569
Detector 20	246	551.768	0.4458
Detector 21	177	477.192	0.3709
Detector 22	165	383.382	0.4304
Detector 23	119	385.978	0.3083
Detector 24	93	363.558	0.2558
Detector 25	292	774.788	0.3769
Detector 26	-	-	-
Detector 27	162	360.726	0.4491
Detector 28	117	351.876	0.3325
Detector 29	127	321.432	0.3951
Detector 30	94	363.912	0.2583

Table 3.5: Individual scale factors fsr for single events

Chapter 4

Simulation of the (α, n) -induced neutron backgrounds

4.1 SOURCES4mv

As described in Chapter 2, neutrons from (α, n) -reactions and spontaneous fission can occur in the detector materials and its environment resulting in a possibly significant neutron background, which can not be reduced by shielding. In order to estimate this background, SOURCES4mv was used, which is a software calculating the production rates and spectra of (α, n) , spontaneous fission and delayed neutrons. This software contain the corresponding libraries with cross sections, branching ratios, half-lives and spectra-parameter for the most isotopes which can be involved in such reactions. The spectra are calculated corresponding to a script which includes the fractional composition of the target material, the fractions of the different isotopes, the concentrations of the α -emitting components and their decay-chain products. Geometries can not be implemented, hence for thin materials only upper limits can be specified, as SOURCES4mv works with stopping cross sections in a default material volume of 1 cm^3 .

4.2 (α, n) -reactions in the CDMS assembly

Although activity-screenings on the most materials used in CDMS were performed, unfortunately no consequent documentation of the U and Th contaminations is available and hence the contaminations were assumed mainly relying on some collaboration-internal notes and files (see [30]). Table 4.1 shows the Uranium and Thorium concentrations in the different CDMS-components used for calculating the (α, n) and spontaneous fission spectra. Three groups of three different contaminations were specified:

- the Copper cans of the icebox
- the Copper towerguts (and other directly related Cu-parts) containing the detectors

- the polyethylene shields around the icebox

Component group	U[ppb]	Th[ppb]
Cu cans	0.0797	0.2989
Cu towerguts	0.2	1
inner polyshield	0.2	0.2

Table 4.1: Concentrations of U and Th in the CDMS components

Cu-Cans (V [cm ³])	Cu-Towerguts (V [cm ³])	Polyshield (V [cm ³])
OVC-can (3938.674)	upper tower (224.215)	innerpoly (81227.678)
OVC-cap (3911.367)	upper tower base (26.121)	innerpoly cap (20391.492)
OVC-base (3911.367)	connectortube (15.695)	innerpoly base (27188.657)
Liquid N-can (3146.6079)	connectortube-basering(5.717)	
Liquid N-cap (632.113)	detectorhousing-cap(7.959)	
Liquid N-base (632.113)	detectorhousing (43.049)	
IVC-can (2606.725)	detectorhousing-base (8.744)	
IVC-cap (2489.72)	12 x side-coaxes (7.244)	
IVC-base (2489.72)		
Still can (1652.532)		
Still-cap (143.31)		
Still-base (401.976)		
Cold-can (1317.72)		
Cold-cap (91.467)		
Cold-base (315.324)		
Base-can (949.349)		
Base-cap (129.459)		
Base-base (228.972)		

Table 4.2: The CDMS components and their voluminas which were considered as (α, n) sources.

Table 4.2 show all components which were used as (α, n) -sources with neutron-energy spectra corresponding to those obtained by SOURCES4mv. The U and Th atom densities $\rho_{U/Th}$ in Cu and Polyethylene were calculated by

$$\rho_{U/Th} = \frac{\rho_{Cu/P} \cdot c_{U/Th} \cdot 10^{-9}}{m_{U/Th}} \cdot N_A \quad (4.1)$$

where $\rho_{Cu/P}$ are the Cu and Polyethylene densities, $c_{U/Th}$ the concentrations (in [ppb]) of U and Th, $m_{U/Th}$ the mol masses of U and Th and $N_A =$

$6.022 \cdot 10^{23} mol^{-1}$ the Avogadro constant.

Using

- $\rho_{Cu} = 8.92 g/cm^3$
- $\rho_P = 0.935 g/cm^3$
- $m_U = 238.0289 g/mol$
- $m_{Th} = 232 g/mol$

from [31], or

- $1Bq^{238}U \equiv 81 ppb U$
- $1Bq^{232}Th \equiv 246 ppb Th$ from [32]

one obtains the following atom densities of U and Th in the cans, the towerguts and the inner poly listed in Table 4.3.

$\rho [atoms/cm^3]$	Cans	Towerguts	Inner Poly
U	$1.787 \cdot 10^{12}$	$4.494 \cdot 10^{12}$	$4.731 \cdot 10^{11}$
Th	$6.925 \cdot 10^{12}$	$2.317 \cdot 10^{13}$	$4.854 \cdot 10^{11}$

Table 4.3: atom densities of U and Th in the CDMS components

This densities were used in SOURCES4mv. Additionally decay-chains for ^{238}U , ^{235}U and ^{232}Th were added to the SOURCES-script. The ^{235}U chain was added, because it appears in natural Uranium with a fraction of $\sim 0.7\%$. The chainlinks involved in α -decays are listed below.

- $^{238}U \rightarrow^{234} U \rightarrow^{230} Th \rightarrow^{226} Ra \rightarrow^{222} Rn \rightarrow^{218} Po \rightarrow^{210} Po \rightarrow^{206} Pb$
- $^{235}U \rightarrow^{231} Pa \rightarrow^{227} Ac \rightarrow^{227} Th \rightarrow^{223} Ra \rightarrow^{219} Rn \rightarrow^{215} Po \rightarrow^{211} Bi \rightarrow^{207} Pb$
- $^{232}Th \rightarrow^{228} Th \rightarrow^{224} Ra \rightarrow^{220} Rn \rightarrow^{216} Po \rightarrow^{212} Bi \rightarrow^{212} Po \rightarrow^{208} Pb$

Isotope	^{63}Cu	^{65}Cu	^{12}C	^{13}C
Natural abundance [%]	69.17	30.83	98.9	1.1

Table 4.4: Natural abundance of Cu and C isotopes [31]

Targetmaterials were added considering their natural abundance of isotopes. Polyeyhylene is a polymer consisting of C_2H_4 -chains. Hydrogen can not play any

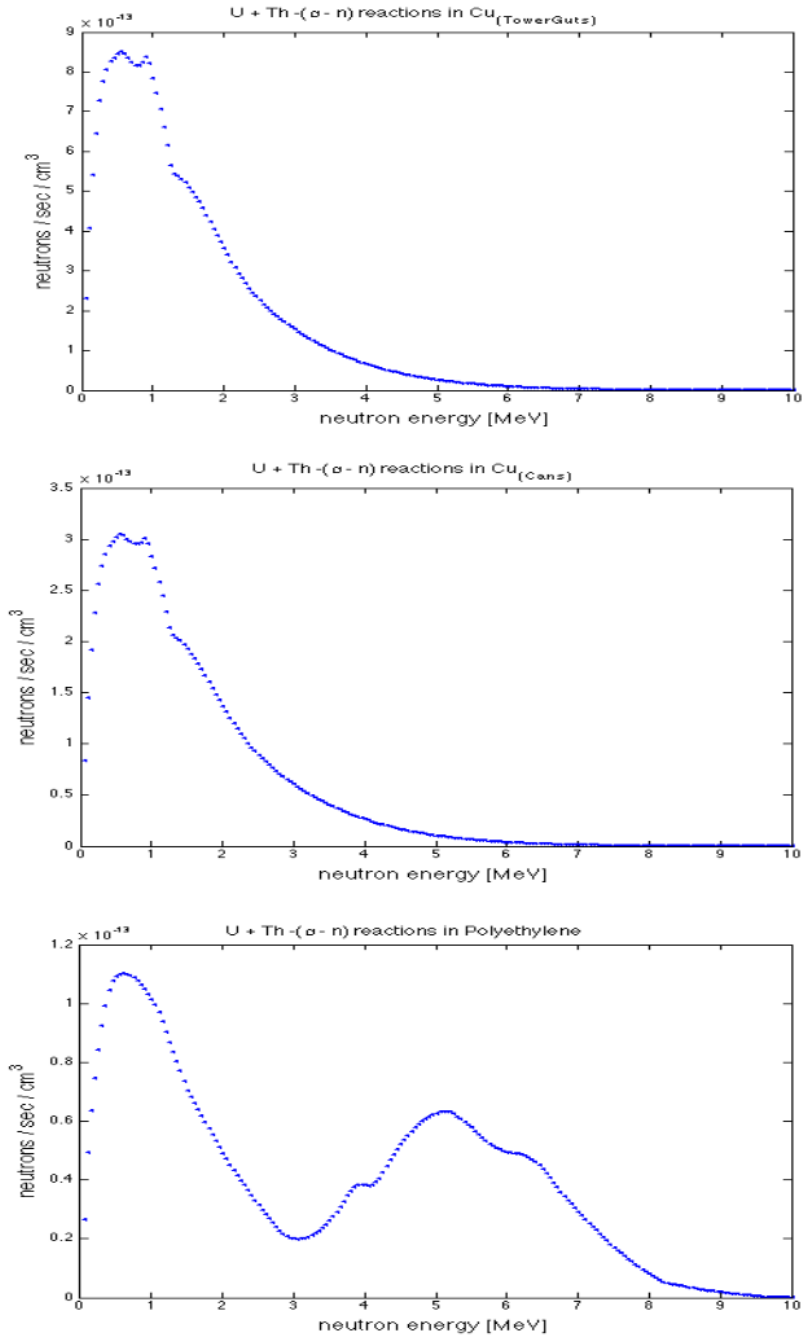


Figure 4.1: Neutron spectras from (α, n) reactions.
 Total neutron spectras from (α, n) -reactions in the towerguts, the cans and in the
 inner poly as calculated by SOURCES4mv.

role in (α, n) -reactions, hence only the carbon was added to the script with a fraction of 33 %. The natural abundances of Copper and Carbon used in SOURCES are listed in Table 4.4 The neutron spectras from (α, n) -reactions were calculated for U and Th separately. Figure 4.1 show the resulting total spectras for the cans, the towerguts and the inner poly. The separated spectras for U and Th are shown in Appendix B.

Resulting total neutron rates per cm^3 from the above spectras are:

- **Cu-cans:** $1.2322 \cdot 10^{-11} n/s/cm^3$
- **Cu-towerguts:** $3.3117 \cdot 10^{-11} n/s/cm^3$
- **Poly:** $7.94 \cdot 10^{-12} n/s/cm^3$

4.3 (α, n) -reactions in the Greenstone rock

Another potential neutron source, although not so closely located to the detectors is the rock of the mine. In this section the neutron spectras from (α, n) reactions are determined in the same way as the spectras for the Copper and the Polyethylene in the previous section. Although the chemical composition of the mine-rock in Soudan wasn't explicitly determined, there exist publications, with composition analyses of the rock from the region. In this section, a chemical composition of the rock published in [33] is taken as target-material for (α, n) -reactions in order to estimate the neutron rates from the cavern. The mentioned rock from the region near Soudan is called "Green Stone" and its chemical composition is shown in Table 4.5. The density of the rock is

$$\bullet \rho_{rock} \sim 2.75 - 2.95 g/cm^3$$

as reported in [33]. In this work a mean value of $\rho_{rock} \sim 2.85 g/cm^3$ was chosen. The Green Stones natural radioactivity background is composed of ^{238}U , ^{232}Th and ^{40}K decay chains. Concentrations of radioactive isotopes in the rock of the Soudan mine were measured at different places, and a mean value of them was taken for further analysis of the (α, n) background. The average concentrations of U and Th in the rock are [33] :

- $^{238}U : 0.17 ppm$
- $^{232}Th : 0.89 ppm$

In order to define the rock composition in SOURCES4mv, Table 4.5 was used to calculate the fraction of the rocks elemental composition first, followed by considering the natural abundancies of each isotope (see Table B.1 Appendix B). Some

Molecule	%
SiO_2	50.6
TiO_2	1.1
Al_2O_3	15.0
Fe_2O_3	2.6
FeO	8.6
MnO	0.2
MgO	6.5
CaO	9.0
Na_2O	2.5
K_2O	0.4
H_2O	2.7
CO_2	0.3
P_2O_5	0.1
other	0.4

Table 4.5: Composition of the Green Stone rock.

El.	O	Si	Ti	Al	Fe	Mn	Mg	Ca	Na	K	H	C	P
Ab. [%]	59.31	16.87	0.36	6	5.34	0.1	3.25	4.5	1.67	0.26	1.8	0.1	0.029

Table 4.6: Abundance of the elements in the Green Stone rock

of the isotopes like ^{16}O , ^{28}Si , ^{40}Ca , ^{12}C do not undergo (α, n) -reactions, because when hit by an α -particle they would form a stable element. This isotopes were not included to the SOURCES libraries. The resulting total spectrum of (α, n) -reactions inside the rock is shown in Figure 4.2. The neutron spectras resulting only from the U-component and the Th-component in the rock are shown in Appendix B. The calculated total neutron rate for the Green Stone rock in Soudan is according to the spectra in Figure 4.2:

- **Green Stone** rock : $3.7368 \cdot 10^{-9} n/s/cm^3$

with atomdensites of $1.226 \cdot 10^9 atoms/cm^3$ for U and $6.584 \cdot 10^9 atoms/cm^3$ for Th.

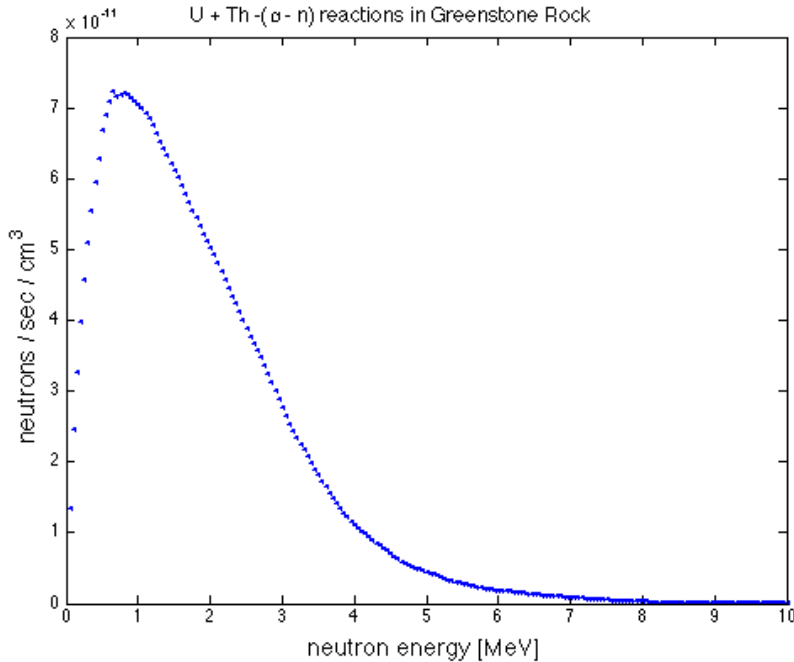


Figure 4.2: (α, n) reactions in the Green Stone rock.
Neutron spectrum resulting from (α, n) -reactions in the Green Stone rock as calculated by SOURCES4mv.

4.4 (α, n) -reactions in Air

An interesting question is that of how many α particles can leave the rock and induce neutrons through (α, n) -reactions with the air atoms of the Soudan cavern. Commonly heavy, charged particles like α 's have very small ranges in matter. This can be some μm in solids. In order to make a more precisely conclusion on α particle ranges in the Soudan rock, and hence on how many of them could undergo interactions with air, the **Bragg-Kleemann** rule was used to calculate the ranges in the Green Stone rock. Furthermore a Geant4 simulation was performed to cross check this result. The Bragg-Kleeman rule is a semi-empirical expression, which allows to approximate ranges of charged particles in material A, assumed that the ranges in material B are known [35].

$$\frac{R_i}{R_0} \cong \frac{\rho_0 \sqrt{A_i}}{\rho_i \sqrt{A_0}} \quad (4.2)$$

where $\rho_{0/i}$ are the densities of material 0 respectively i and $A_{0/i}$ are their atomic weights. For air this results in

$$R_i = 2.2762 \cdot 10^{-4} g/cm^3 \cdot \sqrt{\frac{A_i}{\rho_i R_a}} \quad (4.3)$$

where R_a is the particle range in air. The range in air at $15^\circ C$ and 1atm, however, can be in addition estimated by [36]

$$R_a[\text{cm}] = \begin{cases} 0.56 \cdot E_\alpha & \text{for } E_\alpha < 4 \text{ MeV} \\ 1.24 \cdot E_\alpha - 2.62 & \text{for } E_\alpha \leq 8 \text{ MeV} \end{cases} \quad (4.4)$$

The average α -energies emitted by U and Th are [37]

$$\bar{E}_U \approx 4.7 \text{ MeV} \quad (4.5)$$

$$\bar{E}_{Th} \approx 4 \text{ MeV} \quad (4.6)$$

hence the ranges of U- α 's and Th- α 's in air are

$$R_a \approx \begin{cases} 3.2 \text{ cm} & \text{for } U - \alpha' \text{'s} \\ 2.61 \text{ cm} & \text{for } Th - \alpha' \text{'s} \end{cases} \quad (4.7)$$

The α -ranges in compounds can be calculated by [35]

$$R_c = \frac{M_c}{\sum_i n_i \frac{A_i}{R_i}} \quad (4.8)$$

where M_c is the molecular weight of the compound and n_i the number of atoms of element i.

In principle one could determine the R_i 's in equation (4.8) using equation (4.3) and obtain the α ranges for the Soudan rock this way. In the case of the rock, this wouldn't be really reliable, as all molecules in the rock contain oxygen in a binded form, whose density is an unknown parameter. Instead equation (4.3) was applied to the molecules of the Green Stone rock and their effective molecule-atomic weights A_m , obtaining the α -ranges R_m in the molecules. The ranges R_m obtained in this way were then used together with A_m in equation (4.8) to calculate the ranges in the Green Stone rock composition.

Table 4.7 shows the calculated ranges of α -particles emitted by Uranium for the molecules present in the rock, their densities, and four additional range values for molecules, which could be found in the ASTAR [38] database.

The same procedure was repeated for α -particles emitted by Th. The results can be seen in Table 4.8. The ranges R_c for the whole Grenstone composition obtained with the R_m 's from both Tables 4.7, 4.8 and equation (4.8) are

$$R_c(\alpha_U) \approx 18.97 \mu\text{m} \quad (4.9)$$

for U- α 's of about 4.7MeV, and

$$R_c(\alpha_{Th}) \approx 15.47 \mu\text{m} \quad (4.10)$$

for Th- α 's of about 4MeV.

Molecule	$\rho_m[g/cm^3]$	ASTAR- $R_m[cm]$	$R_m[cm]$
SiO_2	2.32	$1.967 \cdot 10^{-3}$	$2.434 \cdot 10^{-3}$
TiO_2	4.2		$1.55 \cdot 10^{-3}$
Al_2O_3	3.97	$1.179 \cdot 10^{-3}$	$1.853 \cdot 10^{-3}$
Fe_2O_3	5.24		$1.757 \cdot 10^{-3}$
FeO	5.7		$1.083 \cdot 10^{-3}$
MnO	5.45		$1.126 \cdot 10^{-3}$
MgO	3.58		$1.292 \cdot 10^{-3}$
CaO	3.3		$1.653 \cdot 10^{-3}$
Na_2O	2.27		$2.523 \cdot 10^{-3}$
K_2O	2.35		$3.008 \cdot 10^{-3}$
H_2O	1	$3.21 \cdot 10^{-3}$	$3.091 \cdot 10^{-3}$
CO_2	$1.842 \cdot 10^{-3}$	2.042	2.623
P_2O_5	2.36		$3.677 \cdot 10^{-3}$

Table 4.7: Calculated U- α ranges R_m

Molecule	$\rho_m[g/cm^3]$	ASTAR- $R_m[cm]$	$R_m[cm]$
SiO_2	2.32	$1.674 \cdot 10^{-3}$	$1.985 \cdot 10^{-3}$
TiO_2	4.2		$1.264 \cdot 10^{-3}$
Al_2O_3	3.97	$1.002 \cdot 10^{-3}$	$1.511 \cdot 10^{-3}$
Fe_2O_3	5.24		$1.433 \cdot 10^{-3}$
FeO	5.7		$8.834 \cdot 10^{-4}$
MnO	5.45		$9.181 \cdot 10^{-4}$
MgO	3.58		$1.053 \cdot 10^{-3}$
CaO	3.3		$1.3481 \cdot 10^{-3}$
Na_2O	2.27		$2.06 \cdot 10^{-3}$
K_2O	2.35		$2.454 \cdot 10^{-3}$
H_2O	1	$2.711 \cdot 10^{-3}$	$2.522 \cdot 10^{-3}$
CO_2	$1.842 \cdot 10^{-3}$	1.724	2.139
P_2O_5	2.36		$2.999 \cdot 10^{-3}$

Table 4.8: Calculated Th- α ranges R_m

Furthermore, simulations of a typical particle transmission experiment were performed in GEANT4. I_0 α -particles were shot on a target material at energies of 4.7 MeV and 4 MeV corresponding to the average α -energies of U and Th. A block of polyethylene behind the target was registering the number I of transmitted particles. As target material the Green Stone composition was taken, whose thickness was varied between 0 and 10 μm . Figure 4.3 and 4.4 show the behavior of I/I_0 as a function of target thickness. The plots show a typical course

for transmission experiments. The number of transmitted particles stays constant, until the target thickness reaches values close to the mean interaction length of the α particles in the target. The range of the particles can be defined as the target thickness, which causes a decrease of 50% in the particle intensity. As one can see in Figure 4.3 and 4.4 the ranges of 4.7MeV and 4MeV α 's in the cavern rock determined by GEANT4 are about:

$$R_c(\alpha_U) \approx 8.35\mu m \quad (4.11)$$

for U- α 's of 4.7MeV, and

$$R_c(\alpha_{Th}) \approx 6.65\mu m \quad (4.12)$$

for Th- α 's of 4MeV.

Both ranges are about a factor of ~ 2 smaller than those calculated in (4.9) and (4.10). Because an upper limit of the (α, n) neutron background is of interest, a very conservative value of $20\mu m$ for both the (4.7 MeV and 4 MeV) α -ranges in rock was chosen. This $20\mu m$ are regarded as the length which is defining the α emitting volume V' in the rock.

In another conservative assumption, the total number of emitted α 's in this volume, divided by two due to isotropic emission was taken as the number of possible interaction candidates with air. This is illustrated in Figure 4.5. In order to calculate this scenario in SOURCES4mv, a volume of air was regarded which contains the number of U and Th atoms contained in $V'/2$. Thus the densities of U and Th were adequately decreased. This is illustrated in Figure 4.6. The number of U or Th atoms $N'_{U/Th}$, emitting α 's in the rock which can possibly interact with air is

$$N'_{U/Th} = V' \cdot \rho_{U/Th} \cdot 1/2 \quad (4.13)$$

In SOURCES4mv this number is taken as homogeneously contained in the air volume, and thus the new atom densities of U and Th ρ'_U, ρ'_Th are

$$\rho'_{U/Th} = N'_{U/Th}/V \quad (4.14)$$

where V is the volume of the air. The spectrum resulting from this estimation is shown in Figure 4.7.

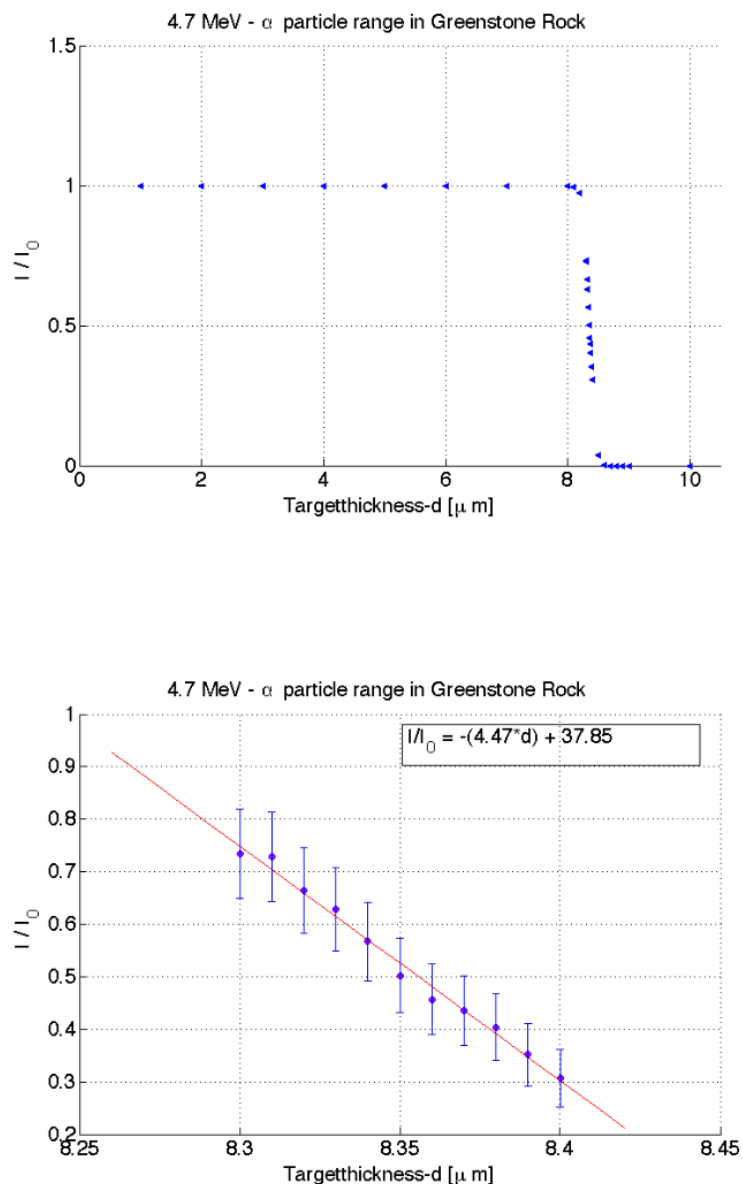


Figure 4.3: Simulated α ranges, α -energy: 4.7 MeV
 Ratio of the initially thrown number of α particles I_0 and the number of transmitted particles I as a function of the Green Stone rock thickness d for α particles emitted by U.

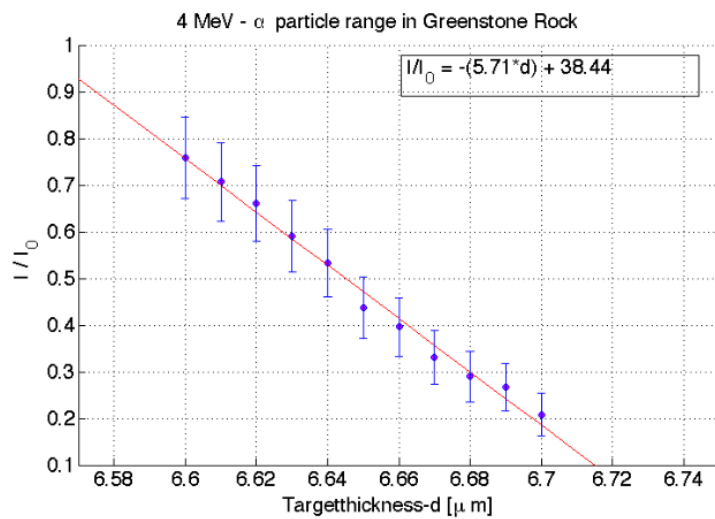
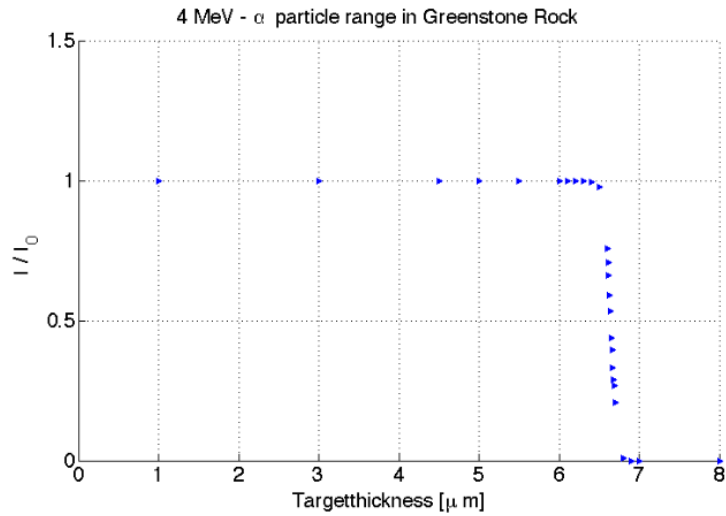


Figure 4.4: Simulated α ranges, α -energy: 4 MeV.

Ratio of the initially thrown number of α particles I_0 and the number of transmitted particles I as a function of the Green Stone rock thickness d for α particles emitted by Th.

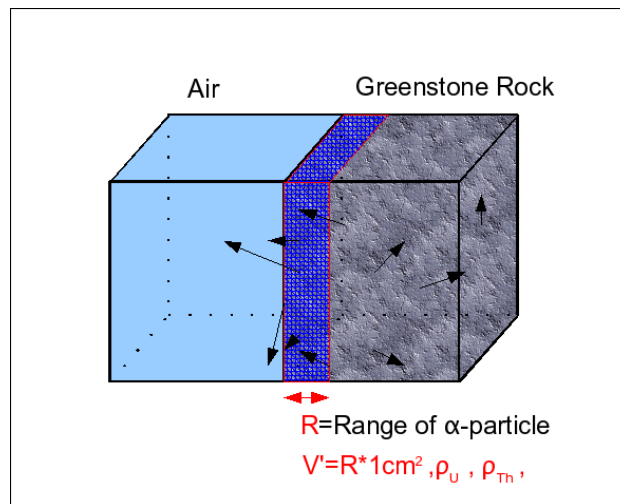


Figure 4.5: Green Stone volume containing possibly escaping α particles. The α particles emitted in the blue patterned volume V' can leave the rock and hence undergo (α, n) -reactions with air. The layer thickness R of V' was conservatively assumed to be $20\mu\text{m}$.

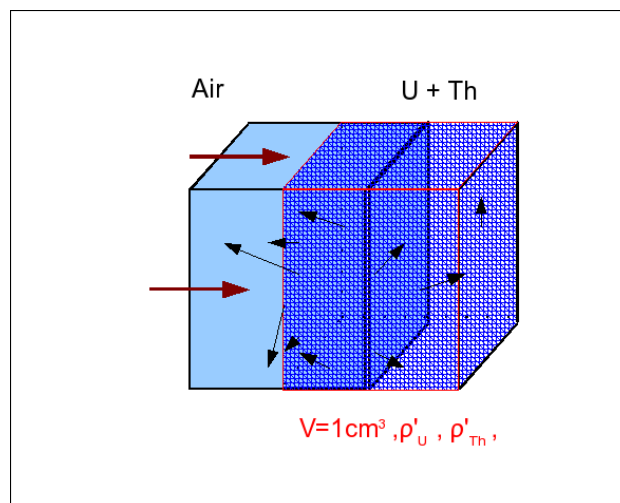


Figure 4.6: Considering (α, n) reactions in Air in SOURCES4mv. Half of the number of α particles emitted in V' in Figure 4.5 is assumed in a conservative way to leave the Green Stone rock and interact with the air volume V .

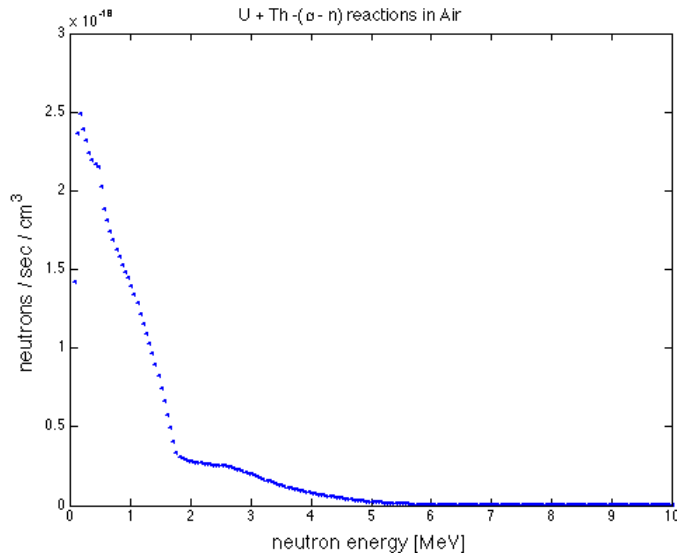


Figure 4.7: (α, n) reactions in air.

Neutron spectrum as it results from (α, n) -reactions in air due to α particles leaving the rock. A very low neutron rate of $6.1034 \cdot 10^{-17} n/s/cm^3$ is given by this spectrum.

A neutron rate of $6.1034 \cdot 10^{-17} n/s/cm^3$ is given by this spectrum. During one year one can expect $\sim 1.9 \cdot 10^{-9}$ neutrons in one cm^3 of air. This seems to be more than negligible, considering the conservative assumptions made before in order to calculate this spectrum.

4.5 Spontaneous fission

Neutron spectra from spontaneous fission, were additionally calculated by SOURCES4mv for the Copper parts of the detector, the inner polyethylene and the Green Stone rock. The same concentrations of U and Th as for the (α, n) calculations (see Table 4.3) were taken in the materials. For the Green Stone, 0.17 ppm for U and 0.89 ppm for Th were taken according to [33]. The resulting spectra are shown in Figure 4.8 and Figure 4.9. The highest neutron rates of about $1 \cdot 10^{-9} n/s/cm^3$ caused by spontaneous fission results from the cavern rock, which is due to its size not necessarily the most dangerous in terms of backgrounds.

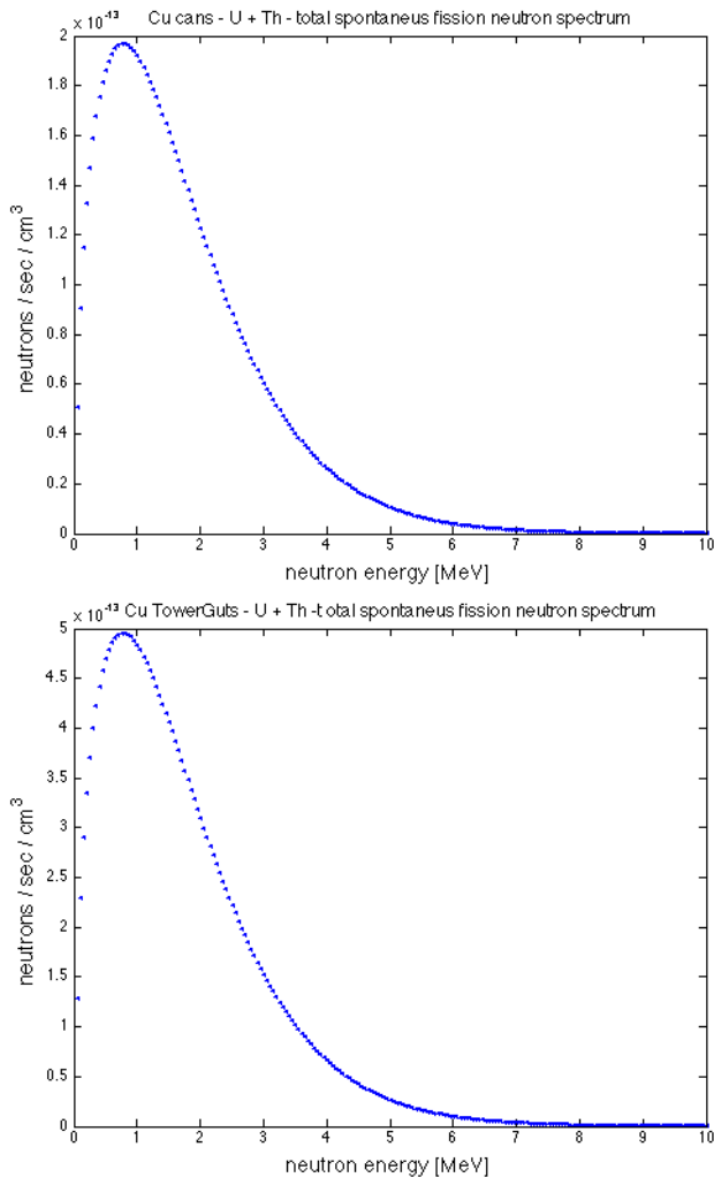


Figure 4.8: Spontaneous fission in copper.
Neutron spectra from spontaneous fission in the icebox cans and the towerguts.

The resulting total neutron rates from spontaneous fission were found to be:

- Cu-cans: $9.603 \cdot 10^{-12} n/s/cm^3$
- Cu-towerguts: $2.42 \cdot 10^{-11} n/s/cm^3$

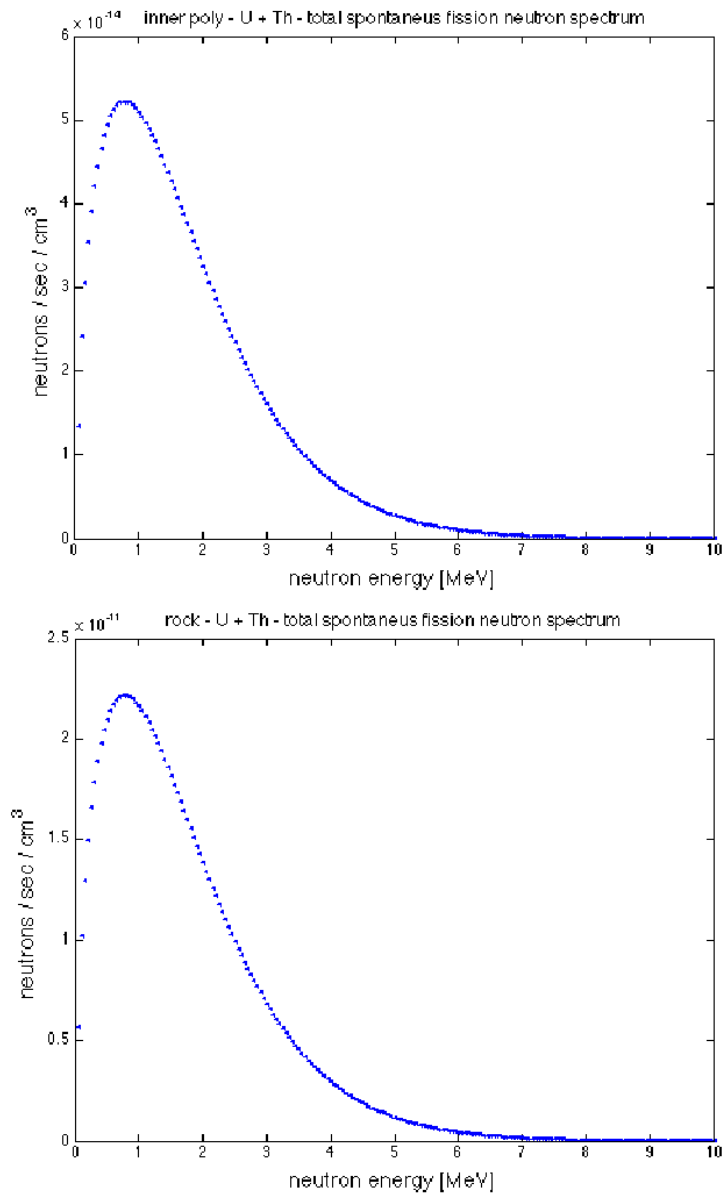


Figure 4.9: Spontaneous fission in polyethylene and the Green Stone rock. Neutron spectra from spontaneous fission in the inner poly shield and in the rock.

- inner poly: $2.548 \cdot 10^{-12} n/s/cm^3$
- rock: $1.082 \cdot 10^{-9} n/s/cm^3$

More spontaneous fission neutron spectra are shown in Appendix C.

4.6 The simulation runs

4.7 The (α, n) -runs

In order to investigate the neutron backgrounds from (α, n) reactions in the Soudan mine and in the CDMS detector, the spectra in Figures 4.1 and 4.2 were normalized and added to the GEANT4 code as neutron emission probability functions. For the detectors cans, towerguts and the inner polyshield, all elements listed in Table 4.2 were separately simulated as neutron sources, exhibiting the accordant neutron energy spectra. Tables 4.9, 4.10 and 4.11 show the simulated CDMS parts, their volumina, the corresponding neutron production rates, the number of neutrons thrown and the resulting simulated exposure time. Because the inner poly has a big volume and a high neutron-interaction rate, the exposure time of it was reduced by factor 10 in order to spare simulation time.

Cans (V [cm^3])	neutrons thrown
OVC (3938.674)	6100401
OVC-cap (3911.367)	6058106
OVC-base (3911.367)	6058106
Liquid N (3146.6079)	4873612
Liquid N-cap (632.113)	979046
Liquid N-base (632.113)	979046
IVC (2606.725)	4037416
IVC-cap (2489.72)	3856193
IVC-base (2489.72)	3856193
Still can (1652.532)	2559518
Still-cap (143.31)	221965
Still-base (401.976)	622599
Cold-can (1317.72)	2040946
Cold-cap (91.467)	141668
Cold-base (315.324)	488388
Base-can (949.349)	1470396
Base-cap (129.459)	200513
Base-base (228.972)	354642
(α, n) neutron-rate [$n/s/cm^3$]	$1.2322 \cdot 10^{-11}$
total simulated exposure time[a]	3973341

Table 4.9: Considered (α, n) sources of the icebox.

Neutrons from the cavern rock can produce a background only if they are not absorbed in the rock. To estimate the layer in rock, which could produce such neutrons, a simulation for determining the neutron ranges in rock was performed first. This was done in the same way like previously for α -ranges. Using the spec-

5xTowerguts (V [cm³])	neutrons thrown
upper tower (5x224.215)	4841930
upper tower base (5x26.121)	541956
connectortube (5x15.695)	325639
connectortube-basering(5x5.717)	118626
detectorhousing-cap(5x7.959)	165146
detectorhousing (5x43.049)	893182
detectorhousing-base (5x8.744)	181427
side-coaxes ($\sum : 7.244$)	$\sum : 150254$
(α, n) neutron-rate [n/s/cm ³]	$3.3117 \cdot 10^{-11}$
total simulated exposure time[a]	3973341

Table 4.10: Considered (α, n) sources nearby the detectors

Polyshield (V [cm³])	neutrons thrown
innerpoly (81227.678)	8081420
innerpoly cap (20391.492)	2030253
innerpoly base (27188.657)	2706969
(α, n) neutron-rate [n/s/cm ³]	$7.94 \cdot 10^{-12}$
total simulated exposure time[a]	397334

Table 4.11: Considered (α, n) poly-sources

trum in Figure 4.2 the average energy \bar{E}_{n-rock} of (α, n) -neutrons produced in the rock was found to be

$$\bar{E}_{n-rock} \approx 1.835 \text{ MeV} \quad (4.15)$$

Neutrons at this energy were thrown at a polyethylene target, whose thickness was varied between 0 and 45 cm. The transmission plots are shown in Figure 4.10. Based on this plots, a roughly mean neutron range of about 5 cm can be estimated. Anyway, the neutron intensity is not decreasing as rapidly as in the case of α 's and a considerably fraction of neutrons is still transmitted at ranges of more than 10 cm. Hence a rock-wall thickness of 30 cm was taken in the simulation to conservatively define the neutron-active layer of rock.

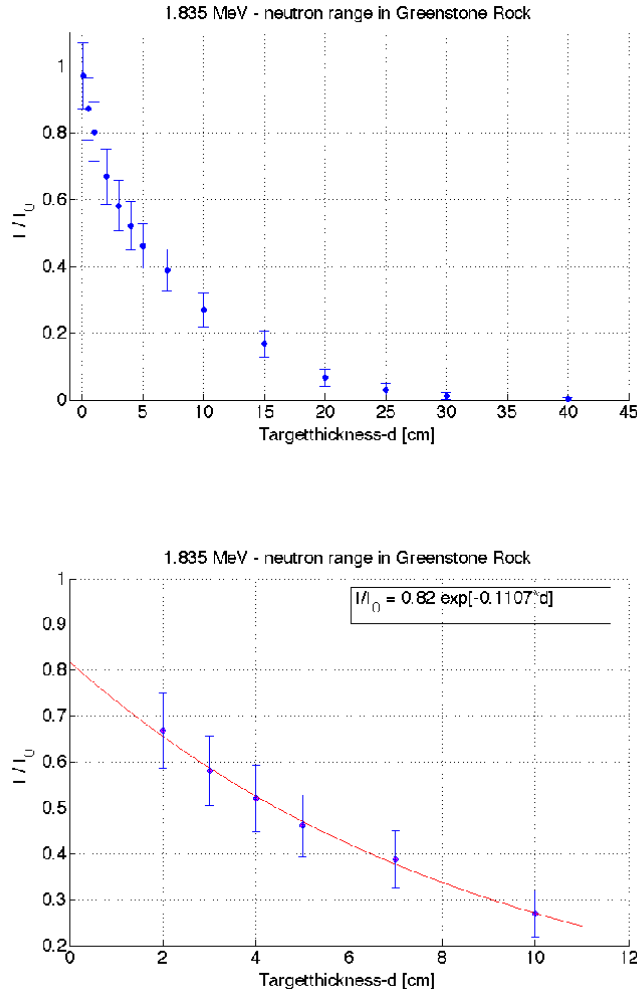


Figure 4.10: Neutron ranges in the Green Stone rock.
Neutron transmission as function of target-thickness for neutrons at a mean (α, n) -energy of 1.835 MeV. Target material is the Green Stone rock.

Based on the report about the Soudan-mine in [33] a cavern geometry with dimensions of 14x14x74m meter, with a wall thickness of 0.3m was added to GEANT4 and used as neutron source with an emission probability distribution given by the spectra in Figure 4.2 after normalizing. The GEANT4 cavern geometry used for simulating (α, n) neutron backgrounds from the rock can be seen in Figure 4.11.

Due to time pressure, only $20 \cdot 10^6$ rock neutrons were thrown in this simulation. Because of the big volume of the cavern of $\sim 1.5 \cdot 10^9 \text{ cm}^3$, its low neutron emission rates and the vast amount of time consuming neutron scattering in this volume, the run-time of this simulation is very high. Hence the simulated exposure time in

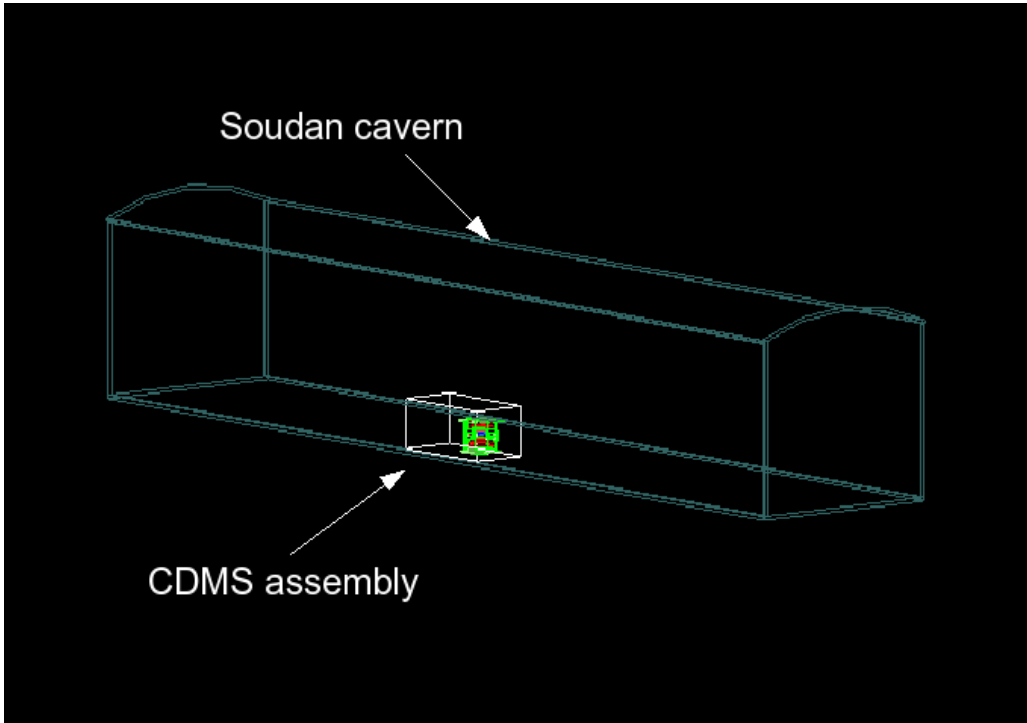


Figure 4.11: Cavern geometry in GEANT4.

Cavern geometry used as active volume for neutrons from (α, n) -reactions in the Soudan rock surrounding CDMS. The chemical composition of the cavern is that of the Green Stone rock. Its size is: 14x14x74 m with a wall thickness of 0.3 m.

this MC-run is comparatively low and corresponds only to 0.114 years. No events of any kind occurred during this run in the detectors.

Cavern-Volume [cm³]	$\sim 1.5 \cdot 10^9$
neutrons thrown	$20 \cdot 10^6$
(α, n) neutron-rate [n/s/cm ³]	$3.737 \cdot 20^{-9}$
total simulated exposure time [a]	0.114

Table 4.12: The (α, n) Green Stone run.

4.8 Spontaneous fission - the inner poly run

Due to its relatively high concentration limits of about 0.2 ppb on U and Th, its high volume and the close location to the detectors, the inner polyethylene shield could be the most dangerous in terms of backgrounds from spontaneous fission. In order to allow conclusions about possible upper limits on neutron backgrounds from spontaneous fission, a final run was performed, using the inner polyethylene shield as a neutron source, whose energy distribution is characterized by the normalized spontaneous fission spectrum shown at the top of Figure 4.9. The run time of 397334 years of exposure was chosen to be the same as for the (α, n) -polyethylene run. Details of this run are shown in Table 4.13.

SF-Polyshield (V [cm ³])	neutrons thrown
innerpoly (81227.678)	2593383
innerpoly cap (20391.492)	651032
innerpoly base (27188.657)	868056
Spontaneous fission neutron-rate [n/s/cm ³]	$2.548 \cdot 10^{-12}$
total simulated exposure time [a]	397334

Table 4.13: The spontaneous fission inner poly run.

The resulting neutron rate is about a factor of ~ 3 smaller than the rate obtained by (α, n) reactions.

Chapter 5

Results and discussion

Table 5.1 shows the U and Th concentrations, which were assumed to be present in the simulated parts at Soudan. Table 5.2 shows the resulting atomdensities of U and Th, used in SOURCES4mv to calculate the occurring neutron spectras of (α, n) -reactions, as well as the neutron spectras from spontaneous fission of U and Th contained in the simulated components.

Component group	U concentration	Th concentration
Cu cans	0.0797 ppb	0.2989 ppb
Cu towerguts	0.2 ppb	1 ppb
inner polyshield	0.2 ppb	0.2 ppb
Green Stone rock	0.17 ppm	0.89 ppm

Table 5.1: Concentrations of U and Th used for the simulations.

Component group	U [$\frac{atoms}{cm^3}$]	Th [$\frac{atoms}{cm^3}$]
Cu cans	$1.79 \cdot 10^{12}$	$6.92 \cdot 10^{12}$
Cu towerguts	$4.49 \cdot 10^{12}$	$2.32 \cdot 10^{13}$
inner polyshield	$4.73 \cdot 10^{11}$	$4.85 \cdot 10^{11}$
Green Stone rock	$1.23 \cdot 10^9$	$6.58 \cdot 10^9$

Table 5.2: Atomdensities of U and Th used in SOURCES4mv.

The spectras were calculated separately for U,Th and U+Th and are shown in Appendix B for (α, n) -reactions and in Appendix C for SF-reactions. The isotopic natural abundancies of Copper, Polyethylene and the elements of the Green Stone composition were also taken into account in SOURCES4mv. The obtained total neutron-rates are shown in Table 5.3 for (α, n) -reactions and Table 5.4 for SF-reactions. While neutrons arising from (α, n) -reactions and SF of Uranium are of about the same order, the Thorium spectras are clearly dominated by its (α, n)

component, which is a factor $\sim 10^5$ higher than the neutron rates from SF of Th. In order to estimate the neutron backgrounds at CDMS, arising from the U and Th contaminations of the Soudan cavern rock and the CDMS assembly, the calculated and normalized spectra were used in the GEANT4 code as neutron emission probabilities. All components listed in Table 4.2 were then separately set as active neutron-emission volumes with the according (α, n) spectrum. The active volume of the rock cavern was defined in GEANT4 after estimating the neutron ranges in the Green Stone first. Neutron rates from (α, n) -reactions in air, caused by α -particles leaving the rock were estimated to be negligible with calculated neutron rates of $\sim 6.1 \cdot 10^{-17} n/s/cm^3$. This value represents a very conservative upper limit and concerns air molecules in the direct neighbourhood of the rock-wall. Hence a GEANT4 simulation of the caverns air volume was set aside.

Component group - (α, n)	U [$n/s/cm^3$]	Th [$n/s/cm^3$]	U+Th [$n/s/cm^3$]
Cu cans	$9.82 \cdot 10^{-12}$	$2.5 \cdot 10^{-12}$	$1.23 \cdot 10^{-11}$
Cu towerguts	$2.47 \cdot 10^{-11}$	$8.37 \cdot 10^{-12}$	$3.31 \cdot 10^{-11}$
Inner Polyshield	$5.22 \cdot 10^{-12}$	$2.71 \cdot 10^{-12}$	$7.94 \cdot 10^{-12}$
Green Stone rock	$3.64 \cdot 10^{-9}$	$9.42 \cdot 10^{-11}$	$3.74 \cdot 10^{-9}$

Table 5.3: Neutron rates resulting from (α, n) -reactions at Soudan.

Component group - (SF)	U [$n/s/cm^3$]	Th [$n/s/cm^3$]	U+Th [$n/s/cm^3$]
Cu cans	$9.6 \cdot 10^{-12}$	$3.27 \cdot 10^{-16}$	$9.6 \cdot 10^{-12}$
Cu towerguts	$2.42 \cdot 10^{-11}$	$1.1 \cdot 10^{-15}$	$2.42 \cdot 10^{-11}$
Inner Polyshield	$2.55 \cdot 10^{-12}$	$2.29 \cdot 10^{-17}$	$2.55 \cdot 10^{-12}$
Green Stone rock	$1.1 \cdot 10^{-9}$	$3.27 \cdot 10^{-16}$	$1.1 \cdot 10^{-9}$

Table 5.4: Neutron rates resulting from spontaneous fission of U and Th at Soudan.

The highest neutron production rates result from (α, n) -reactions and spontaneous fission in the rock, which are about a factor of 10 higher than neutron rates arising from cosmic ray interactions in the rock. The latter were determined in [23] to be about $7.2 \cdot 10^{-8} n/kg/s \sim 2 \cdot 10^{-10} n/s/cm^3$. This shows the importance of estimating the backgrounds from natural radioactivity as one goes deeper underground. Furthermore a GEANT4 neutron simulation of SF was performed only for the polyethylene inner shield, which seems to be the most dangerous in terms of a possible neutron background.

All data obtained by the simulations were rescaled with individual factors for every detector. These factors were previously determined by comparing the simulated ^{252}Cf -calibrations with real calibration runs. The mean neutron rates for nuclear recoils and single events for all detectors, obtained by the performed simulations

are listed in Table 5.5. The weakest neutron background seems to be produced by spontaneous fission reactions in polyethylene. Anyway this background is just a component of the polyethylene-shield's total spectra, which is composed of its (α, n) and spontaneous fission neutrons. The combined total rate of polyethylene is of about the same order than those of the other simulated Copper elements. There is no clearly dominating neutron background source among the simulated parts.

Source	Rates in Ge [$\frac{\text{neutrons}}{\text{kg}\cdot\text{year}}$]	Rates in Si [$\frac{\text{neutrons}}{\text{kg}\cdot\text{year}}$]
(α, n) -Cans: n.r. (**)	$2.59 \cdot 10^{-2} \pm 1.6 \cdot 10^{-4}$	$6.97 \cdot 10^{-2} \pm 4.2 \cdot 10^{-4}$
single recoils	$5.5 \cdot 10^{-3} \pm 7.4 \cdot 10^{-5}$	$1.41 \cdot 10^{-2} \pm 1.9 \cdot 10^{-4}$
(α, n) -Guts: n.r.	$1.32 \cdot 10^{-2} \pm 1.1 \cdot 10^{-4}$	$4.11 \cdot 10^{-2} \pm 3.2 \cdot 10^{-4}$
single recoils	$2.8 \cdot 10^{-3} \pm 5.3 \cdot 10^{-5}$	$8.9 \cdot 10^{-3} \pm 1.5 \cdot 10^{-4}$
(α, n) -Poly: n.r.	$1.24 \cdot 10^{-2} \pm 3.5 \cdot 10^{-4}$	$3.3 \cdot 10^{-2} \pm 9.1 \cdot 10^{-4}$
single recoils	$2.7 \cdot 10^{-3} \pm 1.6 \cdot 10^{-4}$	$7 \cdot 10^{-3} \pm 4.2 \cdot 10^{-4}$
(α, n) -Rock: n.r.	0(***)	0(***)
single recoils	0(***)	0(***)
(SF)-Poly: n.r.	$3.2 \cdot 10^{-3} \pm 1.8 \cdot 10^{-4}$	$9 \cdot 10^{-3} \pm 4.8 \cdot 10^{-4}$
single recoils	$6.85 \cdot 10^{-4} \pm 8.2 \cdot 10^{-5}$	$1.8 \cdot 10^{-3} \pm 2.1 \cdot 10^{-4}$
Total: nr.	$5.47 \cdot 10^{-2} \pm 8 \cdot 10^{-4}$	$15.28 \cdot 10^{-2} \pm 2.13 \cdot 10^{-3}$
single recoils	$1.2 \cdot 10^{-2} \pm 3.7 \cdot 10^{-4}$	$3.18 \cdot 10^{-2} \pm 9.7 \cdot 10^{-4}$

Table 5.5: Expected neutron rates in the detectors from (α, n) and spontaneous fission (SF) reactions at Soudan in an energy range of 7-100 keV.

(**): n.r. \equiv nuclear recoils in the nuclear bands,

(***): 0 events for an exposure time of 0.114 years.

Although the cavern rock in the mine was also simulated, not even one single event occurred during the run of $20 \cdot 10^6$ neutrons thrown, corresponding to about 40 days of exposure. Due to the rocks volume in the simulation of about $1.5 \cdot 10^9 \text{ cm}^3$, much more simulation time must be invested in order to reach statistics which would allow reliable predictions on the neutron backgrounds, caused by the cavern. All rates in Table 5.5 include the correction factors from the Tables 3.4 and 3.5 for nuclear and nuclear-single events, which were necessary in terms of agreement between the ^{252}Cf calibration runs and the MonteCarlo simulations. The spectra for nuclear recoils which result after applying this individual correction factors to the MonteCarlo data are shown in Appendix A. Obviously their distribution can be well reproduced. Most of this correction factors for events in the nuclear recoil bands are very close to unity, and the discrepancy could be an individual effect of each detector or their readout electronics. The position of the calibration source has also an influence on the detector responses. In contrast to the simulations, this position is never identical to its previous in real calibrations runs. One should

be more worried about the discrepancy of the single event rates. The scale factors for single nuclear recoils in Table 3.5 are about a factor of two lower than those for all nuclear recoils, and indicate more a problem in the MC-simulations or the analysis procedure. Anyway, the single event spectra distribution could be also well reproduced by the MonteCarlo after rescaling. An example is shown in Figure 5.1. Hence rescaling the single events in the analysis seems to be a reliable way to make rough predictions on the neutron single rates.

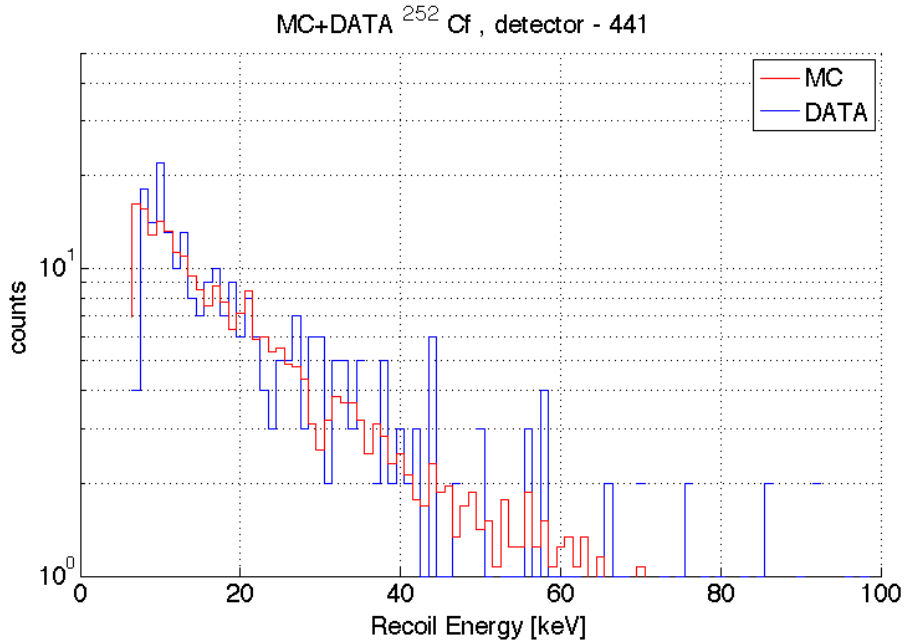


Figure 5.1: Single events spectrum.
Example of a rescaled ^{252}Cf spectra for single events.

The MC event rates in Si for nuclear recoils and nuclear-single events are about a factor of $\sim 2 - 3$ higher than in the Ge detectors. In contrast, the WIMP rates in the Ge detectors should be a factor of 5-7 higher than in Si with an expected upper limit rate of $< 1\text{event}/1\text{keV}/\text{kg}/\text{day}$ [24]. The reason for the higher rates in Si could be - if there is no mistake - the extremely high energy dependence of the Si cross sections especially at neutron energies $\lesssim 3\text{MeV}$.

The calculated total neutron rates shown in Table 5.5 for both, Ge and Si are about $\sim 21 \cdot 10^{-2} \frac{n}{\text{kg}\cdot\text{year}}$ for all nuclear events and $\sim 4.5 \cdot 10^{-2} \frac{n}{\text{kg}\cdot\text{year}}$ for single nuclear recoils. The latter could be mistaken as WIMP interaction events. The CDMS assembly was designed for event rates of $\sim 0.01\text{events}/\text{kg}/\text{keV}/\text{day}$ from all backgrounds. Neutrons from spontaneous fission in the Cu-components of the detector and in the Soudan cavern rock were not simulated in this work, but even if they additionally contribute neutron rates similar to those obtained by (α, n) -reactions, the total background rate would stay much lower than $0.01\text{events}/\text{kg}/\text{keV}/\text{day}$.

Although neutrons from (α, n) -reactions and spontaneous fission in the detector can not be vetoed or shielded, their rate seem not to be very relevant for current experiments.

Appendix A

^{252}Cf -neutron calibration spectras

Table A.1 shows the different but equivalent names for all 30 detectors mounted in the 5 towers of CDMS II.

The following graphics show the ^{252}Cf spectras caused by nuclear recoil events compared to those obtained by the MonteCarlo simulations, after individual rescaling by the factor fnr.

Detector 1	T1Z1	401	G6
Detector 2	T1Z2	402	G11
Detector 3	T1Z3	403	G8
Detector 4	T1Z4	404	S3
Detector 5	T1Z5	405	G9
Detector 6	T1Z6	406	S1
Detector 7	T2Z1	411	S14
Detector 8	T2Z2	412	S28
Detector 9	T2Z3	413	G13
Detector 10	T2Z4	414	S25
Detector 11	T2Z5	415	G31
Detector 12	T2Z6	416	S26
Detector 13	T3Z1	421	S17
Detector 14	T3Z2	422	G25
Detector 15	T3Z3	423	S30
Detector 16	T3Z4	424	G33
Detector 17	T3Z5	425	G32
Detector 18	T3Z6	426	G29
Detector 19	T4Z1	431	S12
Detector 20	T4Z2	432	G37
Detector 21	T4Z3	433	S10
Detector 22	T4Z4	434	G35
Detector 23	T4Z5	435	G34
Detector 24	T4Z6	436	G38
Detector 25	T5Z1	441	G7
Detector 26	T5Z2	442	G36
Detector 27	T5Z3	443	S29
Detector 28	T5Z4	444	G26
Detector 29	T5Z5	445	G39
Detector 30	T5Z6	446	G24

Table A.1: Four different detector designations used in the 5 tower CDMS assembly. G and S in the last column refer to Germanium and Silicon respectively.

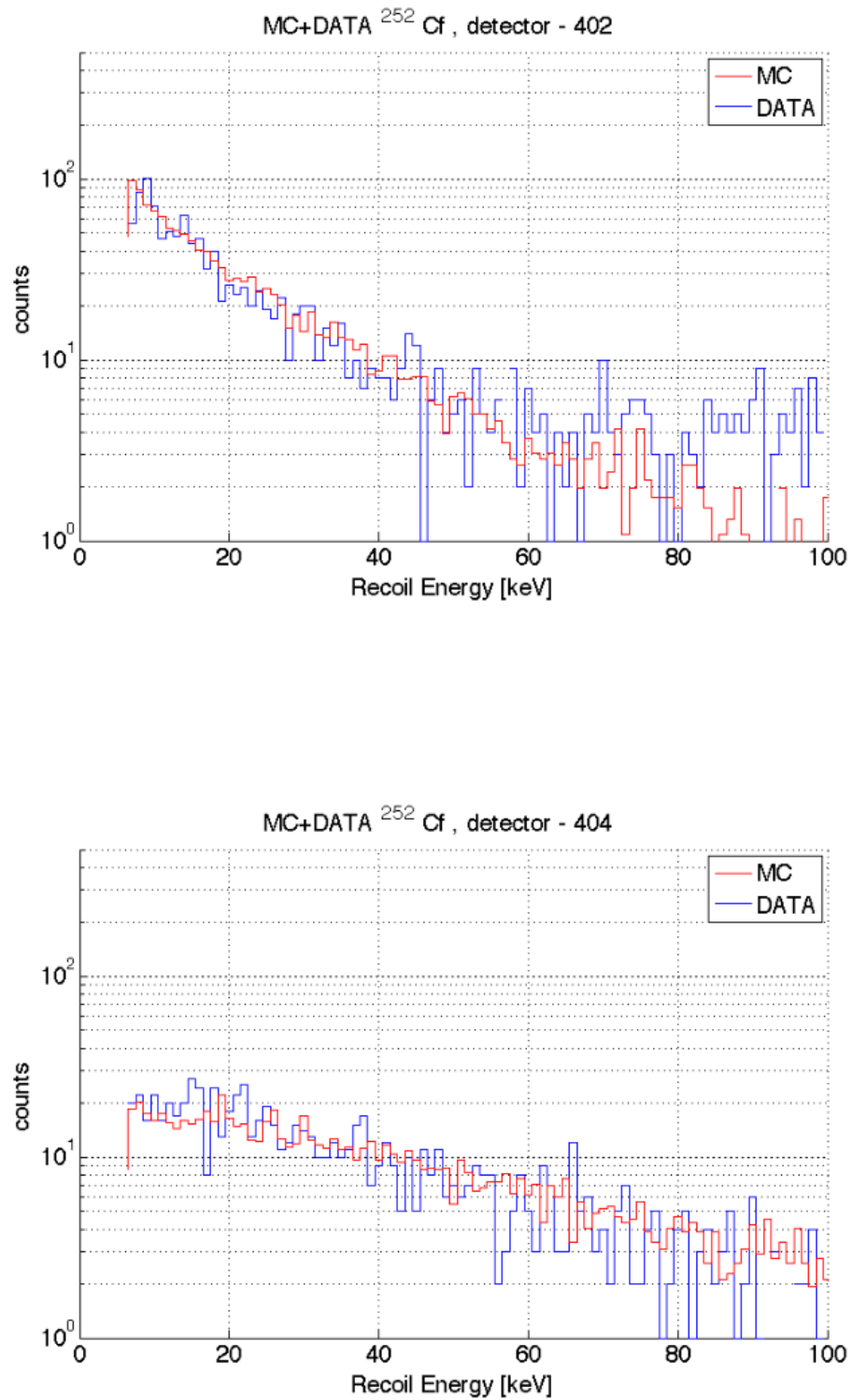


Figure A.1: ^{252}Cf -MC/Data - nuclear recoil spectras in detektors 402 and 404

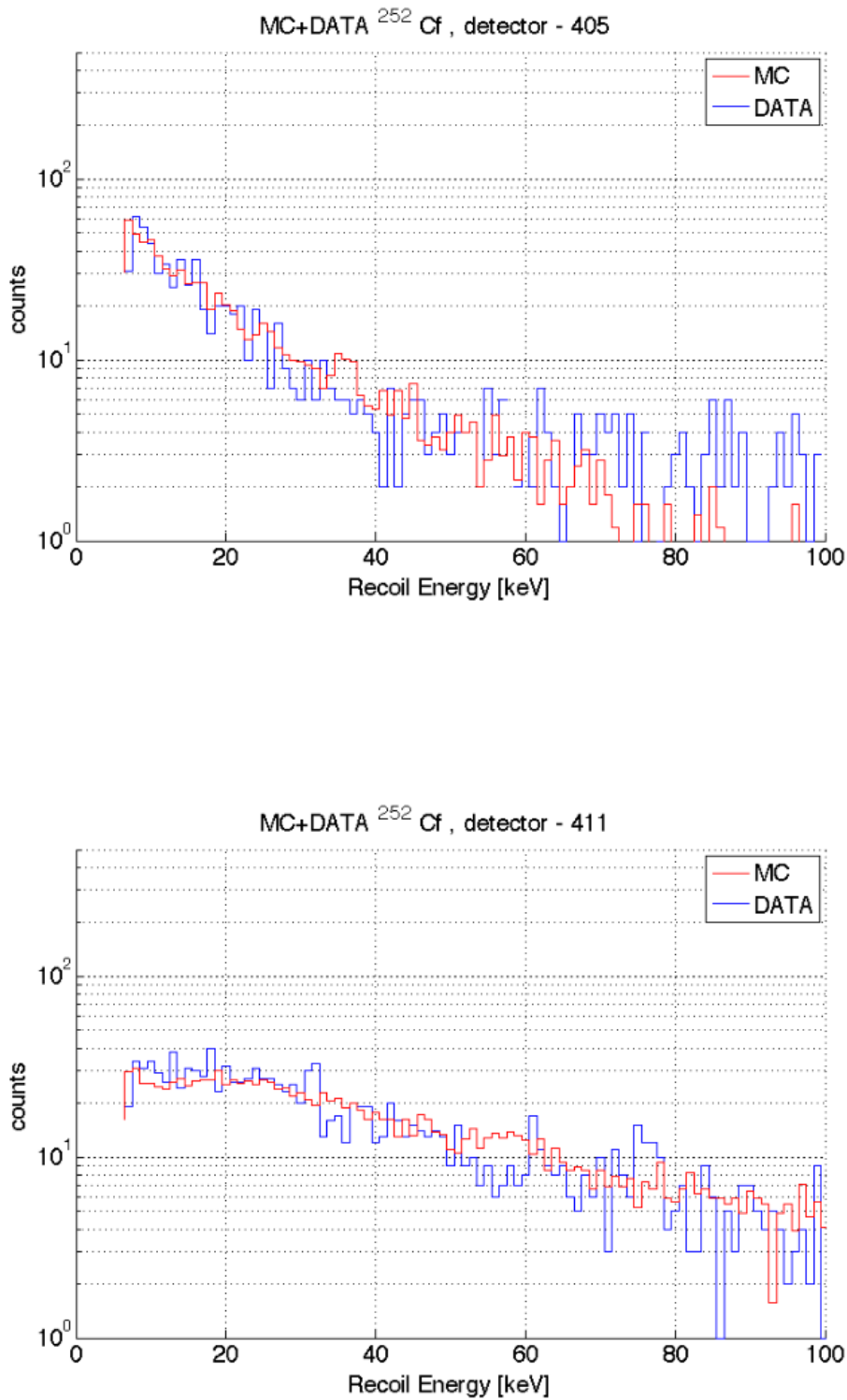


Figure A.2: ^{252}Cf -MC/Data - nuclear recoil spectras in detektors 405 and 411

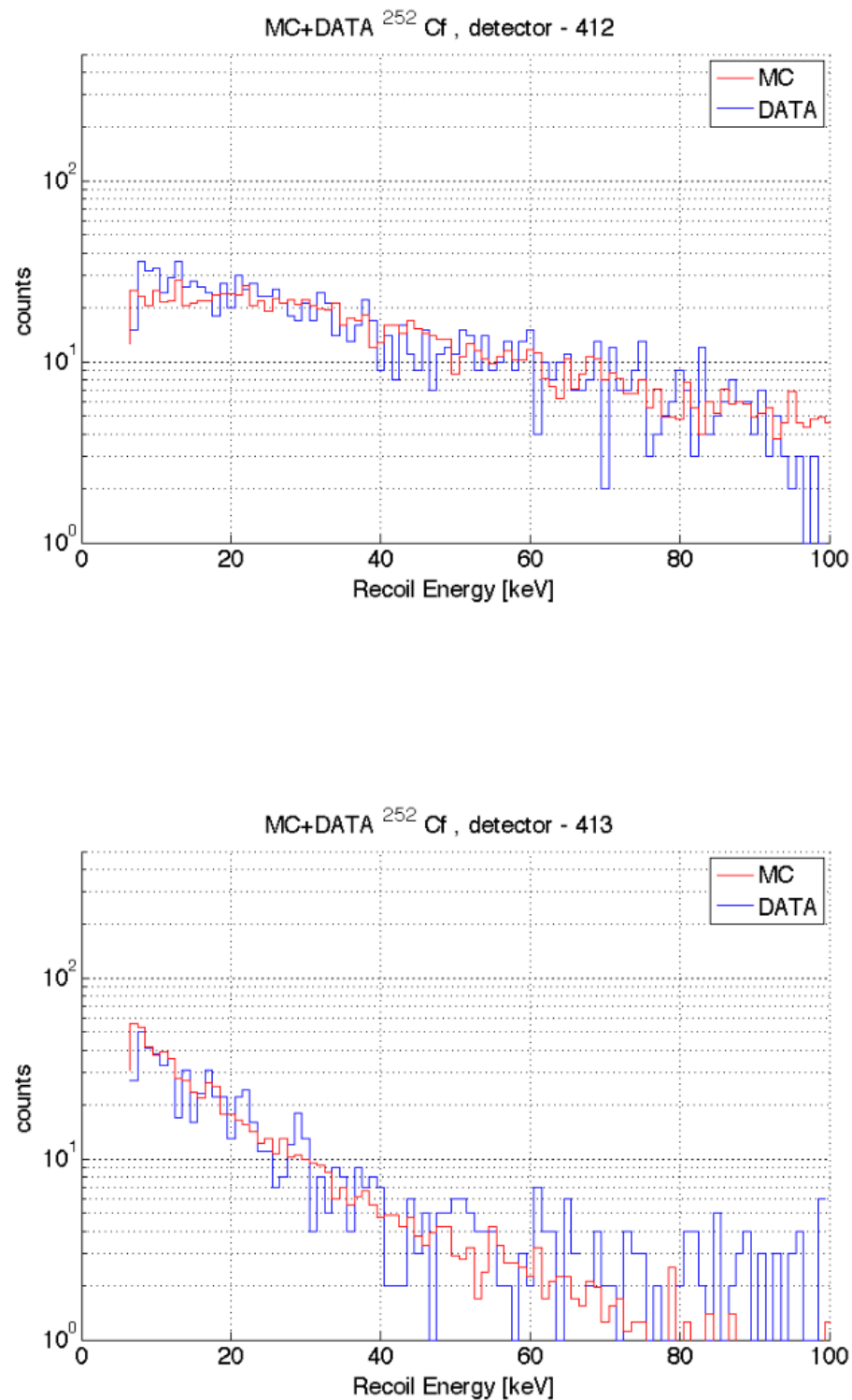


Figure A.3: ^{252}Cf -MC/Data - nuclear recoil spectras in detektors 412 and 413

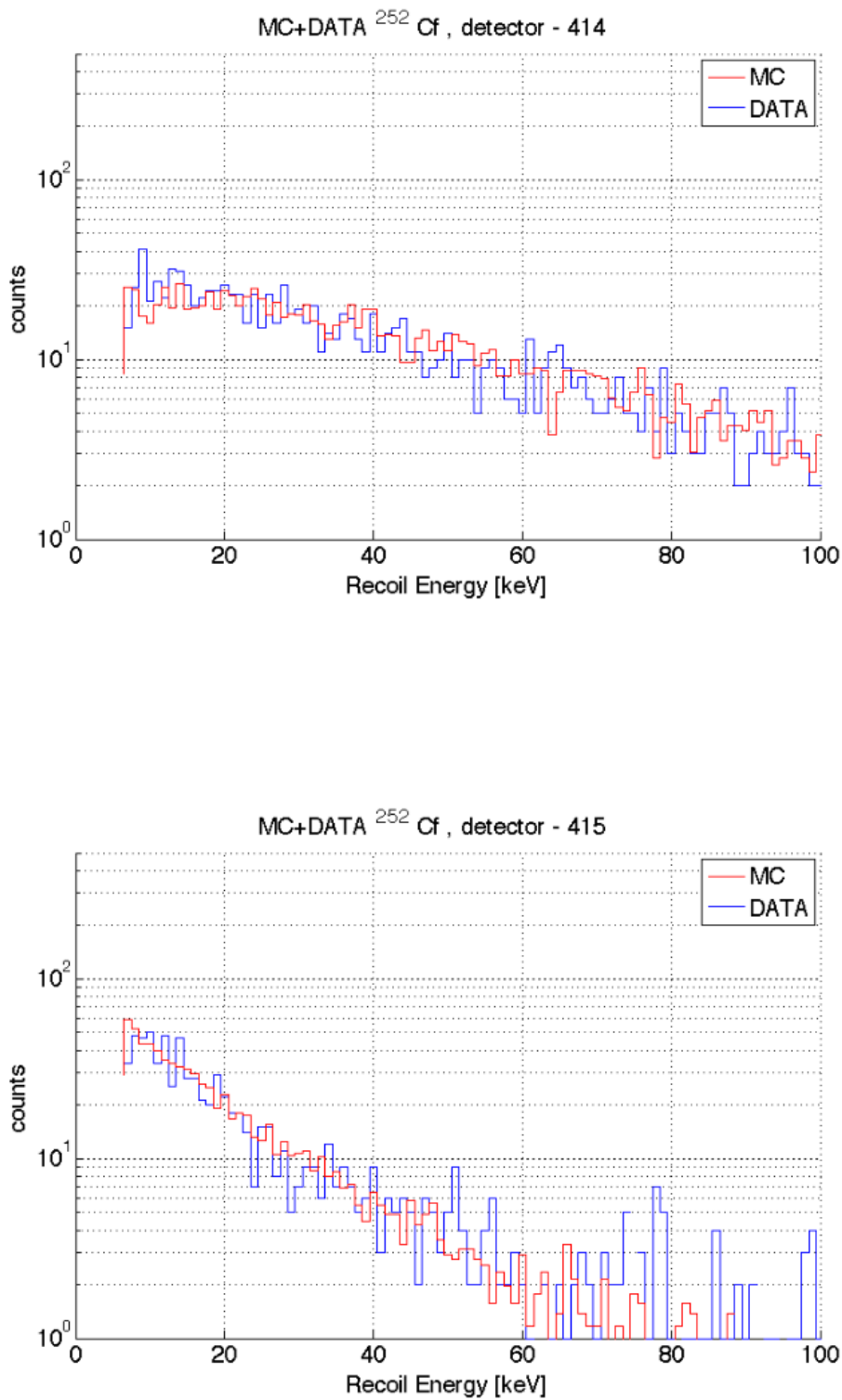


Figure A.4: ^{252}Cf -MC/Data - nuclear recoil spectras in detektors 414 and 415

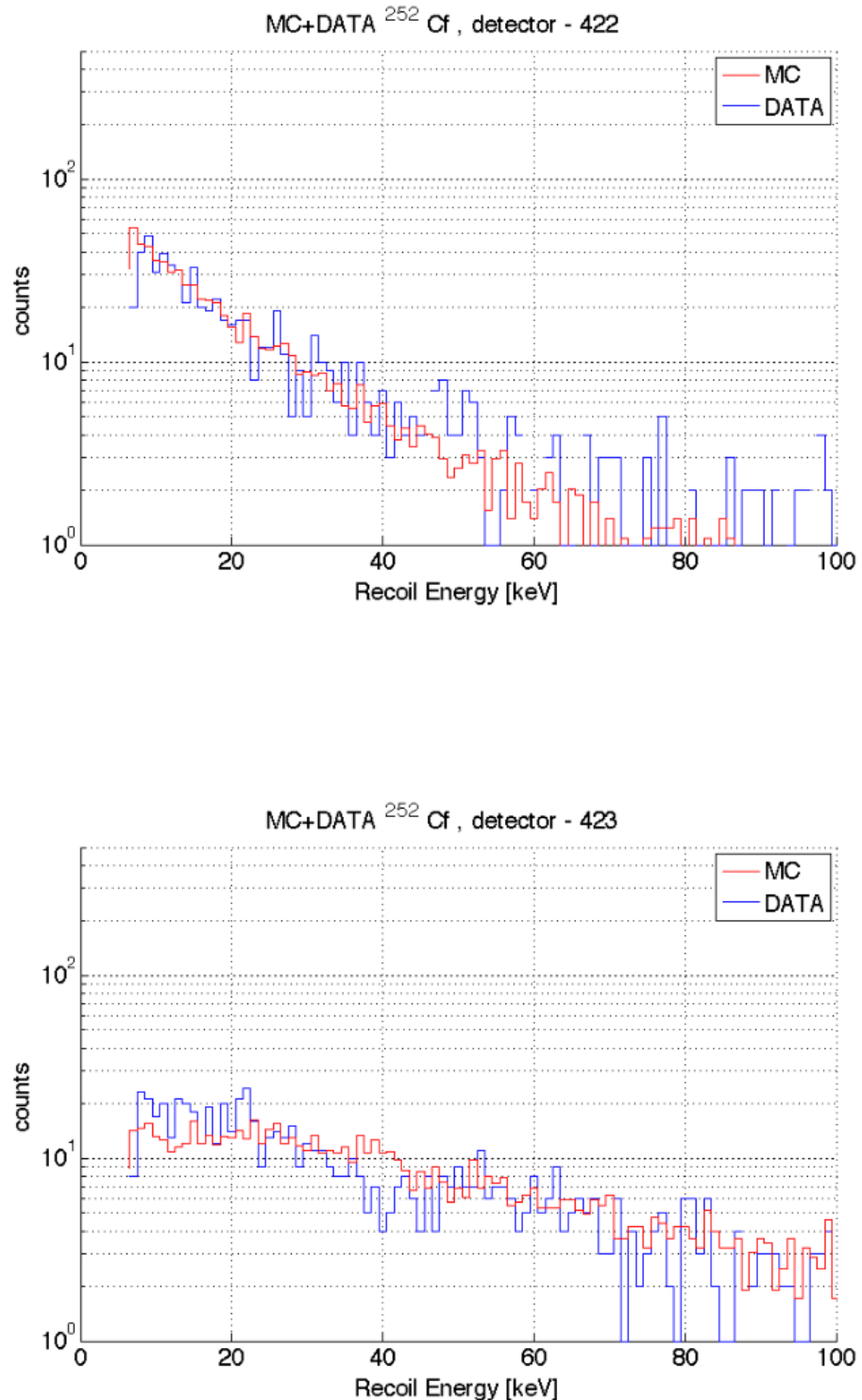


Figure A.5: ^{252}Cf -MC/Data - nuclear recoil spectras in detektors 423 and 422

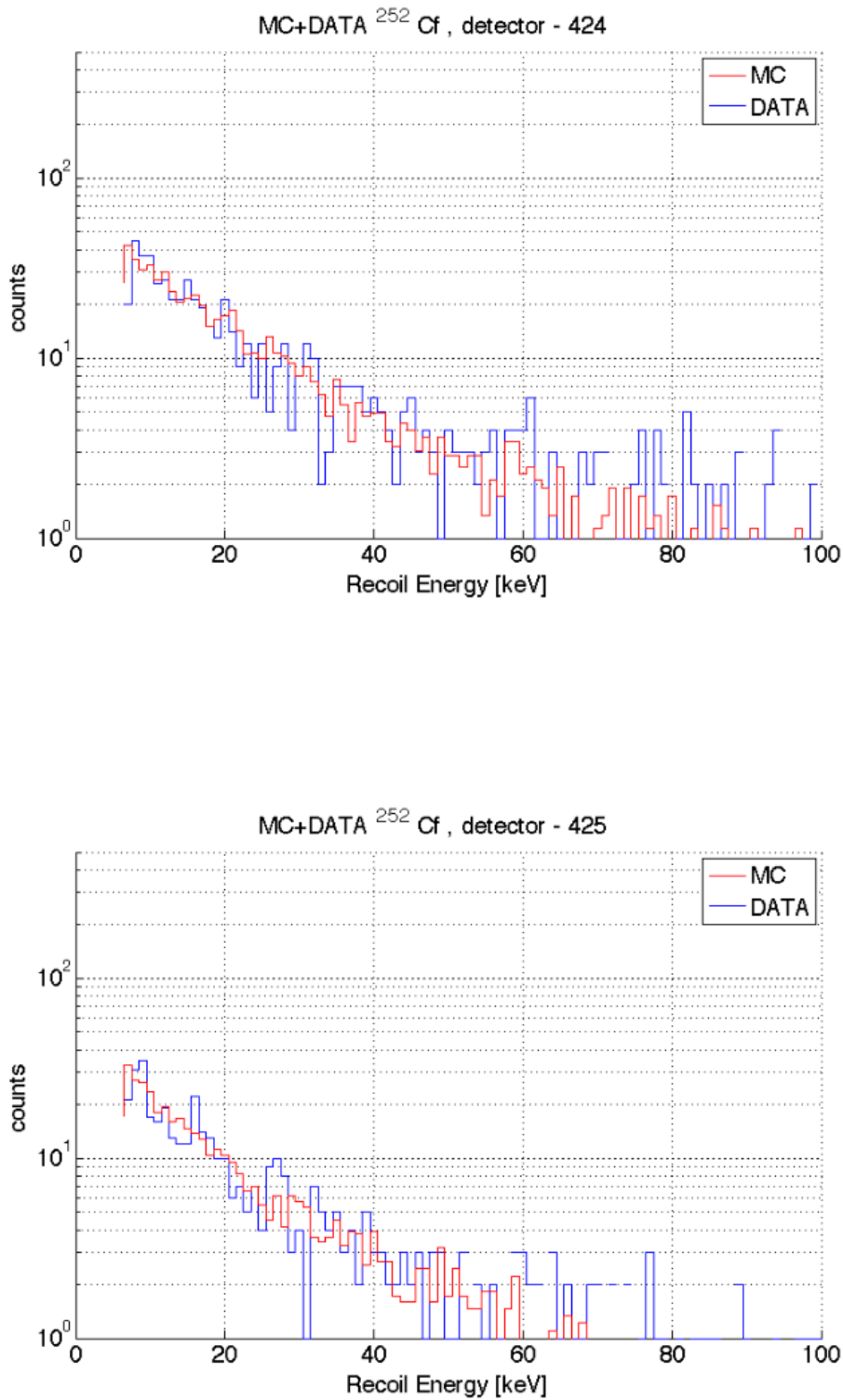


Figure A.6: ^{252}Cf -MC/Data - nuclear recoil spectras in detektors 424 and 425

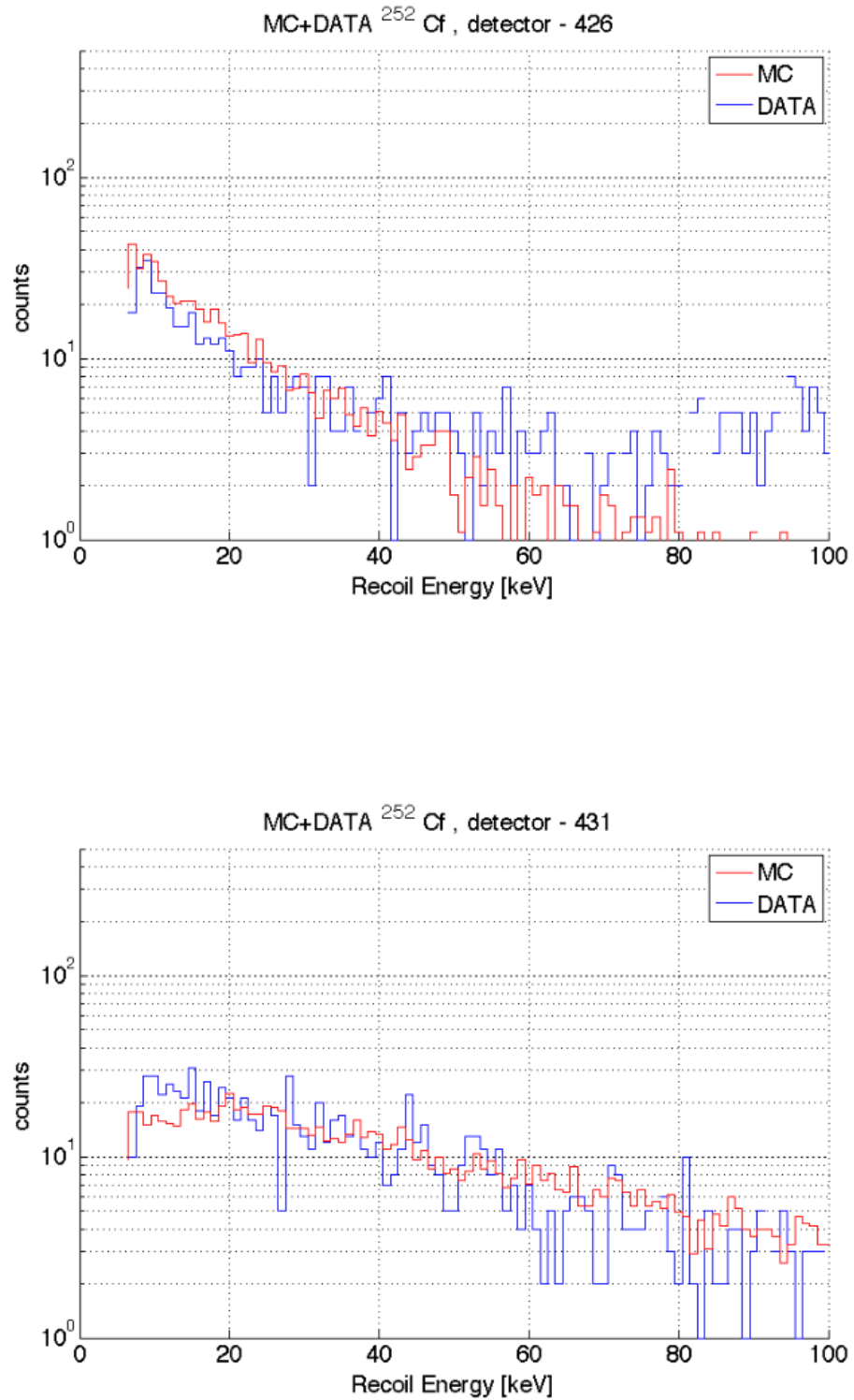


Figure A.7: ^{252}Cf -MC/Data - nuclear recoil spectra in detektors 426 and 431

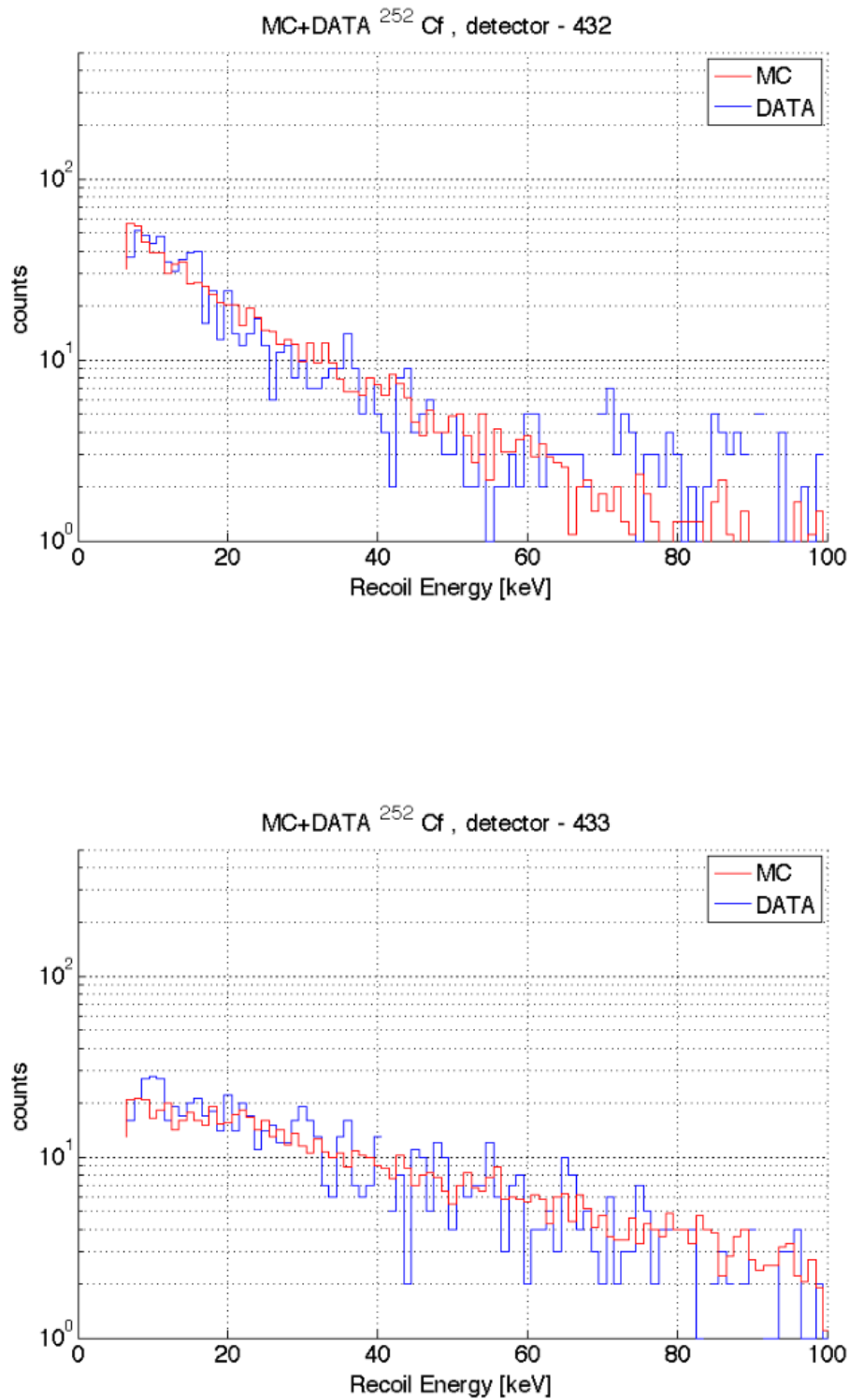


Figure A.8: ^{252}Cf -MC/Data - nuclear recoil spectras in detektors 432 and 433

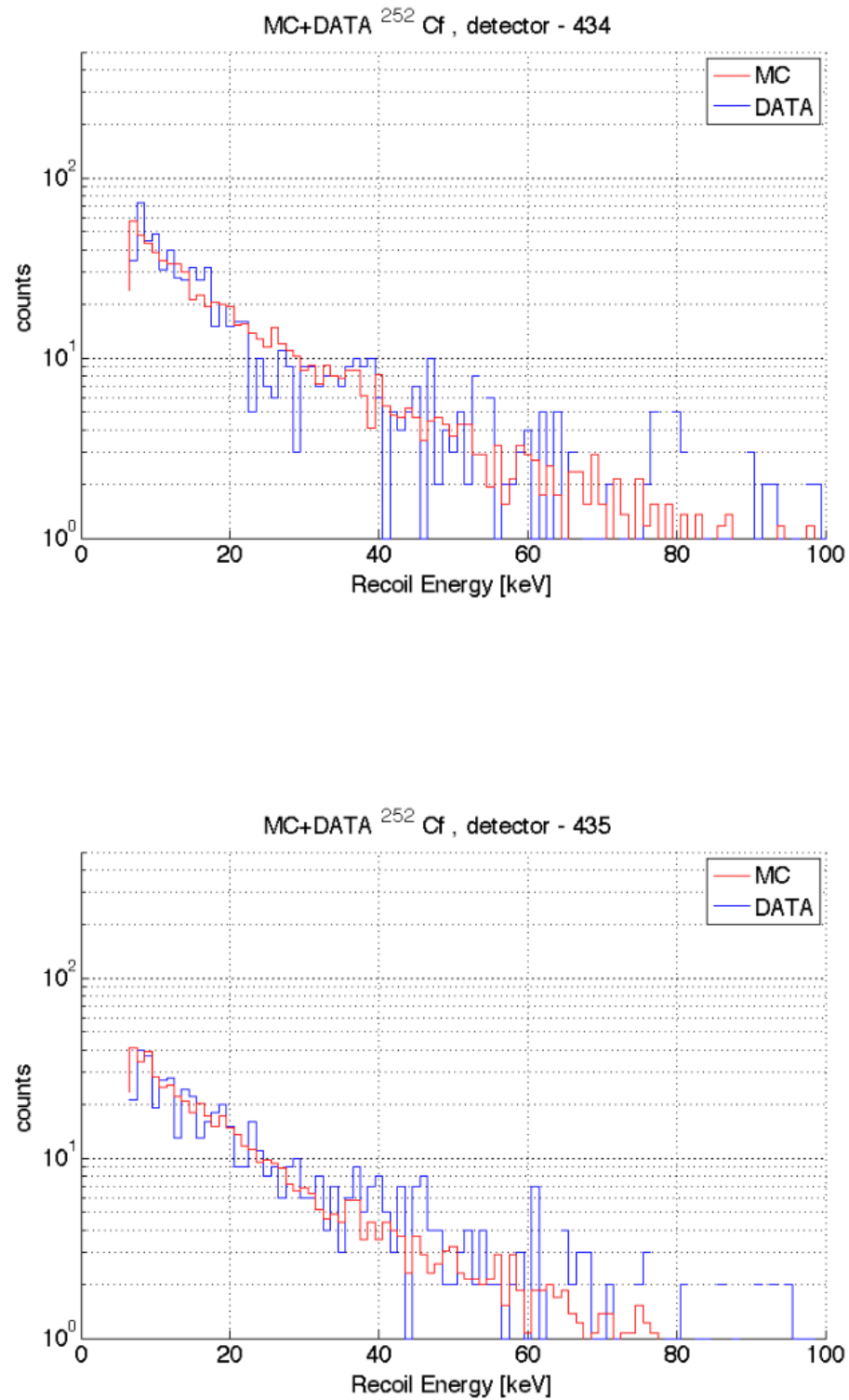


Figure A.9: ^{252}Cf -MC/Data - nuclear recoil spectras in detektors 434 and 435

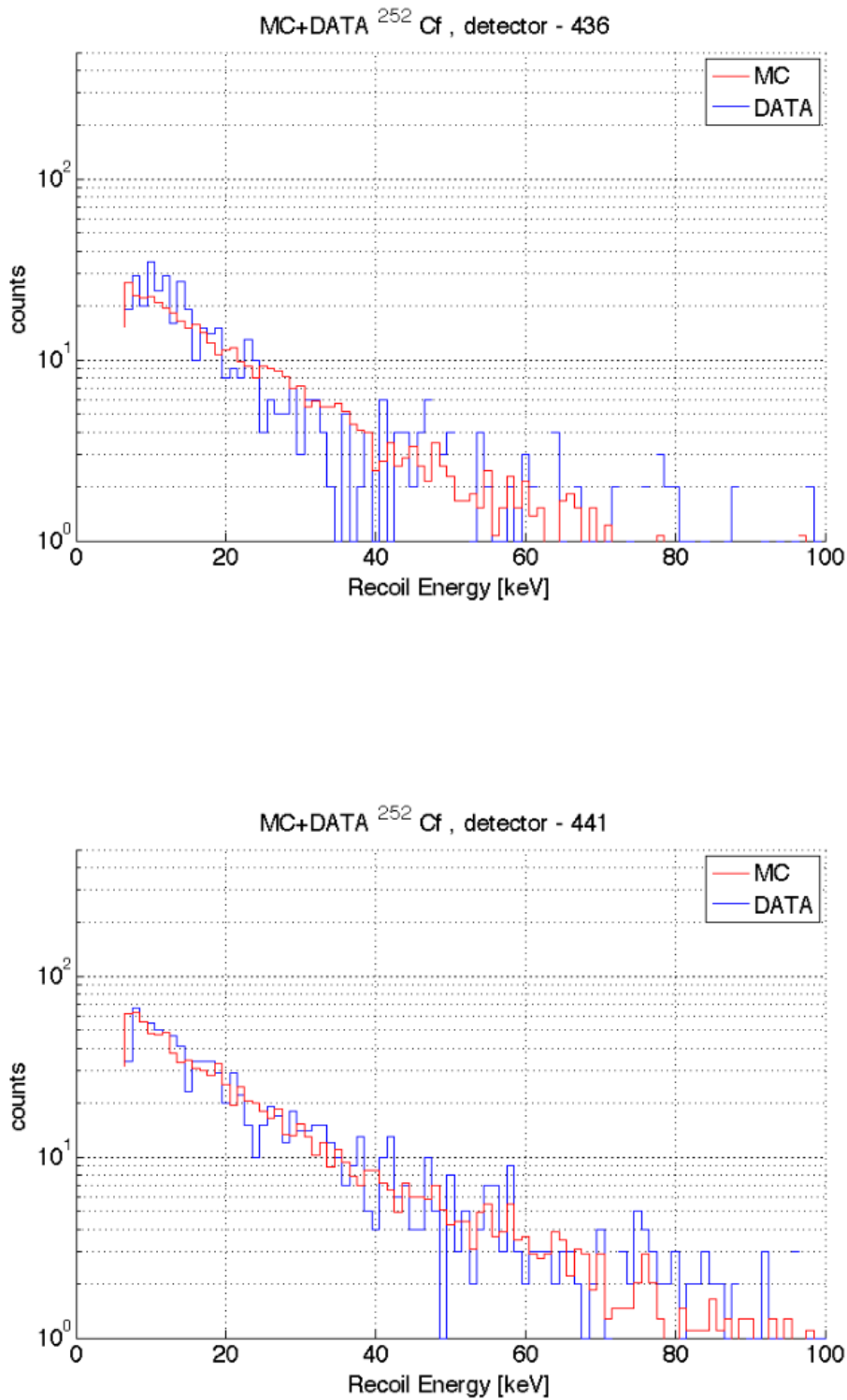


Figure A.10: ^{252}Cf -MC/Data - nuclear recoil spectras in detektors 436 and 441

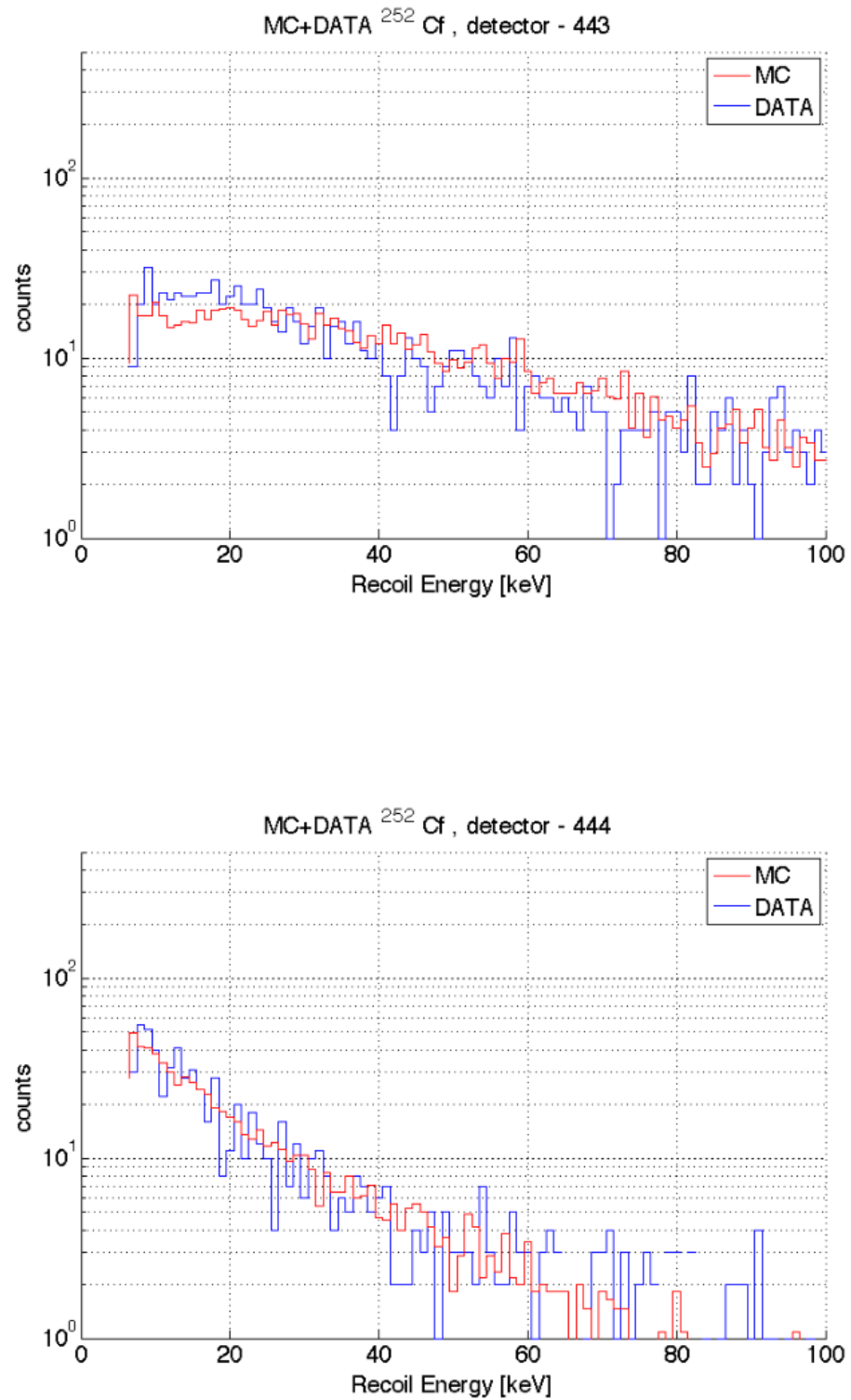


Figure A.11: ^{252}Cf -MC/Data - nuclear recoil spectra in detektors 443 and 444

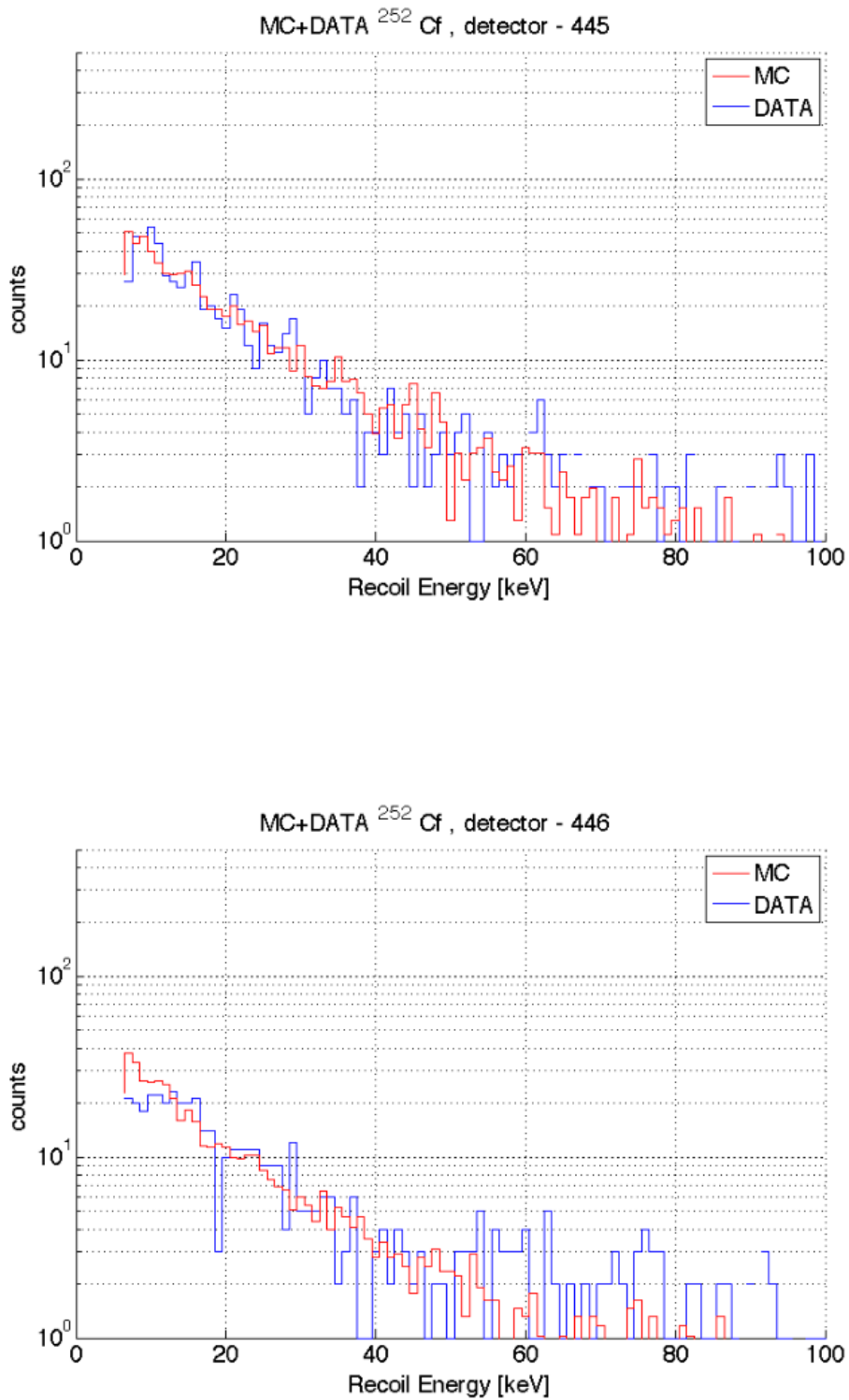


Figure A.12: ^{252}Cf -MC/Data - nuclear recoil spectras in detektors 445 and 446

Appendix B

(α, n) -neutron spectras.

The following graphics show the (α, n) neutron spectras as calculated by SOURCES4mv for U, Th and U+Th contaminations.

At the end Table B.1 shows the natural isotopic abundancies of the elements present in the Green Stone rock.

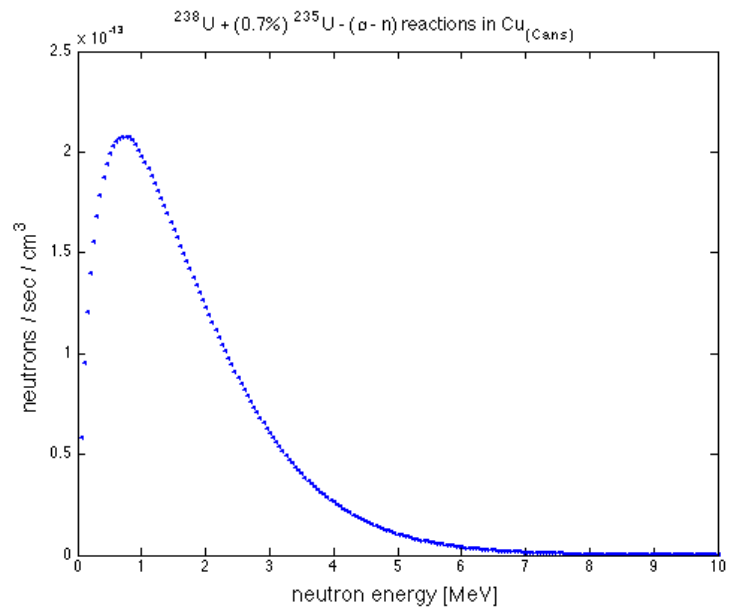


Figure B.1: U- (α, n) -spectra in the Cu-cans.
Total neutron rate: $9.82 \cdot 10^{-12} n/s/cm^3$.

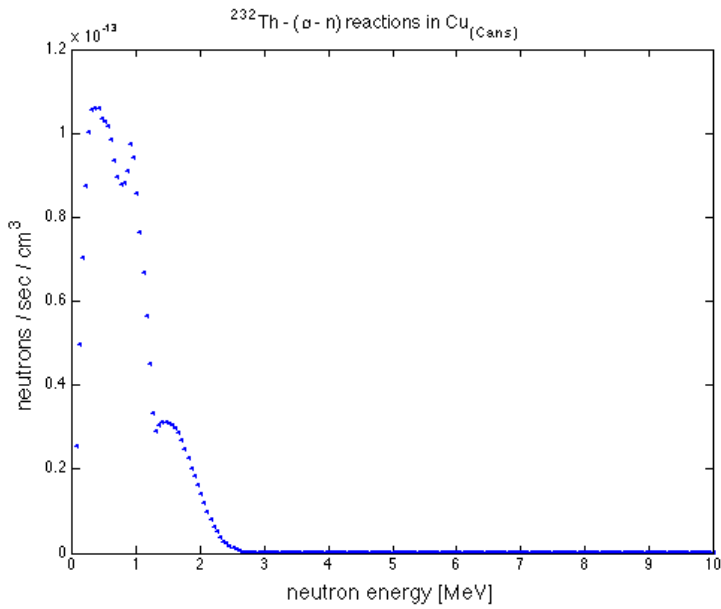


Figure B.2: Th- (α, n) -spectra in the Cu-cans.
Total neutron rate: $2.5 \cdot 10^{-12} n/s/cm^3$.

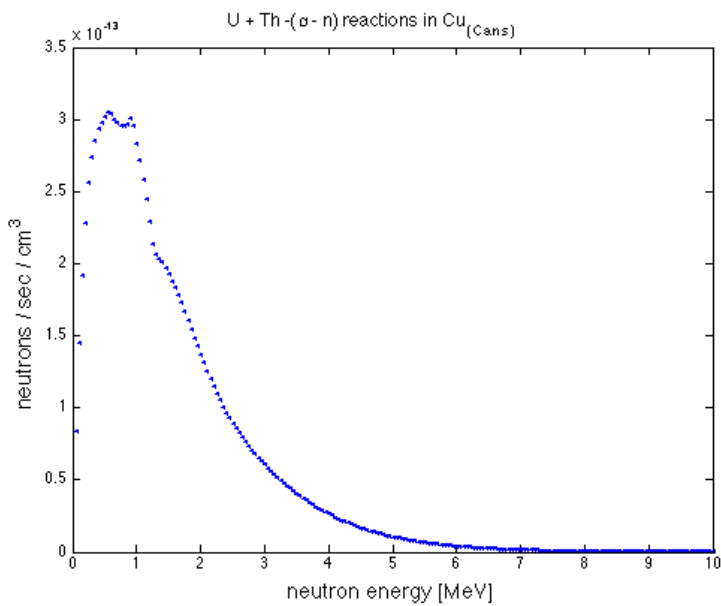


Figure B.3: U+Th- (α, n) -spectra in the Cu-cans.
Total neutron rate: $1.23 \cdot 10^{-12} n/s/cm^3$.

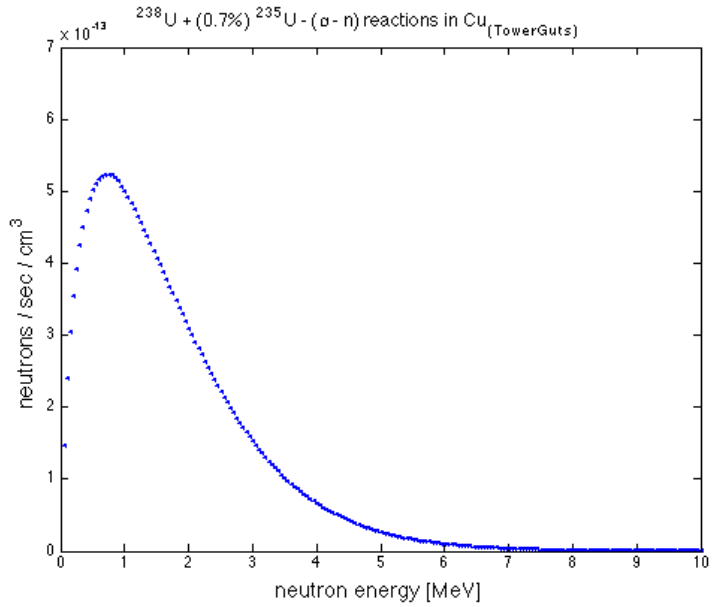


Figure B.4: U- (α, n) -spectra in the Cu-towerguts.
Total neutron rate: $2.47 \cdot 10^{-11} n/s/cm^3$.

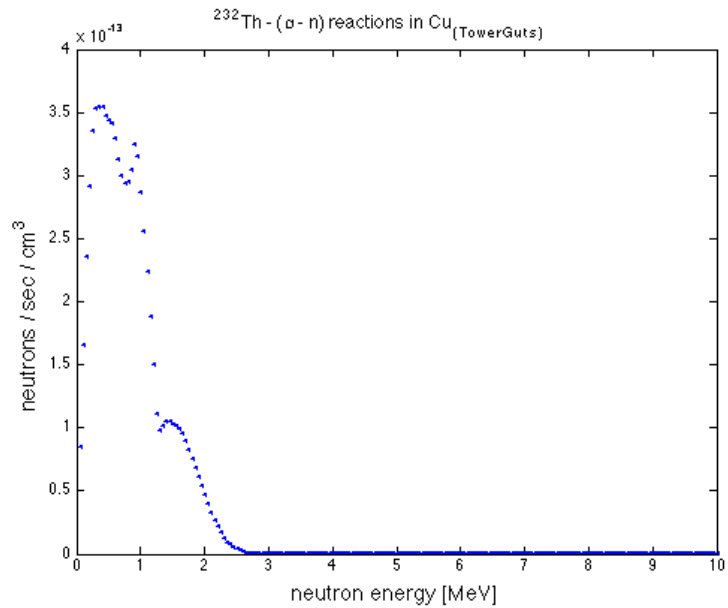


Figure B.5: Th- (α, n) -spectra in the Cu-towerguts.
Total neutron rate: $8.37 \cdot 10^{-12} n/s/cm^3$.

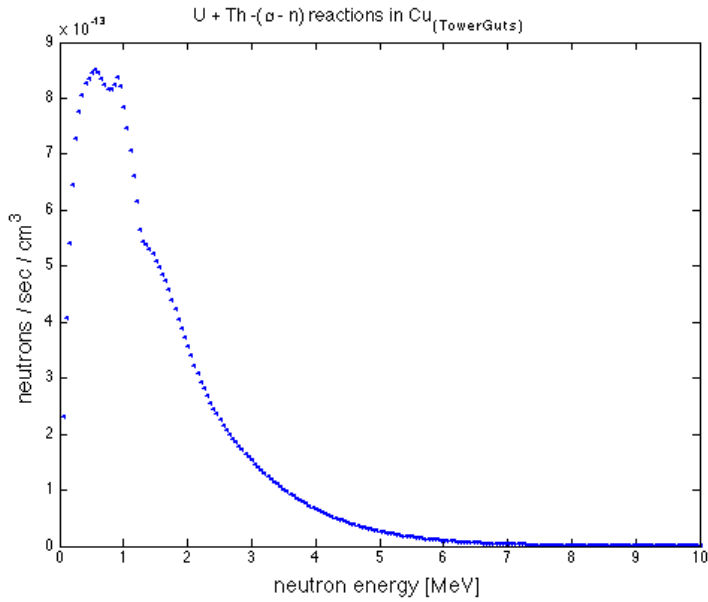


Figure B.6: U+Th- (α, n) -spectra in the Cu-towerguts.
Total neutron rate: $3.31 \cdot 10^{-11} n/s/cm^3$.

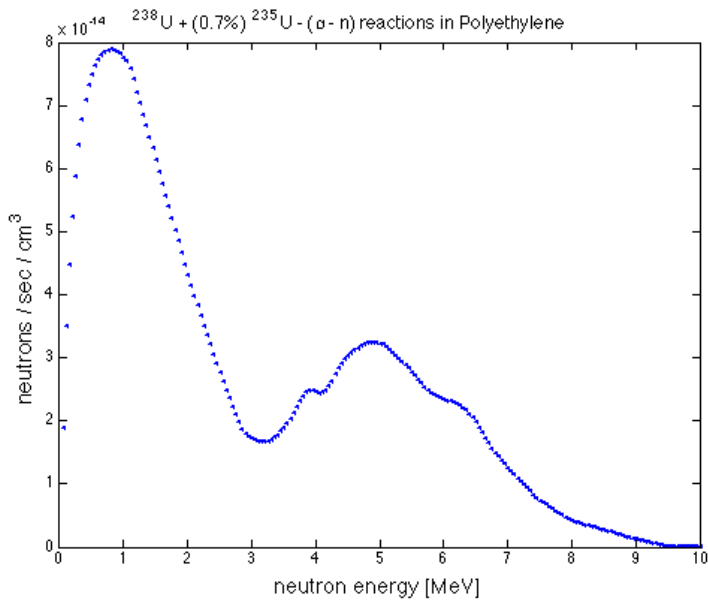


Figure B.7: U- (α, n) -spectra in the inner polyethylene shield.
Total neutron rate: $5.22 \cdot 10^{-12} n/s/cm^3$.

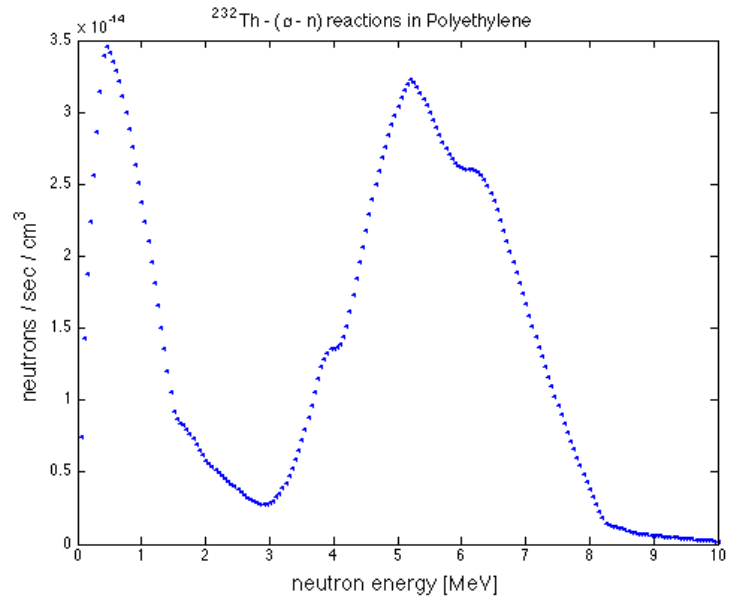


Figure B.8: Th- (α, n) -spectra in the inner polyethylene shield.
Total neutron rate: $2.71 \cdot 10^{-12} \text{n/s/cm}^3$.

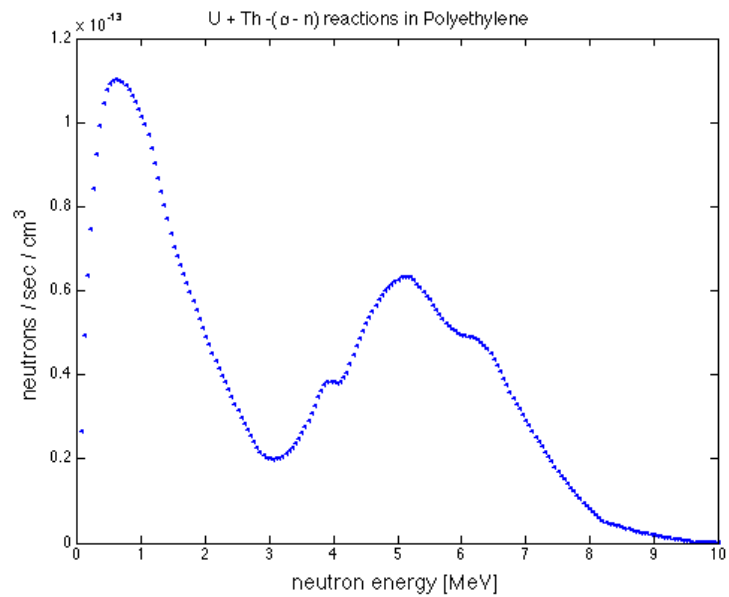


Figure B.9: U+Th- (α, n) -spectra in the inner polyethylene shield.
Total neutron rate: $7.94 \cdot 10^{-12} \text{n/s/cm}^3$.

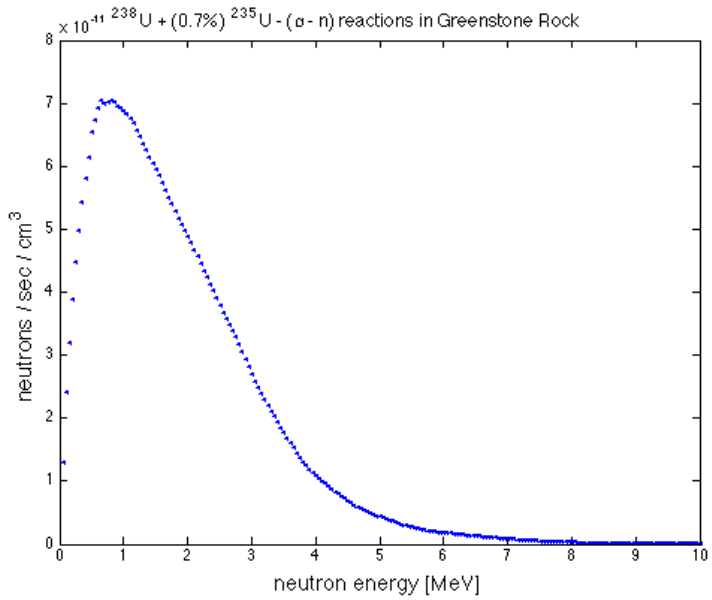


Figure B.10: U- (α, n) -spectra in the Green Stone rock.
Total neutron rate: $3.65 \cdot 10^{-9} n/s/cm^3$.

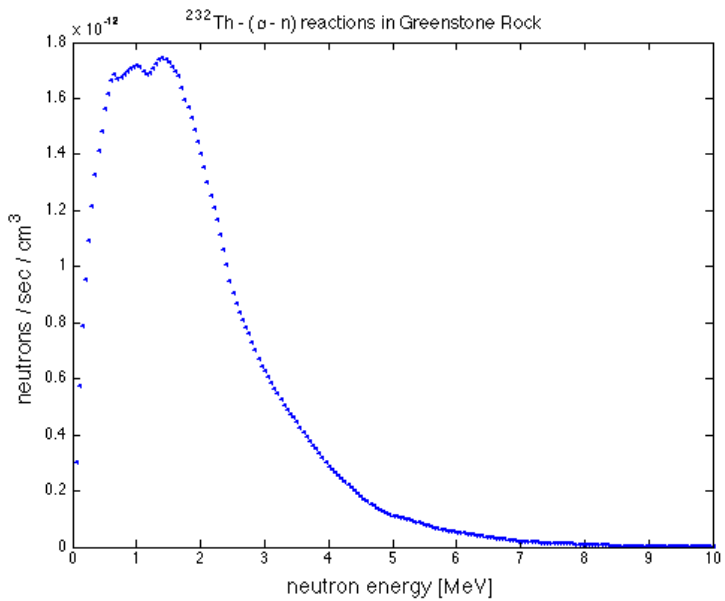


Figure B.11: Th- (α, n) -spectra in the Green Stone rock.
Total neutron rate: $9.42 \cdot 10^{-11} n/s/cm^3$.

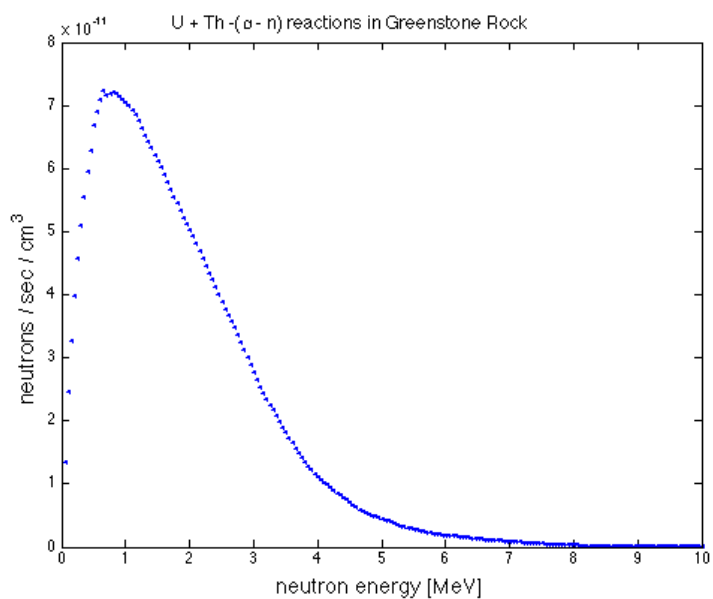


Figure B.12: U+Th- (α, n) -spectra in the Green Stone rock.
Total neutron rate: $3.74 \cdot 10^{-9} n/s/cm^3$.

Isotope	^{16}O	^{17}O	^{18}O			
Abundance [%]	99.762	0.038	0.2			
Isotope	^{28}Si	^{29}Si	^{30}Si			
Abundance [%]	92.23	4.68	3.087			
Isotope	^{46}Ti	^{47}Ti	^{48}Ti	^{49}Ti	^{50}Ti	
Abundance [%]	8.2	7.4	73.8	5.4	5.2	
Isotope	^{27}Al					
Abundance [%]	100					
Isotope	^{54}Fe	^{56}Fe	^{57}Fe	^{58}Fe		
Abundance [%]	5.8	91.7	2.12	0.3		
Isotope	^{55}Mn					
Abundance [%]	100					
Isotope	^{24}Mg	^{25}Mg	^{26}Mg			
Abundance [%]	78.99	10	11.01			
Isotope	^{40}Ca	^{42}Ca	^{43}Ca	^{44}Ca	^{46}Ca	^{48}Ca
Abundance [%]	96.941	0.647	0.135	2.086	0.004	0.187
Isotope	^{23}Na					
Abundance [%]	100					
Isotope	^{39}K	^{40}K	^{41}K			
Abundance [%]	93.258	0.0117	6.7302			
Isotope	^{12}C	^{13}C				
Abundance [%]	98.9	1.1				
Isotope	^{31}P					
Abundance [%]	100					

Table B.1: Natural abundance of the isotopes in the Green Stone rock.

Appendix C

Spontaneous Fission-neutron spectras.

The following graphics show the neutron spectras caused by spontaneous fission (SF) for U, Th and U+Th contaminations as calculated by SOURCES4mv.

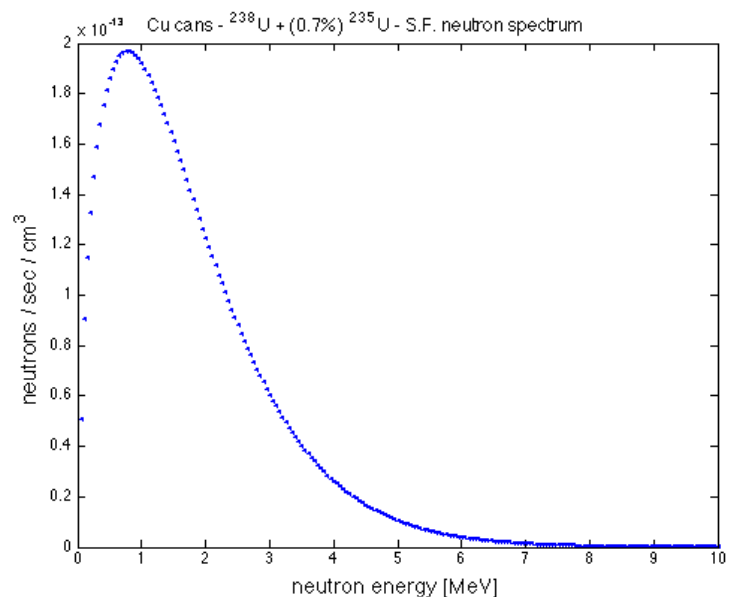


Figure C.1: U-(SF)-spectra in the Cu-cans.
Total neutron rate: $9.6 \cdot 10^{-12} n/s/cm^3$.

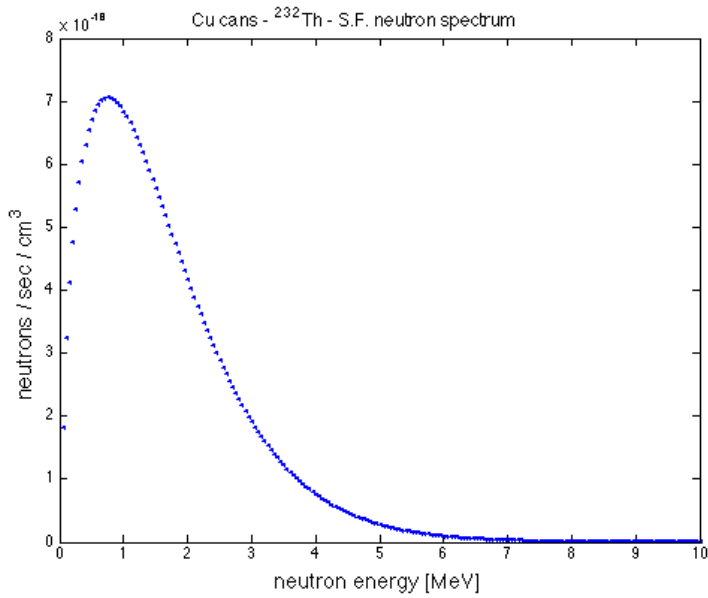


Figure C.2: Th-(SF)-spectra in the Cu-cans.
Total neutron rate: $3.27 \cdot 10^{-16} n/\text{s}/\text{cm}^3$.

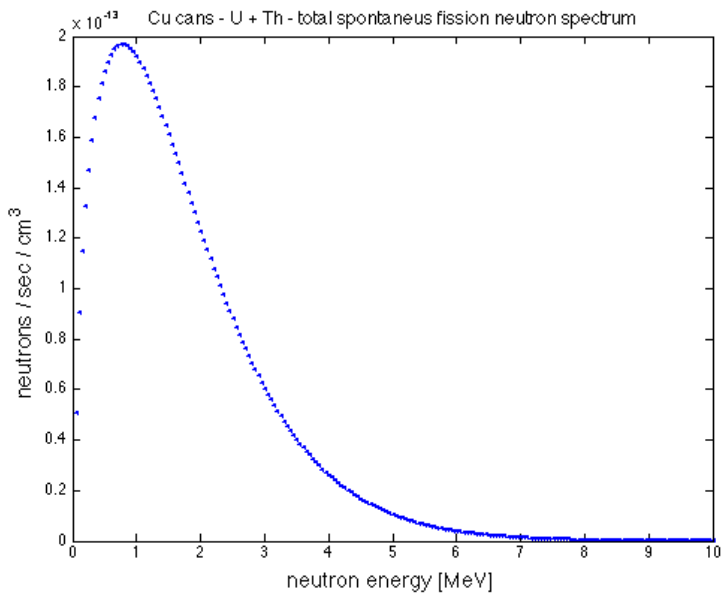


Figure C.3: U+Th-(SF)-spectra in the Cu-cans.
Total neutron rate: $9.6 \cdot 10^{-12} n/\text{s}/\text{cm}^3$.

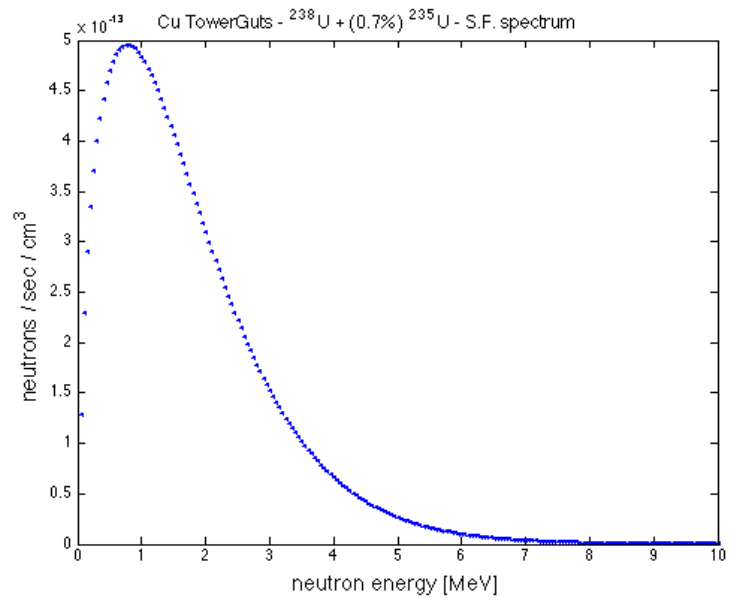


Figure C.4: U-(SF)-spectra in the Cu-towerguts.
Total neutron rate: $2.42 \cdot 10^{-11} n/s/cm^3$.

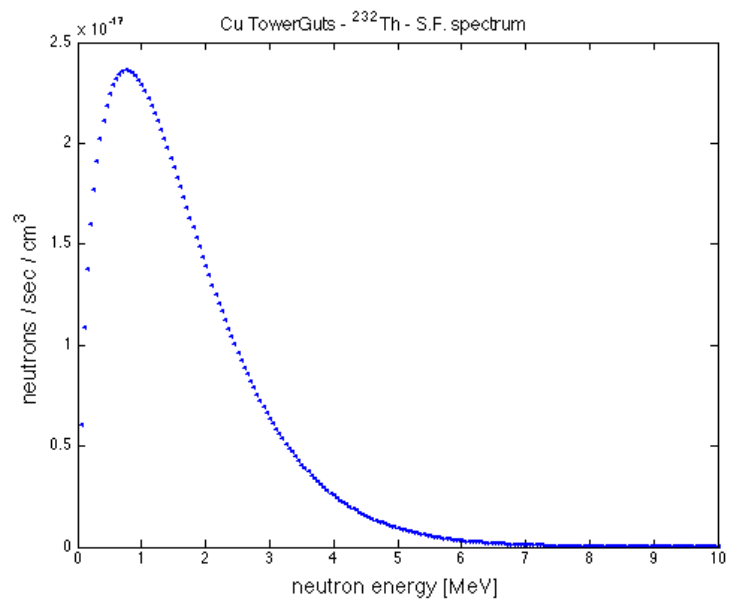


Figure C.5: Th-(SF)-spectra in the Cu-towerguts.
Total neutron rate: $1.09 \cdot 10^{-15} n/s/cm^3$.

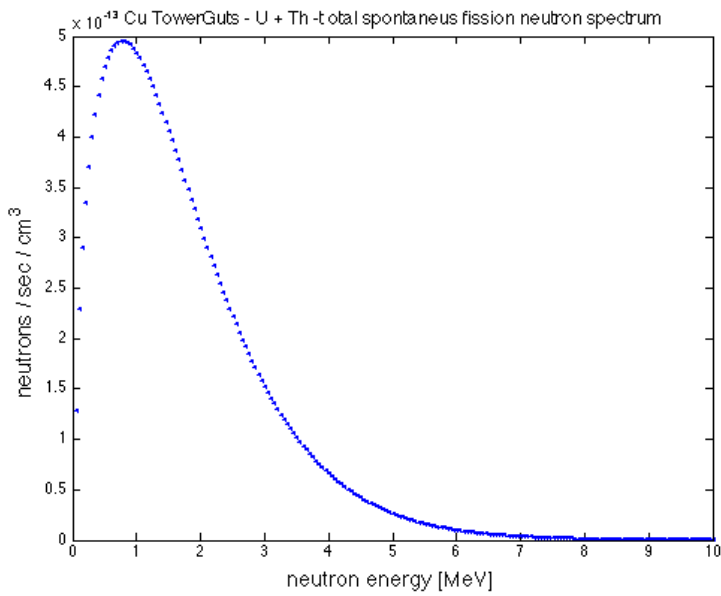


Figure C.6: U+Th-(SF)-spectra in the Cu-towerguts.
Total neutron rate: $2.42 \cdot 10^{-11} n/s/cm^3$.

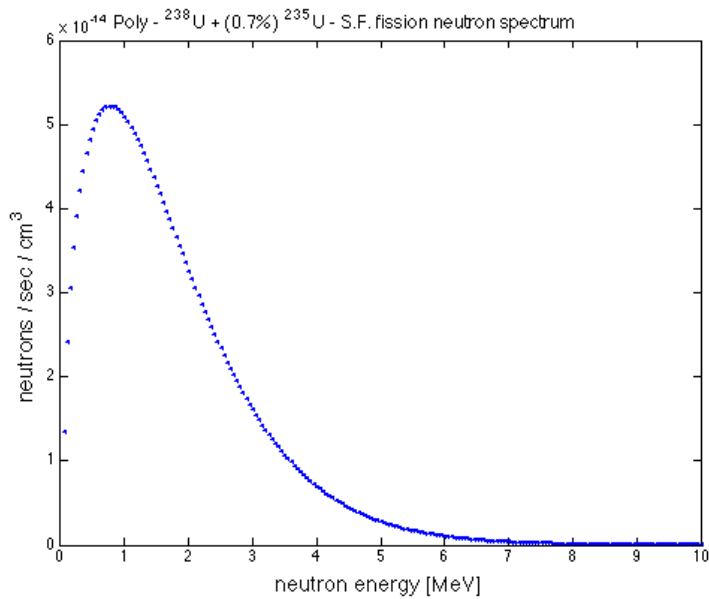


Figure C.7: U-(SF)-spectra in the inner polyethylene shield.
Total neutron rate: $2.55 \cdot 10^{-12} n/s/cm^3$.

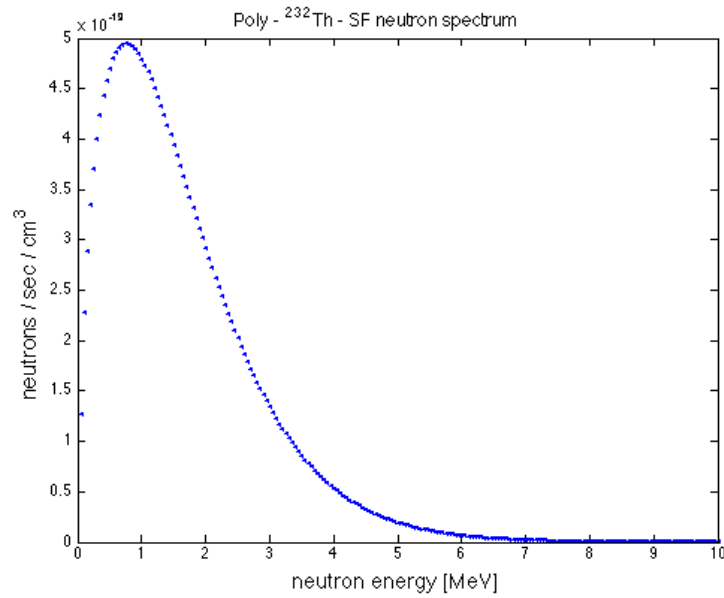


Figure C.8: Th-(SF)-spectra in the inner polyethylene shield.
Total neutron rate: $2.29 \cdot 10^{-17} n/s/cm^3$.

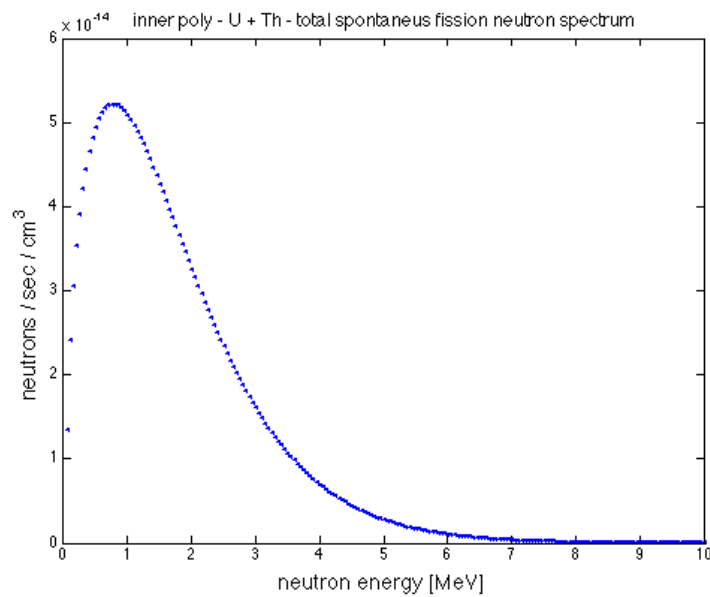


Figure C.9: U+Th-(SF)-spectra in the inner polyethylene shield.
Total neutron rate: $2.55 \cdot 10^{-12} n/s/cm^3$.

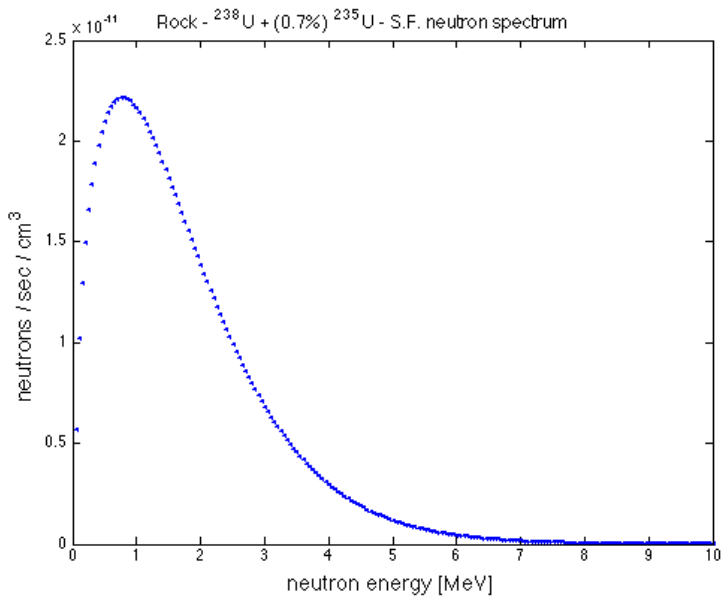


Figure C.10: U-(SF)-spectra in the Green Stone rock.
Total neutron rate: $1.08 \cdot 10^{-9} \text{n/s/cm}^3$.

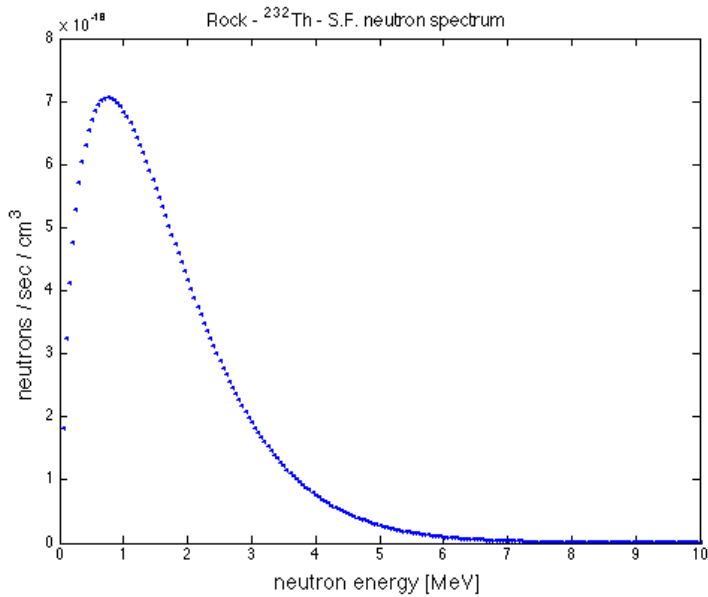


Figure C.11: Th-(SF)-spectra in the Green Stone rock.
Total neutron rate: $3.27 \cdot 10^{-16} \text{n/s/cm}^3$.

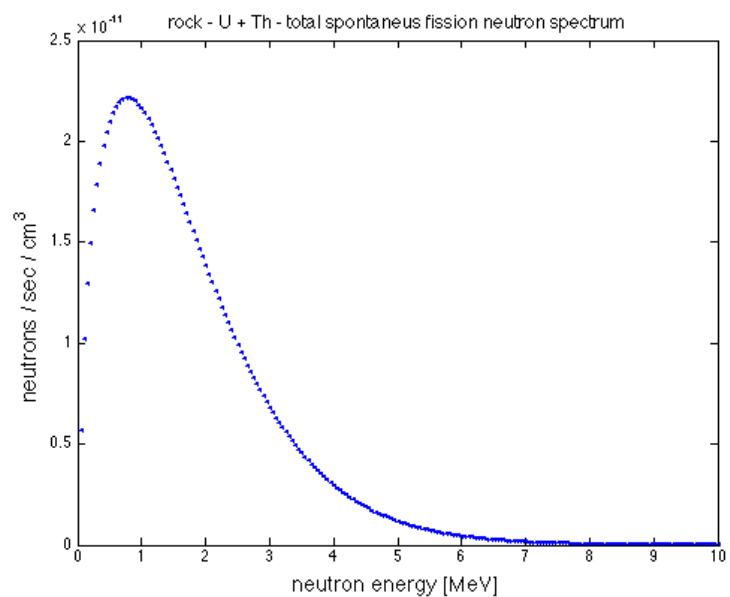


Figure C.12: U+Th-(SF)-spectra in the Green Stone rock.
Total neutron rate: $1.08 \cdot 10^{-9} n/s/cm^3$.

Bibliography

- [1] **First results from the 2dF galaxy redshift survey.** Matthew Colless . MSSSO-MMC-980407, Apr 1998. 12pp., arXiv:astro-ph/9804079v1.
- [2] **The Review of Particle Physics**, <http://pdg.lbl.gov/>.
- [3] **Constraints on the Self-Gravity of Radiation Pressure via Big Bang Nucleosynthesis.** Saul Rappaport, Josiah Schwab, Scott Burles . Jul 2007. 4pp., arXiv:0707.3589v1 [astro-ph].
- [4] **H I rotation curves of spiral galaxies. I - NGC 3198.** K.G. Begeman (Groningen U.) . Oct 1989. Published in Astron.Astrophys.223:47-60,1989.
- [5] **Structure, mass and distance of the virgo cluster from a tolman-bondi model.** Pascal Fouque, Jose M. Solanes, Teresa Sanchis, Chantal Balkowski. Jun 2001. 12pp., arXiv:astro-ph/0106261v1.
- [6] **Candidates for intracluster planetary nebulae in the Virgo cluster based on the Suprime-Cam narrow-band imaging in O[III] and H-alpha.** S. Okamura et al. Nov 2002. 8pp. Submitted to Publ.Astron.Soc.Jap., arXiv:astro-ph/0211352v1.
- [7] **Diffuse x-ray emission from the NGC-2300 group of galaxies: Implications for dark matter and galaxy evolution in small groups.** John S. Mulchaey (Baltimore, Space Telescope Sci. and Maryland U.) , David S. Davis, Richard F. Mushotzky (NASA, Goddard) , David Burstein (Arizona State U.) . LHEA-93-15, Sep 1992. 16pp. Submitted to Astrophys. J. Lett..
- [8] **Three-year Wilkinson Microwave Anisotropy Probe (WMAP) observations: temperature analysis.** By WMAP Collaboration (G. Hinshaw et al.). Mar 2006. 93pp. Published in Astrophys.J.Suppl.170:288,2007, arXiv:astro-ph/0603451v2.
- [9] **Max Planck Institute for Astrophysics**, Garching, <http://www.mpa-garching.mpg.de/Virgo/virgopics.html>.
- [10] **Constraints on planetary companions in the magnification $A = 256$ microlensing event: OGLE-2003-BLG-423.** By The MuFUN Collabora-

- tion, The OGLE Collaboration (Jaiyul Yoo et al.). Mar 2004. 10pp. Published in *Astrophys.J.*616:1204-1214, 2004, arXiv:astro-ph/0403459v2.
- [11] **A direct empirical proof of the existence of dark matter.** Douglas Clowe (Arizona U., Astron. Dept. - Steward Observ.) , Marusa Bradac (KIPAC, Menlo Park) , Anthony H. Gonzalez (Florida U.) , Maxim Markevitch (Harvard-Smithsonian Ctr. Astrophys. and Moscow, Space Res. Inst.) , Scott W. Randall, Christine Jones (Harvard-Smithsonian Ctr. Astrophys.) , Dennis Zaritsky (Arizona U., Astron. Dept. - Steward Observ.) . SLAC-PUB-12078, Aug 2006. Submitted to *Astrophys.J.Lett.*, arXiv:astro-ph/0608407v1.
 - [12] **The Cosmic baryon budget.** M. Fukugita (Princeton, Inst. Advanced Study and Tokyo U., ICRR) , C.J. Hogan (Washington U., Seattle) , P.J.E. Peebles (Princeton U.) . IASSNS-AST-97-72, Dec 1997. 27pp. Published in *Astrophys.J.*503:518,1998, arXiv:astro-ph/9712020v2.
 - [13] **Review of Big Bang nucleosynthesis and primordial abundances.** David Tytler, John M. O'Meara, Nao Suzuki, Dan Lubin (San Diego, CASS) . Jan 2000. 61pp. Published in *Phys.Scripta* T85:12,2000., arXiv:astro-ph/0001318v1.
 - [14] **Constraints on neutrino masses from a galactic supernova neutrino signal at present and future detectors.** Enrico Nardi (Frascati and Antioquia U.) , Jorge I. Zuluaga (Antioquia U.) . Dec 2004. 22pp. Published in *Nucl.Phys.B*731:140-163,2005, arXiv:hep-ph/0412104v2.
 - [15] **Cosmological limits on the neutrino mass from the Ly alpha forest.** Rupert A.C. Croft (Harvard U.) , Wayne Hu (Princeton, Inst. Advanced Study) , Romeel Dave (Princeton U. Observ.) . Mar 1999. 4pp. Published in *Phys.Rev.Lett.*83:1092-1095,1999, arXiv:astro-ph/9903335v1.
 - [16] **WIMP / neutralino direct detection.** Maryvonne De Jesus (Lyon, IPN) . LYCEN-2003-69, Feb 2004. 9pp. Review talk at 21st International Symposium on Lepton and Photon Interactions at High Energies (LP 03), Batavia, Illinois, 11-16 Aug 2003. Published in *Int.J.Mod.Phys.A*19:1142,2004, arXiv:astro-ph/0402033v1.
 - [17] **Galactic halo models and particle dark matter detection.** Marc Kamionkowski, Ali Kinkhabwala (Columbia U.) . CU-TP-864, CAL-648, Oct 1997. 9pp. Published in *Phys.Rev.D*57:3256-3263,1998, arXiv:hep-ph/9710337v1.
 - [18] V. Mandic, **First Results from the Cryogenic Dark Matter Search Experiment at the Deep Site**, Ph.D. Thesis, Department of Physics, University of California, Berkeley (2004).

- [19] **Results from DAMA / NaI and perspectives for DAMA / LIBRA.** R. Bernabei et al. Nov 2003. Contributed paper to 4th International Conference on Physics Beyond the Standard Model: Beyond the Desert (BEYOND 03), Castle Ringberg, Tegernsee, Germany, 9-14 Jun 2003. Published in *Tegernsee 2003, Beyond the desert* 541-560, arXiv:astro-ph/0311046v1.
- [20] A.J. Da Silva, **Development of a Low Background Environment for the Cryogenic Dark Matter Search**, Ph.D. Thesis, Department of Physics, University British Columbia (1996).
- [21] **Exclusion limits on the WIMP nucleon cross-section from the cryogenic dark matter search.** By CDMS Collaboration (D. Abrams et al.). FERMILAB-PUB-02-287, CWRU-P4-02, UCSB-HEP-02-02, Mar 2002. 38pp. Published in Phys.Rev.D66:122003,2002, arXiv:astro-ph/0203500v3.
- [22] T. Saab, **Search for Weakly Interacting Massive Particles with the Cryogenic Dark Matter Search Experiment**, Ph.D. Thesis, Stanford University (2002).
- [23] S. Kamat, **Extending the Sensitivity to the Detection of WIMP Dark Matter with an Improved Understanding of the Limiting Neutron Backgrounds**, Ph.D. Thesis, Department of Physics, Case Western Reserve University (2005).
- [24] **Exclusion Limits on the WIMP-Nucleon Cross-Section from the First Run of the Cryogenic Dark Matter Search in the Soudan Underground Lab.** By CDMS Collaboration (D.S. Akerib et al.), Jul 2005. Published in Phys.Rev. D72 (2005) 052009, arXiv:astro-ph/0507190 v1.
- [25] **Limit Plotter.**
<http://dmtools.berkeley.edu/limitplots/>.
- [26] C.L. Chang, **The Cryogenic Dark Matter Search (CDMS-II) Experiment - First Results from the Soudan Mine**, Ph.D. Thesis, Stanford University (2004).
- [27] LA-13639-MS, **SOURCES4A manual**.
- [28] Landolt-Bornstein, **Low Energy Neutron Physics**, Springer Verlag.
- [29] **Cross Section Plotter.** <http://atom.kaeri.re.kr/cgi-bin/endfplot.pl>.
- [30] **Contamination links.**
</neutrons/alpha-n-bauer.pdf>.
</ebook/040615/index.html>.
</Materials/ActivitySheets/>.
- [31] **WebElements.**
<http://www.webelements.com/webelements/elements/>.

- [32] **Low-Radioactivity Background Techniques**, G. Heusser. Annual Review of Nuclear and Particle Science. Vol. 45: 543-590 (Volume publication date December 1995).
- [33] **Underground particle fluxes in the Soudan mine.** Keith Ruddick, NuMI-L-210, Sept 1996.
- [34] **A Unified approach to the classical statistical analysis of small signals.** Gary J. Feldman (Harvard U.) , Robert D. Cousins (UCLA) . HUTP-97-A096, Nov 1997. 20pp. Published in Phys.Rev.D57:3873-3889,1998, arXiv:physics/9711021v2 [physics.data-an].
- [35] Glenn F. Knoll, **Radiation Detection and Measurement**, Wiley, 2000.
- [36] H. Cember, **Introduction to Health Physics**, McGraw-Hill, 1996.
- [37] N. Ensslin, **The Origin of Neutron Radiation**, Passive Non-Destructive Assay Manual, Los Alamos National Laboratory, 1991, ISBN 0-16-032724-5.
- [38] **National Institute of Standards and Technology.**
<http://physics.nist.gov/PhysRefData/Star/Text/ASTAR.html>.

Appendix D

Acknowledgment

In erster Linie moechte ich mich bei Prof. Laura Baudis bedanken, die mir diese Arbeit auf einem sehr interessanten Forschungsgebiet ermoeglicht hat. Desweit-eren bedanke ich mich bei meinen Kollegen aus Uebersee, die mir sehr viel bei den Simulationen geholfen und erklaert haben. Besonderer Dank dabei an Angela Reisetter und Xinjie Qiu von der Universitaet Minnesota. Ebenfalls ein herzliches Dank an meine Buero-Kollegen aus der CDMS und Xenon Kollaboration, v.a. an Tobias Bruch, Sebastian Arrenberg, Stephan Schulte und Martin Bissok, die ausser den vielen Anregungen auch fuer eine witzige und entspannte Stimmung sorgten, die das arbeiten wesentlich leichter gemacht hat. Ein letztes Dank an Salvatore Manmana von der EPF Lausanne fuer seine Kommentare und Korrek-turvorschlaege bezueglich dieser Arbeit, und auch an Gerhard Backes, meinem Chef am ILT Aachen, der sich waehrend meiner Diplomarbeit als sehr geduldig und Hilsbereit erwiesen hat.

Erklaerung

Hiermit versichere ich, dass ich diese Arbeit selbststaendig und ohne Benutzung anderer als der angegeben Quellen und Hilfsmittel angefertigt habe.

Aachen, 16. Oktober 2007